UNIVERSITA' DEGLI STUDI DI NAPOLI

"FEDERICO II"

FACOLTA' DI INGEGNERIA

DOTTORATO DI RICERCA IN INGEGNERIA AEROSPAZIALE, NAVALE E DELLA QUALITA'
XIX CICLO

Numerical and experimental study of UHTC materials for atmospheric re-entry

Coordinatore:

Ch.mo Prof. A. Moccia

Candidato:

Ing. Arturo Francese

Tutor:

Ch.mo Prof. R. Monti

Ch.mo Prof. R. Savino

This page intentionally left blank

To my mother Rosa Longobardi,

To my love Raffaella

Acknowledgements

At the end of my course of study, there are some people I would like to thank for a huge variety of reasons.

Firstly, I would like to thank my tutors prof. Raffaele Savino and prof. Rodolfo Monti.

I could never imagine to have better advisor and mentor for my PhD, and without their common-sense, knowledge, patience (above all) I would never have finished.

I am grateful to the secretaries Brigida Stanziano and Mirella Parilli for helping the Dept. of Space Science and Engineering "L.G. Napolitano" to run smoothly and for assisting me in many different ways. I would like to thank also Pasquale Loquace for technical assistance and all department's personnel for the willingness.

There are no words for my friends Diego Paterna and Mario De Stefano Fumo. With their enthusiasm, their inspiration, and their great efforts to explain things clearly and simply, they helped me to live in the best way, these three years at department during my course of study.

Special thanks go to my family, my father Nicola, my brother Francesco and my sister Anna, for the reciprocal support in the difficult.

Finally, a lover-tender thanks to Raffaella for helping me to go over the difficult times and for all the wonderful support throughout my thesis-writing period. I would have been lost without her.

To my mother Rosa Longobardi, I only wish to say "I miss you", especially in these moments.

Contents

Nomenclature

c_i = mass fraction of i-th specie
c_p = specific heat, J/kg-K
D_i = diffusion coefficient of i-th specie, m^2/s
Da = Damkoeler number
L = aerodynamic lift, N
h_{ch} = specific chemical enthalpy, J/kg
h_w = specific wall enthalpy, J/kg
H = specific total enthalpy, J/kg
M = Mach number
p = pressure, Pa
P_0 = total pressure, Pa
p_{02} = stagnation point pressure, Pa
$\dot{q}_0$ = stagnation point heat flux, W/m^2
r = curvature radius, m
Re_1 = Reynolds number per unit length, m^{-1}
T = temperature, K
V = velocity, m/s
Z = Altitude, km
$(\Delta h_f)_i^0$ = formation enthalpy of i-th specie, J/kg

Greek symbols

ε = emissivity
γ = recombination coefficient
λ = thermal conductivity, W/m-K
ρ = density, kg/m^3
σ = Stephan-Boltzmann constant, $W/m^2\text{-}K^4$

Subscripts

t = wind tunnel conditions
∞ = freestream conditions

Abbreviations and acronyms

UHTC	Ultra High Temperature Ceramic
SiC	Silicon Carbide
ZrB_2	Zirconium Diboride
PWT	Plasma Wind Tunnel
CIRA	Italian Aerospace Research Centre
NASA	National Aeronautical and Space Administartion

1 Introduction

An atmospheric re-entry with an increased re-entry time duration (order of hours compared with conventional re-entry of about 20 minutes for Shuttle) and a more gentle deceleration of the vehicle at higher altitudes along the trajectory imply lower values of the energy conversion per unit time, less severe aerodynamic heating rate, lower mechanical loads and decelerations.
This innovative re-entry concept makes use of a sharp edge fuselage and wings, flying at low angle of attack. In this manner, the convective heat fluxes are concentrated at the leading edges and the rest of the structure is thermally protected by the thermal boundary layer which remains sufficiently thick.
Large convective heat fluxes on the leading edges asks for innovative materials that can stand temperature larger than 2000 K. A class of materials that seems able to sustain such temperatures are the Ultra High Temperature Ceramic (UHTC).
The on-ground experimentation testing about UHTC materials is included in a technology project by European Space Agency (ESA), called European eXPErimental Re-entry Testbed (EXPERT).
In this program, a capsule will carry out several scientific payloads devoted to study the main aspects of the hypersonic flight.
In particular, the scientific payload Sharp Hot Structures (SHS) is aimed to test a UTHC material in real re-entry conditions and use the collected data to make a correlation among on-ground and in-flight experimental measurements and numerical results.
The SHS project activity is focused on the manufacturing of high performance and slender shaped structures for reusable launch vehicles.
Flight experiments are typically associated with high costs, while numerical simulations contain several shortcomings when modelling aero-thermo-dynamic processes. Therefore, long-duration, high-enthalpy, ground-test facilities are still the key tools for the design, verification and qualification of re-entry vehicles hot structures.

During the on-ground experimentation, to achieve flight-like conditions, we test UHTC (Ultra High Temperature Ceramic) specimens in arc-jet high enthalpy flows, using the SPES (Small Planetary Entry Simulator) facility available at the Department of Space Science and Engineering “L.G. Napolitano”, University of Napoli “Federico II”, Napoli, Italy.
The objectives of these tests are:

- To demonstrate the capability of the material to withstand, for a sufficient time, at temperature of the order of 2000 °C in oxidizing atmosphere;
- To characterize the materials’ surface in terms of spectral emissivity and surface catalicity.

The use of ground-based, high-enthalpy facilities such as SPES, requires a detailed knowledge of the test section flow. Because the flow conditions generated in high-enthalpy tunnels are very complex, the characterization of the free-stream flow must be a combined effort of measurement techniques and computational fluid dynamics (CFD) simulations.
For high-enthalpy testing, this close cooperation between experimental testing and CFD simulations can be regarded as an iteractive process, providing a step-by-step improved understanding of the facility performance.

The activity was initially focused on a preliminary theoretical and numerical analysis of the geometry and configuration of the UHTC specimens and holder to be tested under high specific enthalpy flow.

In particular, numerical simulations have been carried out to investigate the following aspects:

- The magnitude and distribution of the surface convective heat flux.
- The aerodynamic heating, caused by the surface heat flux, at the typical conditions of the plasma torch SPES facility.
- The effects of the surface emissivity and catalytic properties of the materials.

The main requirement is the possibility to test UHTC materials at temperatures in the order of 1800°C-2000°C in high enthalpy flows (order of 10-20 MJ/Kg).

The CFD computations have been carried out by solving the full Navier-Stokes equations for a multi-reacting gas mixture in chemical non equilibrium, in order to evaluate the convective surface heat flux and the pressure distribution on the specimen, at the typical conditions of the SPES facility.
The numerical model has been previously validated by comparing numerical results and experimental data available in literature (Ref. 1-5). The possibility of evaluating the surface catalytic property by numerical-experimental correlation of the surface heat flux on specimens at typical plasma torch conditions was already been demonstrated (Ref. 2).
The present thesis is devoted to the in-flight and on-ground characterization of UHTC materials in term of surface catalicity, spectral emissivity and resistance to oxidation. It is divided in four parts:

- Part I deals with an introduction to the thermal protection systems (TPS) and in particular with a new concept of TPS for next generation re-entry vehicles based on the Ultra High Temperature Materials (UHTCs).
- Part II deals with the design of a flying test-bed in the frame of the EXPERT (European eXPErimental Re-entry Testbed) program. The test-bed objectives are: the design, fabrication and testing in real re-entry environment conditions, of a prototype of UHTC specimen for an advanced concept of hot structure.
- Part III deals with the on-ground experimentation on UHTC materials in high enthalpy flow by Small Planetary Entry Simulator (SPES) facility. In this part, there is also a description of the SPES facility, the instrumentations and the experimental tests setup.
- Part IV deals with the results of the experimental-numerical correlations for the characterization of UHTC materials in terms of spectral emissivity and surface catalicity.

2 Thermal Protection Systems for re-entry vehicles

A space vehicle that enters a planetary atmosphere (e.g. earth) requires the use of a thermal protection from aerodynamic heating. The aerodynamic heating is generated at the surface of an object entering the atmosphere due to the combination of compression and surface friction of the atmospheric gas.
The vehicle's configuration and entry trajectory, in combination with the type of used surface material, define the temperature distribution on the surface vehicle. The Space Shuttle Orbiter features a thermal protection system based on the use of surface materials with a high heat capacity in combination with an underlying thermal insulation to inhibit the conduction of heat to the interior of the vehicle. The heat developed from the aerodynamic heating process is thereby radiated back into space by virtue of the high surface emissivity. The leading edges of wings and the nose cap are the highest temperature regions. Due to the wide variation of these temperatures, the TPS selected for Space Shuttle was composed of many different materials (see Figure 1(a)).

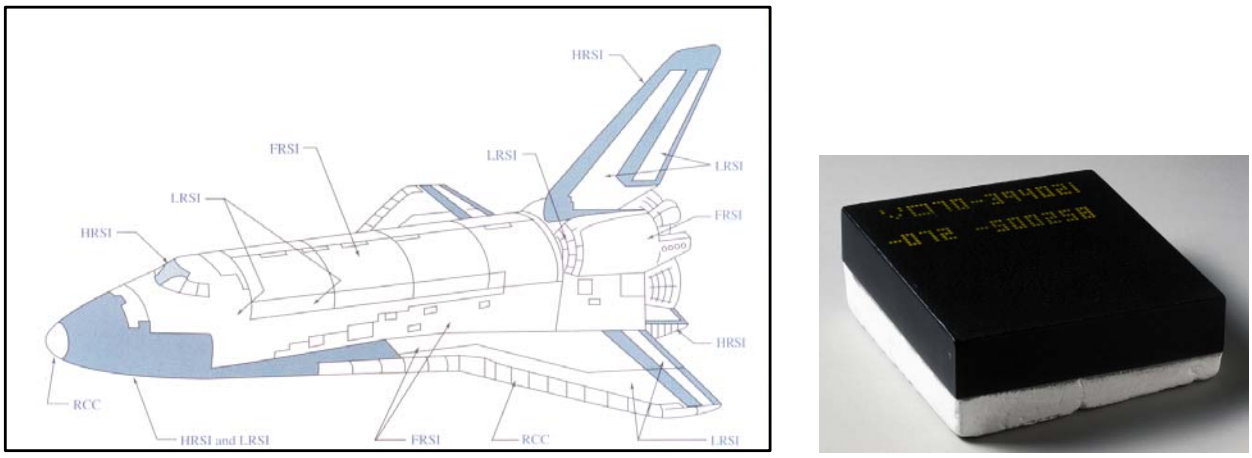

Figure 1 (a) Space Shuttle Orbiter TPS and (b) Tiles of TPS Shuttle

Each material's heat capacity, durability and weight determine the extent of its application on the vehicle. Improvements to these materials have been the subject of much research as enhanced capability material (i.e., more durability, higher temperature capability, greater thermal shock resistance and lower thermal conductivity) improves thermal protection material and vehicle performance.
Future re-entry vehicles capabilities will depend upon the capabilities of TPS being developed and available to them. The economic ups and downs of reusable rocketry largely depend on beat-the-heat protection systems. Without a robust, temperature-thwarting, and easily maintainable outer skin, rockets of the future may never offer routine, low-cost access to space.
Getting the vehicle ready for re-launch is a long and costly process. About 30,000 hours of work is needed between flights, and that's on the TPS alone. The TPS is reusable for 100 missions, but only after loads of hands-on, tender-loving care (see figure 1-b, a tile's TPS Orbiter).
In the atmospheric re-entry missions, in particular, the TPS must be able to avoid heat goes deep into the vehicle, so as to keep structure safe from the high heat fluxes raised by the aerodynamic heating, so that material properties don't decay because of strains. These protections work depending on the thermal load. There are three types of strategies to protect the space vehicle during the re-entry: active, semi-passive and passive systems.

2.1 Conventional Thermal Protection Systems

Passive systems

The passive systems are the heat transfer systems without power spending nor moving pieces. Hence, among heat transfer modes, we can have the radiative transfer only, and the surface optical properties are the unique parameters to play with.
These type of systems don't match with Reusable Launch Vehicle (RLV), because they would require too high masses to absorb the re-entry high energies.
Moreover these systems work well beyond radiative equilibrium temperature so that they can't achieve an efficient radiative cooling.
Another type of passive system is based on the concept of *Hot Structure,* i.e. on the use of structural materials able to hang in high temperature (see Figure 2). Not even one material now used in the aerospace applications is able to tolerate the very high temperatures achieved during the re-entry of sharp vehicles. Actually, the availability of ceramic materials with very high thermal resistance has changed this scenario, so that we can think to new configurations.

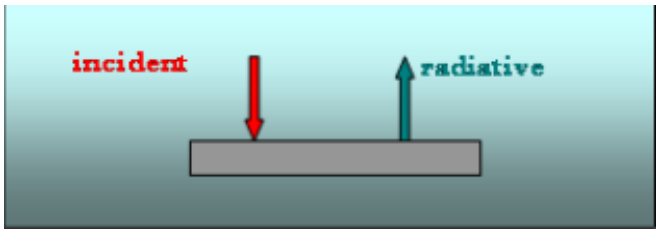

Figure 2 Passive TPS

Half-passive systems

The half-passive systems can have moving pieces (solid or fluid), but they don't have any element which burns power for this purpose.
Heat Pipe are the most famous among them, and, according to some studies, they could be able to tolerate heat fluxes values until 500 KW/m^2, which are surely less then the ones typical for *slender* bodies.
Another very important half-passive system stands in using ablative materials, i.e. materials that, when treated with high heat fluxes, absorb this energy through phase change from solid to steam (ablation) These materials have been always used as TPS of re-entering spacecrafts. Because of their degrading during the re-entry, they can be used in one mission only, and so they can't embrace the RLV-philosophy, that is the reusability.

Active systems

The active systems have both moving elements and power spending for this purpose.
Cooling fluids are generally used to chip off continuously heat from the structures, using, in particular, either transpiration cooling systems or liquid films ones or convective cooling. The formers release the fluid into the atmosphere, instead the latter take on the operative fluid, so that they can't be used at high thermal loads. These are very useful for nozzle cooling and, in this case, just the propellant can be used as cooler.

3 Ultra High Temperature Ceramics for space applications

In the continuing pursuit to improve the performance of future re-entry vehicles, Ultra High Temperature Ceramics have been considering for their higher temperature capability, which is required for vehicles with sharp leading edges. Sharper leading edges will reduce the vehicle drag, enhancing the vehicle manoeuvrability and performance, and also improve safety due to an increased cross range and larger abort window. Analysis has shown that materials with temperature capability approaching 2000 °C and above will be required for these vehicles, but the state of the art Reinforced Carbon-Carbon (RCC), material currently used on the space shuttle nose cone and wing leading edges, has a maximum use temperatures of about 1650°C (see Table 1).

One of the challenges when designing sharp leading edged vehicles is that at a given velocity, the temperature at the tip of the leading edge is inversely proportional to the square root of the leading edge nose radius. In other words, as the radius of curvature at the tip of the wing leading edge decreases, its surface temperature increases. Vehicles with sharp leading edges, that is leading edges with a nose radius smaller than the current blunt bodies such as the Shuttle Orbiter, will therefore, as mentioned previously, require higher temperature thermal protection materials.

In an attempt to bridge this temperature gap, recent experimental work is studying a subset of UHTC materials consisting primarily of Hafnium and Zirconium Diboride (HfB2 and ZrB2) ceramics. The diborides have extremely high melting temperatures (>3000°C) and have relatively good resistance to oxidation in simulated re-entry environments. In the aerospace applications, the Zirconium Diboride has an important advantage respect to Hafnium Diboride, in fact it is less dense among two, as reported in following Table 1.

Recent work at NASA Ames is focused on developing improved manufacturing methods for these materials, characterization of the materials' mechanical and thermal properties and evaluation of the materials' performance in simulated re-entry environments produced in NASA Ames Arc Jet facilities. Figure 1 shows a variety of models that have been tested in the arc jet, including nose cones and wedge models of similar geometry and scale as anticipated for use on an actual vehicle.

Figure 3 shows an image of a UHTC nose cone during arc jet testing. The surface temperature during this test exceeded 2000°C. Although the UHTC materials are considerably more dense than RCC, it is anticipated that only relatively small amounts of UHTC will be used along the vehicle leading edges so the total UHTC mass is minimized. Also, the UHTC mass is located forward on the vehicle, helping to balance the vehicle center of gravity and offset the relatively high mass anticipated for the engines at the rear of the vehicle. Some trade studies have indicated that most, if not all, of the UHTC mass is offset by the reduction in ballast required to balance the vehicle center of gravity. The UHTCs discussed here are monolithic ceramic materials composed primarily of HfB_2 or ZrB_2 with SiC additives. These represent a small portion of the UHTC family of materials and are only one of a series of potential material types that will enable the development of sharp leading edged vehicles. Other options to the UHTCs include carbon-carbon materials with higher temperature coatings and carbon fibre reinforced UHTC matrix materials. One of the most challenging topics of the UHTC components design is that these materials, which can stand very high temperature, invariably must be in contact with cooler elements of the structure. Ground based arc-jet testing and in flight experiments demonstrated the potential of these materials in reusable application at temperatures of the order of 2500 K.

On-going work includes studying the effects of composition and processing methodologies on the behaviour of UHTC materials in simulated re-entry environments and developing design methodologies to determine how best to integrate the UHTC onto a wing leading edge. UHTC

represent a class of promising materials for use in extreme applications such as sharp leading edges hot structures on future generation of slender-shaped re-entry vehicles, because of their high melting point and relatively good oxidation resistance in re-entry conditions.
Emissivity and catalicity represent key parameters for the eligibility of UHTC materials in hot structures manufacturing. High emissivity and low surface catalycity improve the material performance in re-entry conditions.
A reliable experimental evaluation of these parameters is required to feed aero-convective heating computations that, in absence of experimental data, have to rely on extremely conservative theoretical values. Moreover, the surface catalytic behaviour of the material must be fully understood in order to be able to extrapolate the structure performance in real re-entry conditions from on-ground test data obtained in arc-jet facilities.
Figure 3 shows some typical test specimen configurations in recent experimental tests at CIRA (Italian Aerospace Research Centre) (see Figure 3-a and b) and at NASA Ames Centre (see Figure 3-c).


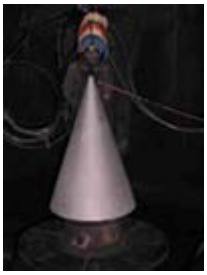


Figure 3 (a) C/Sic nose cap technology demonstrator, (b) ZrB2-SiC deposition into Plasma SprayChamber and (c) Technology demonstrator made of C/SiC substrate and ZrB2-SiC coating

3.1 UHTC features

Among UHTC, the diboride are characterised by high thermal conductibility value, reducing thermal gradients into the inner of the material; for this, on one side, the maximum temperature decreases, through heat transfer from higher temperature zones (e.g. stagnation points) to lower temperature ones, on the other side thermal shock resistance raising. Hence, using these materials, like the zirconium diboride, in the vehicle parts subjected to higher thermal loads, it can improve performances when having high heat fluxes, which are typical in the atmospheric re-entry. Zirconium diboride (ZrB_2), titanium diboride (TiB_2) and hafnium diboride (HfB_2) work well from this viewpoint. Table 1 shows, in comparison, another material used in aerospace applications: the metallic super-alloy Inconel 617.

Materials	**ρ [Kg/m^3]**	**C_p [J/(Kg·K)]**	**K [w/(m·K)]**	**Melting point [K]**	**σ [298K-1273K] [MPa]**
ZrB_2	**6000**	**628**	**66**	**3313**	**351-317**
TiB_2	**4363**	**1228**	**78**	**3193**	**473@298°K**
HfB_2	**11100**			**3523**	
Inconel-617	**8360**	**419**	**14**	**1623**	**700-100**
Carbon-carbon	**1568**			**1922-2061**	

Table 1 UHTC features

4 Design of a Flying Test Bed

4.1 Introduction

The research program EXPERT (**E**uropean e**XPE**rimental **R**e-entry **T**estbed) aimed by ESA (**E**uropean **S**pace **A**gency) is finalised to study the typical high-temperature gas dynamics re-entry conditions throughout a lot of scientific P/L (**p**ay**l**oad) on-board. Every P/L will study one or more aspects among the main re-entry hypersonic flight. The experimentation in re-entry real conditions is necessary because the on-ground experimentation is not able to reproduce the real hypersonic flow surroundings and to validate numerical models.
The utilized capsule in the frame of the EXPERT program is a revolution body ellipse-junction-cone, which geometry is reported in fig. 1.
In the frame of the EXPERT Program, a scientific payload devoted to the in flight-testing of an innovative class of high temperature materials that can be considered as potential candidate materials for new concepts of hot structures.
The objective of the technical activities is the design, manufacturing and testing of a structural sub-component represented by a small winglet made of Ultra High Temperature Ceramics.
The winglet will be designed and adequately equipped with specific sensors in order to acquire fundamental in flight information such as temperature and pressure encountered by the payload during the re-entry mission.

Operational Requirements of the Structural TPS

Main objectives of the Expert payload n.15 are the design, fabrication and testing, in real environmental conditions, of an advanced concept of hot structure (Sharp Hot Structure, SHS) based on the ultra high temperature ceramics (UHTCs).
The functional and operational requirements of the Expert scientific payload n.15 are reported below:

a. To be mounted on the capsule interfacing the system mechanically and electronically.
b. To test UHTC structural component in hypersonic re-entry conditions:
c. specific total enthalpy > 10 MJ/Kg
d. stagnation point heat flux (cold wall hypothesis) > 5MW/m^2
e. To compare the in flight measured temperatures, with those estimated from numerical thermal model used for the design, thus assessing the foreseen material surface emissivity, catalicity, and thermal conductivity.
f. To compare flight results with on ground facility test results obtained at similar hypersonic conditions.

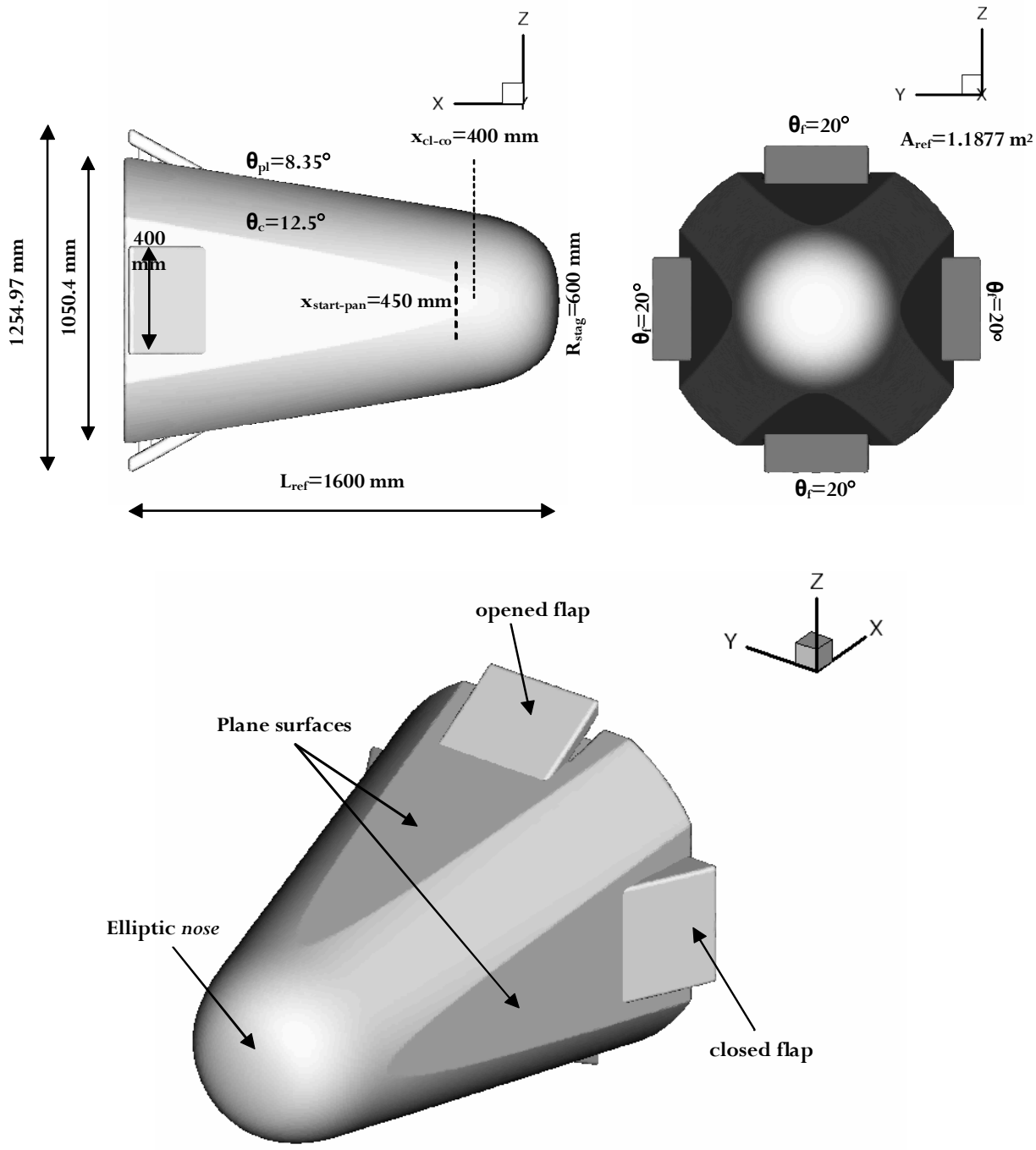

Figure 4 EXPERT configuration

4.2 Design of the Structural TPS

The Winglet external shape is designed in order to achieve significant temperatures at the tip of the winglets and in order to prevent unacceptable heating at the interface with the capsule.
The Winglet has a double delta shape (see Figure 5 and Figure 6) and are tapered. In the figures 1 and 2 there are reported dimensions and external shape of the winglet, too.
The winglet leading edge forms an angle of about 26 degrees with the surface of the capsule and has a curvature radius of 20 mm at the root and 10 mm at 15 mm from the capsule surface. Above this distance, the angle with the wall is increased to about 54 degrees and the curvature radius of the leading edge decreases to 5 mm at the tip.
The winglet is made of UHTC leading-edge connected to an ODS (**O**xide **D**ispersion **S**trengthened) support, e.g. the superalloy PM1000.
Two winglets of UHTC materials will be placed on the capsule wall in diametrically opposite positions (see fig. 3), preserving the symmetry of the re-entry capsule, in order to study the influence of different material properties (thermal conductivity, surface emissivity, catalytic efficiency).

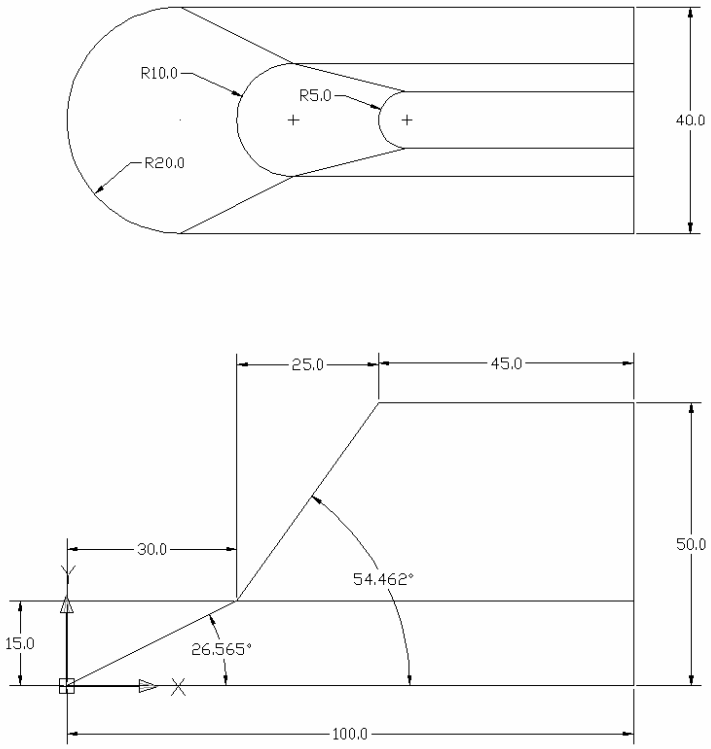

Figure 5 Drawings of the external shape of the Winglet

The possibility to locate the winglet at a sufficient distance from the back of the capsule will be considered, to avoid the interaction with the base flow and in case of space limitation due to the launcher configuration.

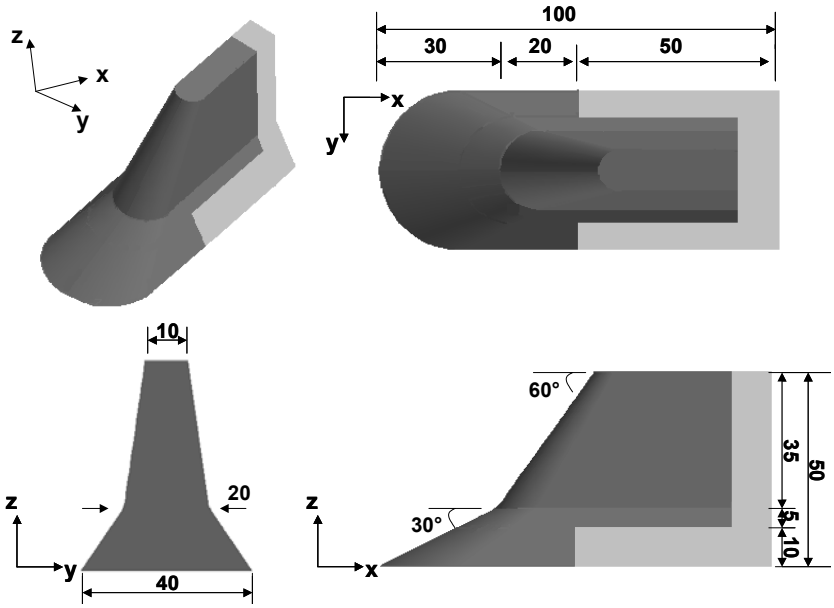

Figure 6 the winglet geometry

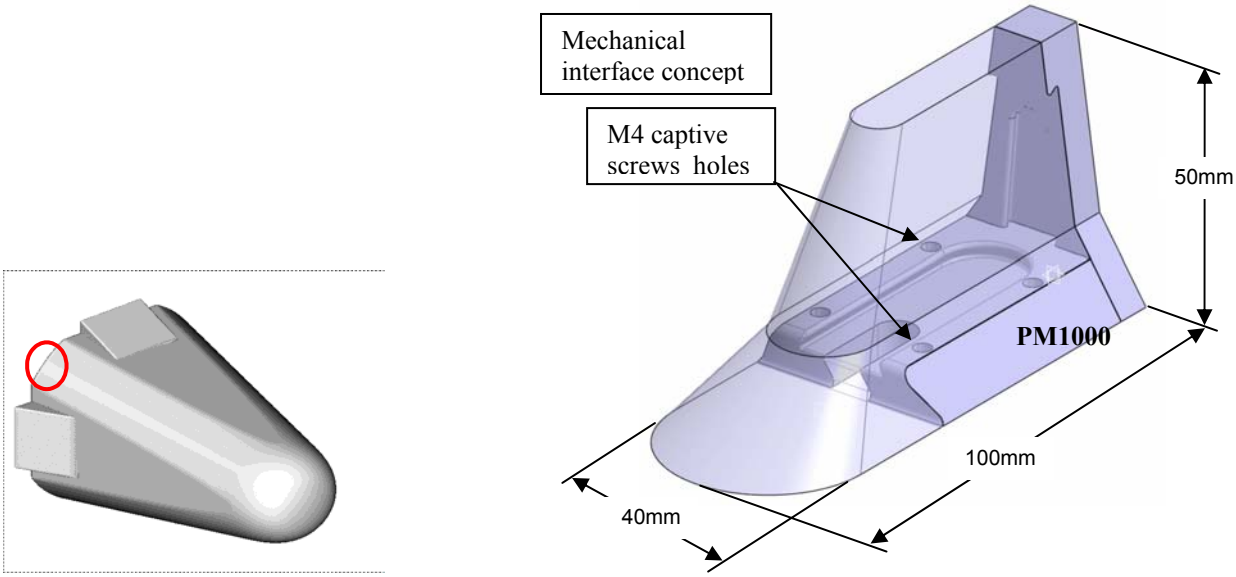

Figure 7 a) winglet position on the surface's capsule and b) 3D winglet

Reference trajectory

The capsule is expected to fly along a predefined re-entry trajectory.
The point of the trajectory corresponding to the maximum heat flux condition has been considered for the 3D CFD computations of the aerodynamic field around the winglet.

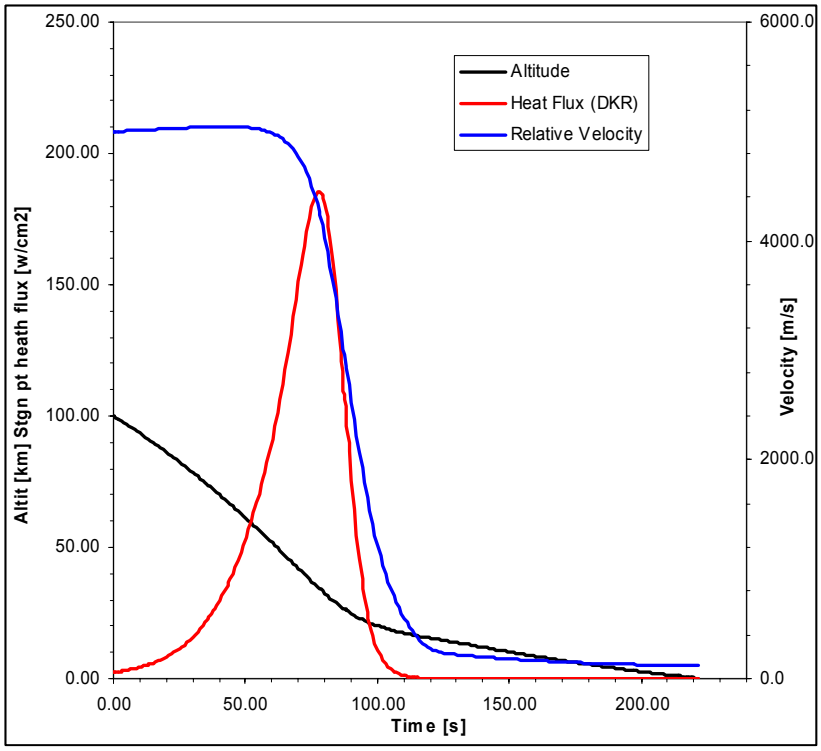

Figure 8 Reference 5Km/s entry speed trajectory of the capsule (mission 1)

CFD analysis.

The CFD computations, performed for the 5 km/s entry speed trajectory, have been carried out for the maximum peak heating condition along the re-entry (Z=34 Km, M=14) and under the assumption of an isothermal 3D winglet (T_w=300K) and an isothermal capsule surface (T_w=300K). To impose appropriate inlet boundary conditions axi-symmetric field computations at the winglet locations have been performed. In particular, the computations have been carried out based on the following input data:

a. Reference Geometry
b. Reference trajectory
c. The distributions of the main aero-thermodynamic variables at the winglet location plane, corresponding to the maximum heat flux conditions along the reference trajectory.

Because the final position of the winglet is not yet consolidated, the inlet boundary conditions have been evaluated at two stations (x=1.12 m and x =1.20 m) along the surface of the capsule, as shown in Figure 9. In this figure, the x-coordinate represents the stagnation point distance.

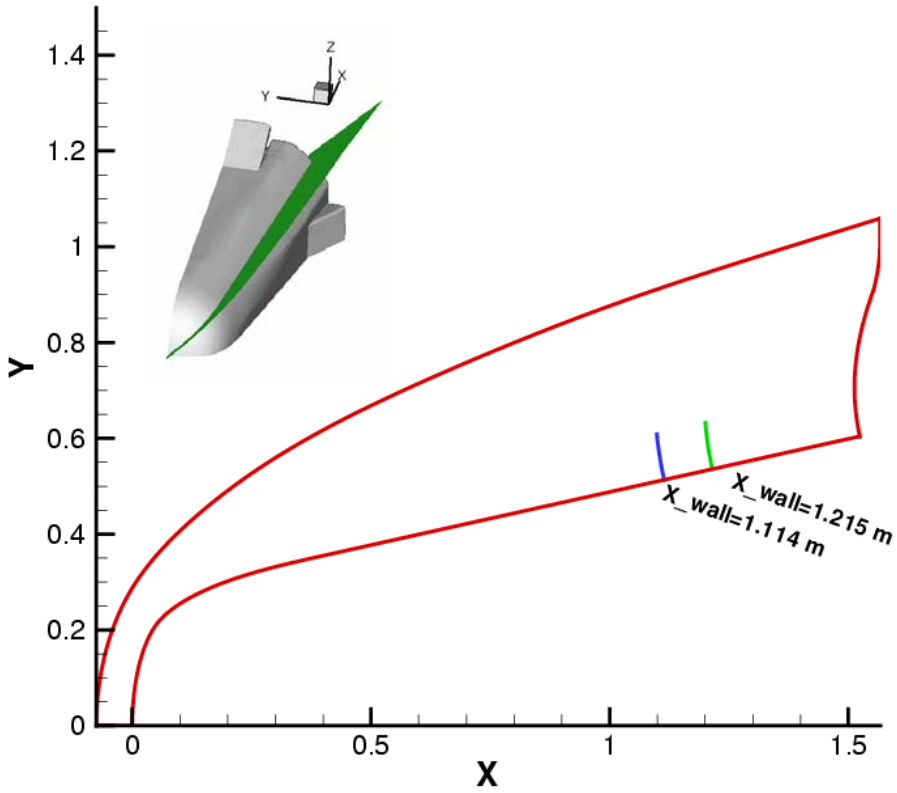

Figure 9 Position on the capsule of the input parameters for 3D CFD

The profiles of the Mach number, of the temperature, of the pressure and of the concentration of atomic Oxygen in correspondence of the two considered stations along the capsule are shown in Figure 10. As shown in these figures, the differences in the flow field distributions at the two positions are negligible. In particular, the CFD computations have been performed with the profiles characterized by the highest pressure value corresponding to the distance of 1.12 m from the capsule stagnation point.

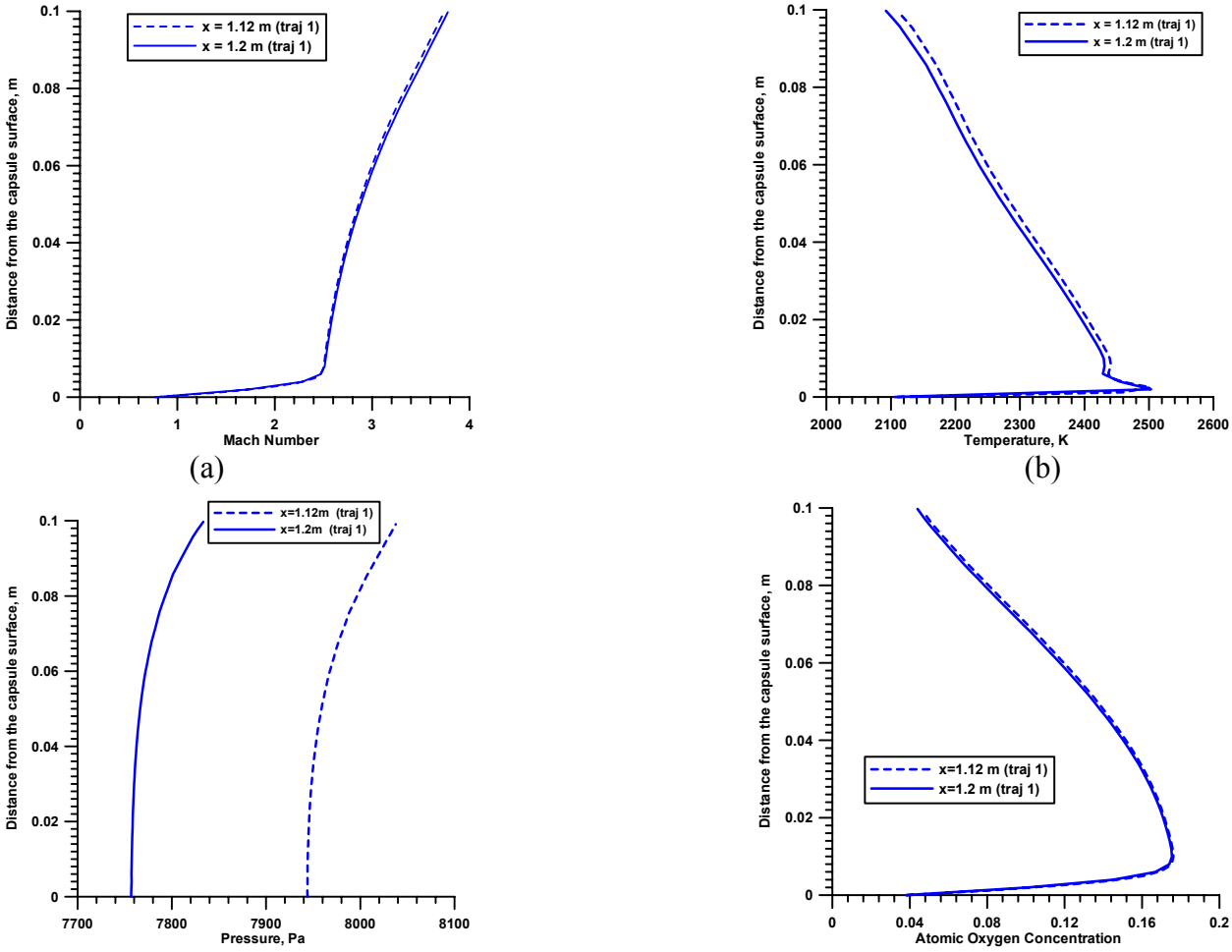

Figure 10 Comparison of Mach number profiles (a), temperature (b), pressure (c) and atomic Oxygen mass fraction (d) in the two points chosen as input for CFD analyses

Figure 11 and 12 show the heat fluxes distributions at the maximum heat flux condition under the assumption of fully catalytic and non catalytic wall.

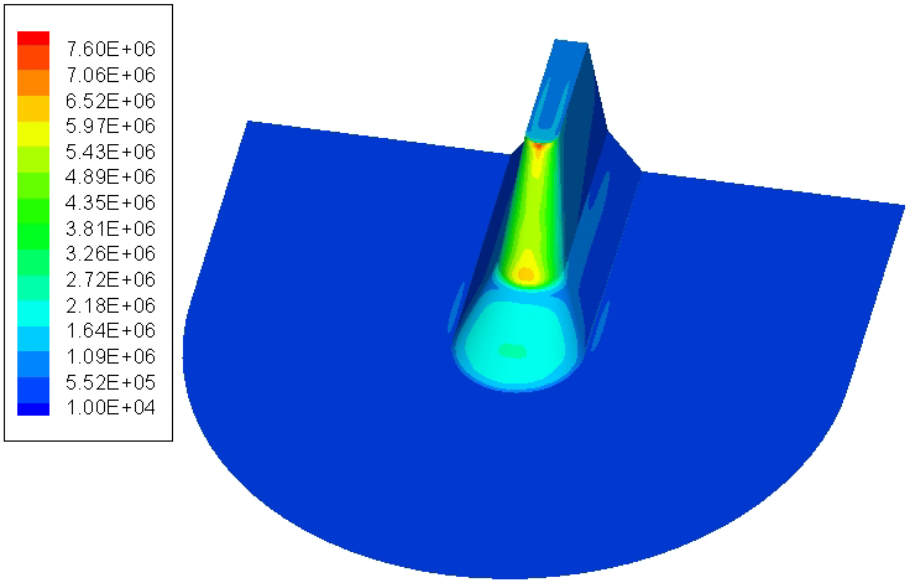

Figure 11 Surface heat flux contours (W/m^2), M=14, Z=34 km Fully catalytic wall

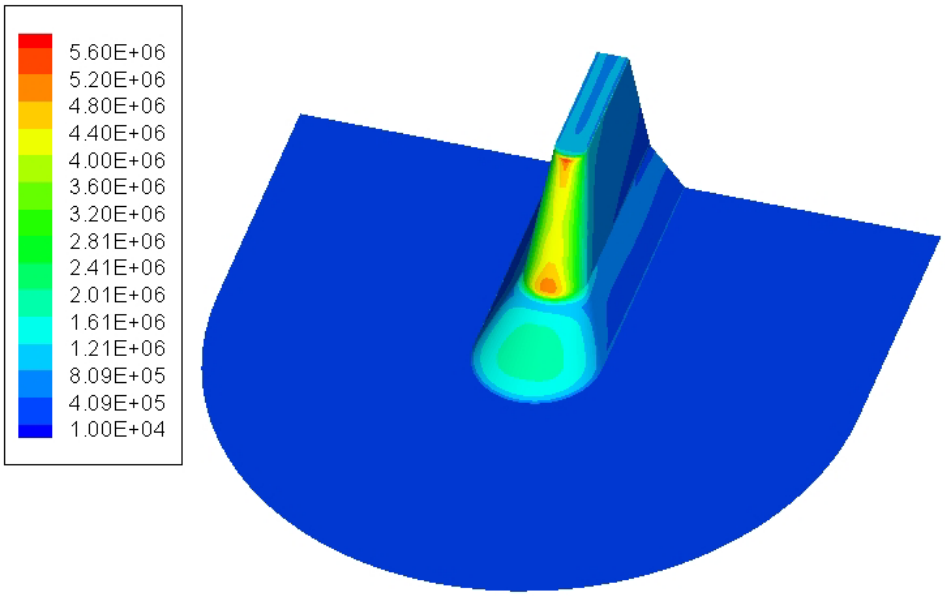

Figure 12 Surface heat flux contours (W/m^2), M=14, Z=34 km Non catalytic wall

It must be pointed out that the effect of a non catalytic wall is to reduce the maximum heat flux from 7.6 MW/m^2 to 4.9 MW/m^2.

Figure 13 shows the surface pressure distribution that is almost the same for the fully and non catalytic wall condition.

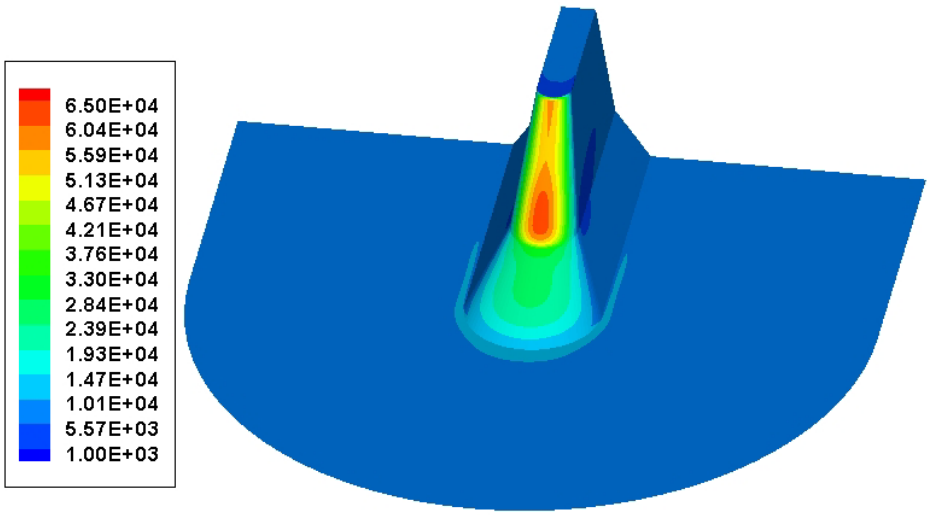

Figure 13 Pressure contour (Pa), Mach 14, Z=34 km

The following table summarizes the maximum pressures and heat fluxes for the analyzed conditions.

Test Case	Heat Flux [MW/m^2]	Pressure [Pa]	γ_w
fully catalityc wall	**7.6**	**63000**	**1**
partially catalityc wall	**6.1**	**63000**	**0.05**
partially catalityc wall	**5.3**	**63000**	**0.005**
partially catalityc wall	**5.1**	**63000**	**0.001**
non catalityc wall	**4.9**	**63000**	**0**

Table 2 Maximum pressures and surface heat fluxes for fully catalytic, partially catalytic and non catalytic wall

Winglet thermal analysis

In order to evaluate the temperature of the winglet, it is necessary to combine the CFD analysis with a thermal model of the structure. The computations have been carried out based on the heat fluxes distributions for a fully catalytic and a non catalytic wall. The properties of the considered materials both for the winglet (ZrB_2 and PM 1000) and for the capsule TPS (PM 1000) are reported in table 10. The heat transfer equation solve in the structure assuming as boundary condition a time dependent surface heat flux given by the difference between the convective heat flux and the radiative heat flux at each time. This computation provides the new surface temperature distribution that is then input to update the surface heat flux at the flight condition of the next time step.

The temperature distributions shown in Figure 14 correspond to the time (t=115s starting from an initial altitude of 100km, see Figure 8) at which the maximum surface temperature occurs at the tip of the leading edge. In both the computations the capsule surface has been considered fully catalytic with a thickness of 2.5 mm. The maximum value of the surface temperature is about 2520K for a fully catalytic wall and about 2000K for a non catalytic wall. In any case, the temperature of the metallic support does not exceed its maximum allowable value (1480 K).

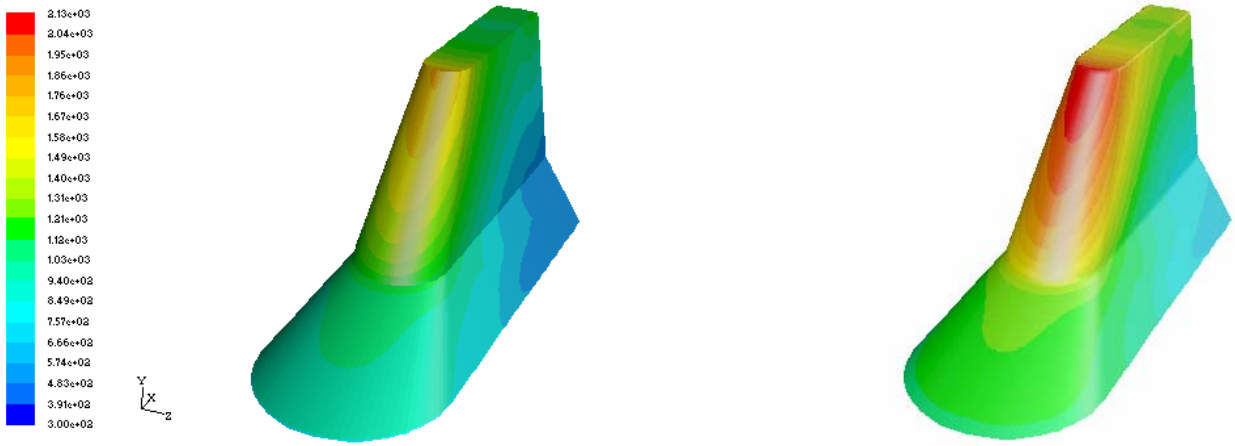

(a) (b)

Figure 14 Temperature distributions on the winglet for fully (a) and non catalytic (b) condition at time t=78s

Material	ρ [Kg/m^3]	c_p [J/Kg K]	λ_s [W/m K]	ε
ZrB_2	5610	459	103.8	0.775
PM 1000	8240	432	11.5	0.6

Table 3 Material Properties

Effect of the SHS payload on the heat fluxes on the EXPERT metallic TPS

A typical fin interaction phenomenon could be observed at the conjunction between the winglet and the capsule surface. In this flow field the boundary layer separates due to the adverse pressure gradient caused by the shock wave and reattaches downstream. In the reattachment region quite high peak heating are expected. A focal point for the payload development is that the peak heating can be sustained by the capsule TPS. The steady results obtained by CFD computation in the most severe heating condition (Z=34 Km M=14) for a cold wall (T_w=300) are shown in Figure 15 and Figure 16 both for a fully catalytic and a non catalytic wall.

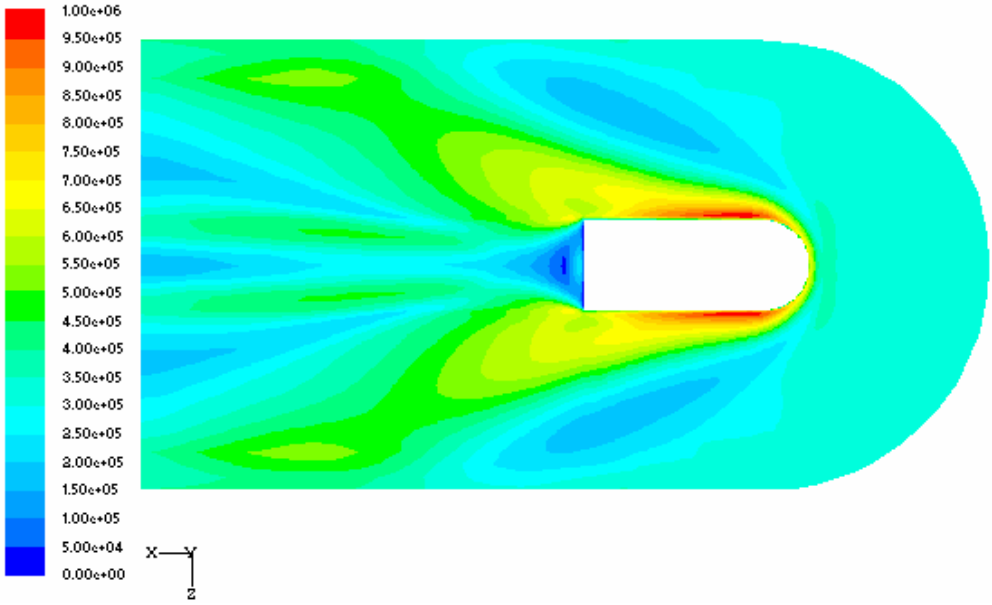

Figure 15 Surface heat flux on the capsule surface: fully catalytic wall

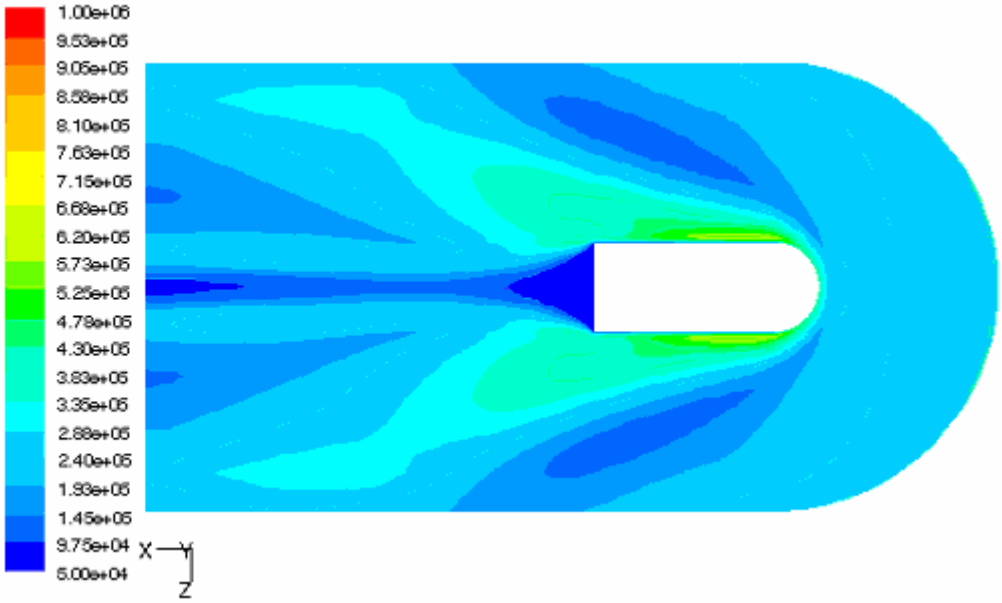

Figure 16 Surface heat flux on the capsule surface: non catalytic wall

To evaluate the heat loads during the trajectory an unsteady thermal analysis has been carried out. The thickness of the metallic TPS is 2.5 mm, and the backward surface condition is cold

temperature T_w = 300 K. The capsule wall (PM 1000) has been considered fully catalytic and two different assumptions (fully catalytic and non catalytic) have been considered for the UHTC winglet. This choice is supported by experimental analysis.
Figure 17 and Figure 18 show the temperature distribution on the capsule wall at t=120s corresponding to the maximum temperature conditions. Figure 17 refers to the case of the plate and the winglet both fully catalytic; Figure 18 refers to the case of plate fully catalytic and winglet non catalytic.

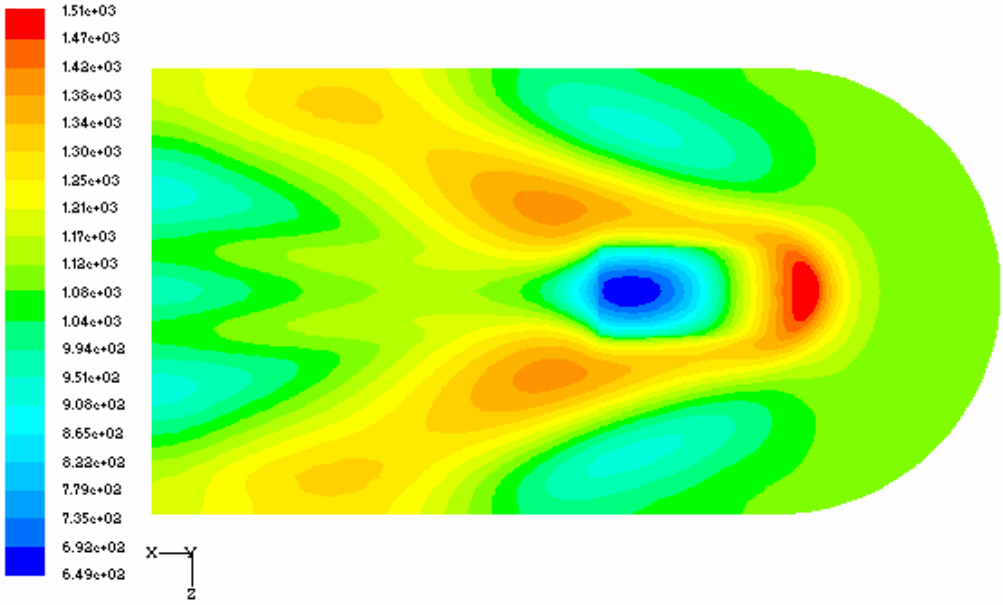

Figure 17 Temperature [K] on the capsule surface at t=120s. Fully catalytic plate-fully catalytic winglet.

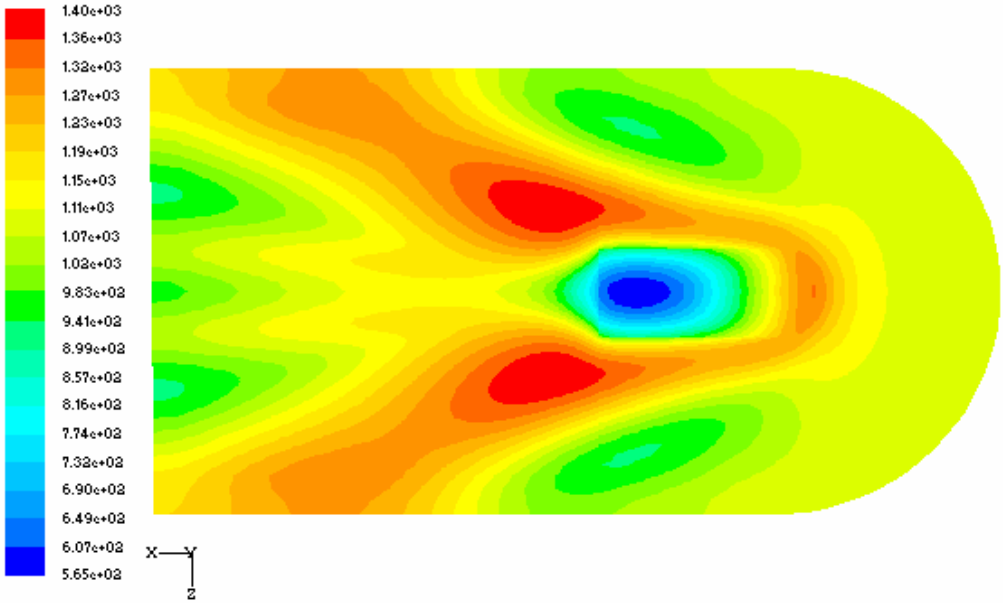

Figure 18 Temperature [K] on the capsule surface at t=120s. Fully catalytic plate-non catalytic winglet.

In the more realistic situation that the UHTC material is supposed to be non catalytic, as obtained by preliminary experimental results on ZrB_2, the conductive heat fluxes from the winglet to the plate are lower and the maximum surface temperature is consequently lower than 1400 K. If the PM 1000 is considered fully catalytic the temperature on the metallic TPS achieves locally a

temperature between 1500 K and 1600 K for about 10 seconds after the peak heating, while, If the PM 1000 is supposed to be non catalytic, the surface temperature is much lower than 1400 K, as shown in Figure 18.

Proposed sensors collocation

Numerical results are also important for the definition of the payload sensors locations. Figure 19 and Figure 20 show the distributions of temperature and pressure on the leading edge in the most severe conditions of the re-entry trajectory.
These distributions are used as a guideline for the collocation of the sensors in such a way to optimize the investigation of the aerodynamic effects around the winglet.

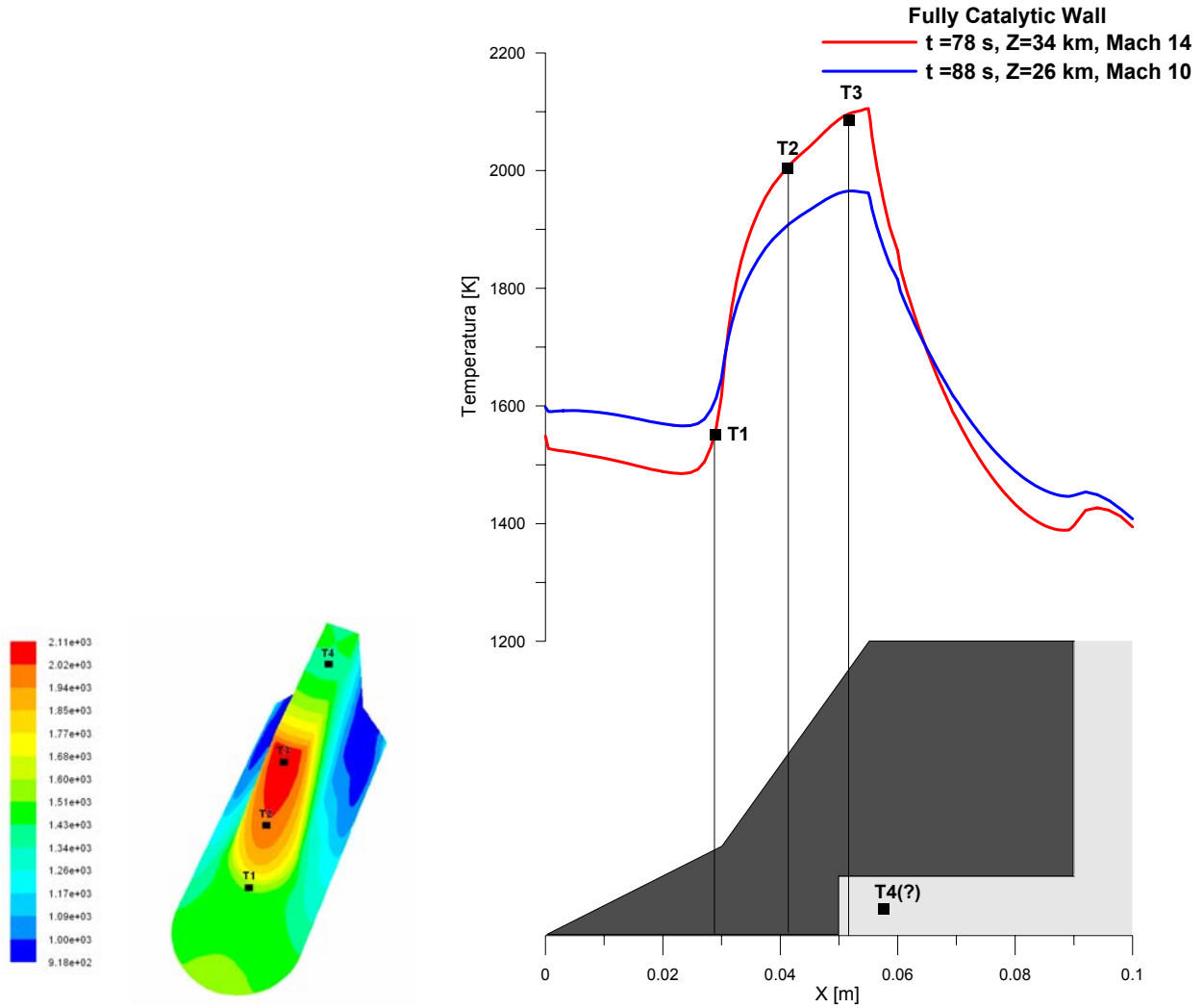

Figure 19 Temperature distribution on the leading edge for the 5km/s trajectory for fully catalytic condition and proposed measurement points

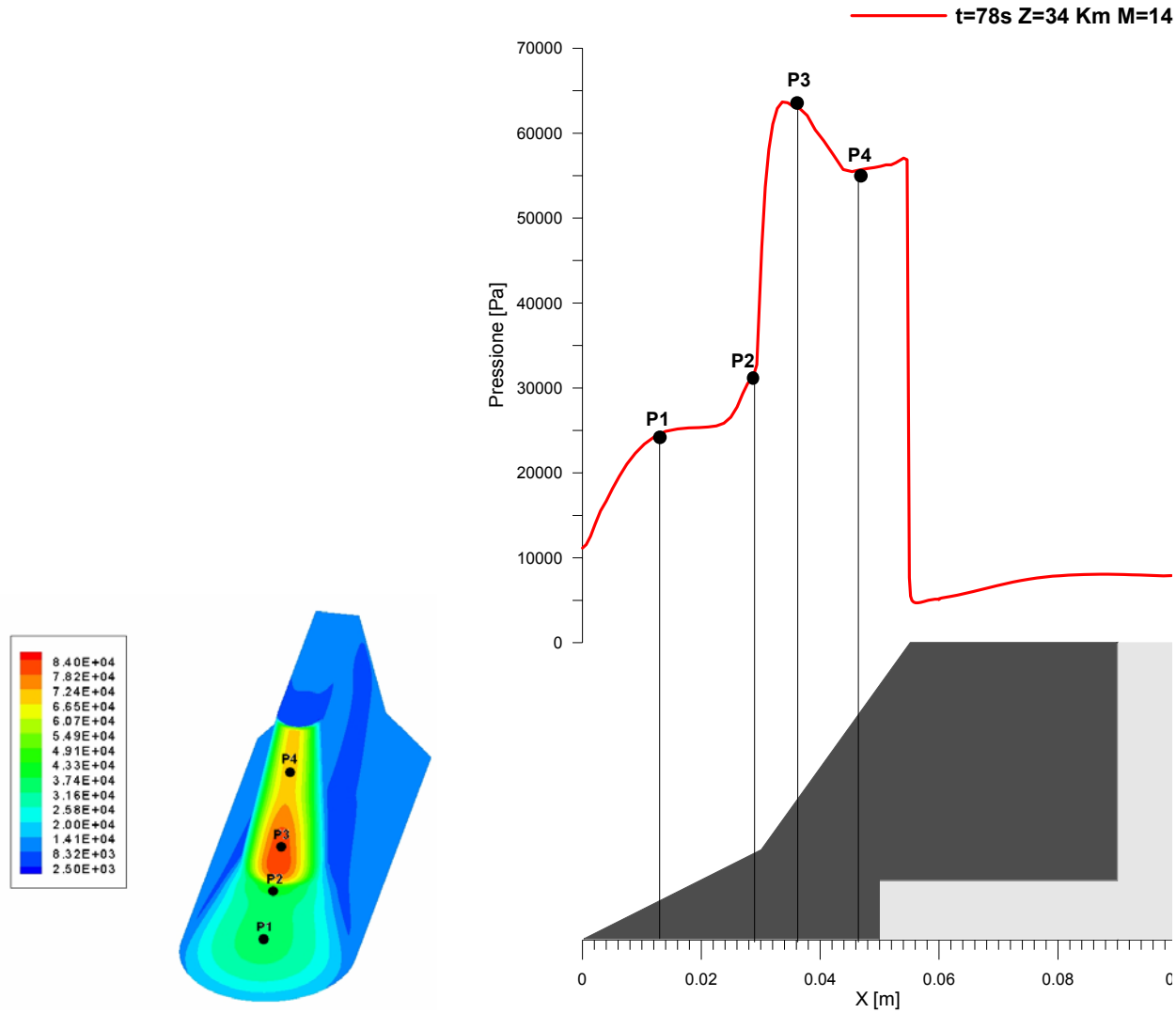

Figure 20 Pressure distribution on the leading edge and proposed measurement points

The designed layout is consistent with the flight test objective in order to assess the resistance to the oxidation at very high temperatures of the selected UHTC materials. Moreover, the structural architecture of the winglet is compliant with the thermal constraints of the metallic support. In fact the temperature profile estimated decrease through the thickness to values compatible with the selected materials.

4.3 Conclusions about Design Flying test Bed

Upstream conditions for the 3D computation around the winglet have been obtained by axial-symmetric thermo fluid-dynamic fields. Because the final collocation of the winglet has not yet been defined, different positions have been considered. It has been concluded that the position of the winglet on the capsule surface affects very marginally the aerodynamics around the winglet.
The CFD computations have produced heat flux distributions on the winglet and on the capsule surface under the conservative hypothesis of cold wall (T_w = 300 K), in fully catalytic, partially catalytic and non-catalytic wall conditions. The chosen re-entry trajectory reduces the thermal loads with respect to the preliminary trajectory (entry speed of 6 Km/s) used in the phase A. Anyway, the heat load continues to be high enough to guarantee the scientific validity of the experiment of UHTC materials in real flight conditions.
The pressure distribution has been computed along with the heat flux distribution, and will be considered in the thermo-structural analysis for the design of the winglet.
The heat fluxes induced by the interaction between the winglet and the capsule metallic TPS have been evaluated and a preliminary thermal analysis has been carried out. The evolution of the temperature on the metallic skin structure show locally on the TPS temperatures between 1500 K and 1600 K for about 10 seconds after the peak heating for a fully catalytic wall. For a non-catalytic wall, a maximum temperature on the skin structure of about 1350 K is achieved.
Setting shape's winglet and its position on capsule, we consider the choice of more suitable material to flying test. The more interesting material's properties are the spectral emissivity, surface catalicity and resistant to the surface oxidation. The relevance of the previous properties will be clarified in the following discussion. The under consideration material is ZrB_2 + SiC, that has an high melting point and it seems to have a good resistance o surface oxidation by means of the SiC added to zirconium diboride.

5 Spectral Emissivity Evaluation

5.1 Spectral and Total Emissivity at Near Ambient Temperatures

Emissivity is the ability of an object to emit or absorb energy. Perfect emitters have an emissivity of 1, emitting 100% of incident energy. An object with an emissivity of 0.8 will absorb 80% and reflect 20% of the incident energy. Emissivity may vary with temperature and wavelength.
Spectral emissivity over the thermal infrared wavelength (3 μm to 60 μm) is a key property to determine energy transfer. The reliable prediction of energy gains and losses to and from such structures has become an important aspect of energy conservation and control.
Over the thermal infrared spectral region, the spectral emissivity is related to the diffusive and specular components of reflectance and transmittance of the target (see Appendix A).

5.2 Radiative equilibrium temperature

During re-entry, sharp-body are subject to high heat flux, to which corresponds temperature high enough to make relevant the contribution to total thermal flux. The definition of radiative heat flux is: $\dot{q}_r = \sigma \cdot \varepsilon \cdot T_w^{\,4}$, where σ and ε are the Stefan-Boltzmann constant and the surface emissivity, respectively, and T_w is the surface temperature.
The radiative equilibrium temperature will be as less as material higher emissivity, as represented in Figure 21. The radiative equilibrium definition is: $\dot{q}_c = \dot{q}_r$.

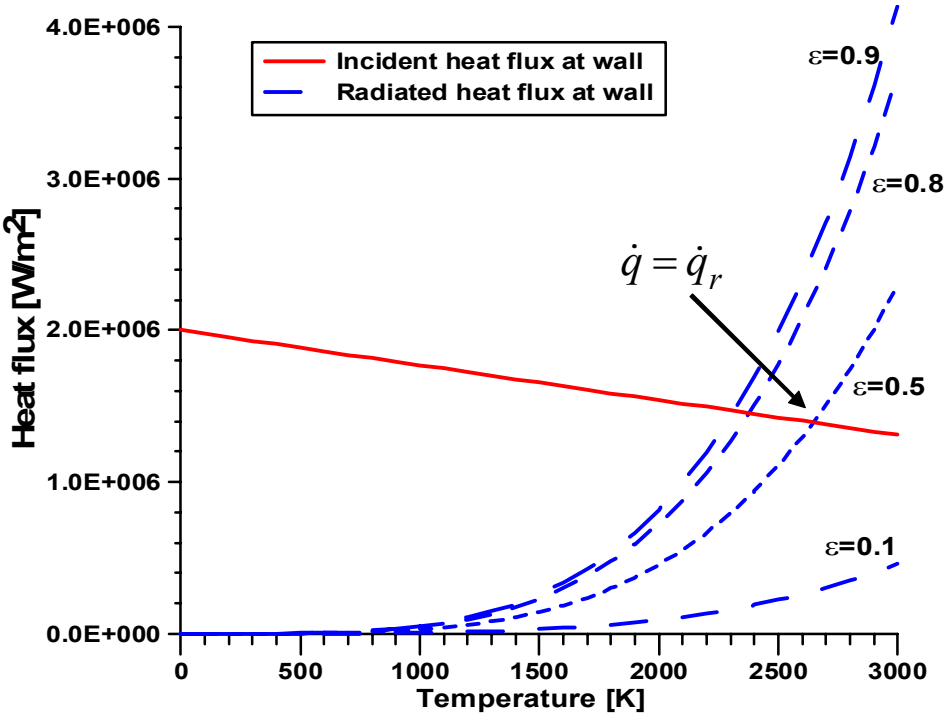

Figure 21 Radiative equilibrium temperature

The advantages, in raising to raise the radiative equilibrium wall condition, are that the amount of radiative heat flux became equal to convective incident heat flux at wall.

5.3 Measuring error to emissivity

For a thermal-sensor, to measure correctly temperature, you must know what is the emissivity value to enter. This is not always easy, because many different things affect the emissivity value you must enter. The following is a partial list of things that affect emissivity to enter:

a. Even very thin coatings on the surface can affect the emissivity value of the surface and the correct emissivity value may be that of the coating, not the main substrate. Very thin coatings (such as oxides or oils) can act as "interference filters" that cause the emissivity to vary widely depending on exact film thickness.
b. The microscopic and macroscopic roughness of the surface causes differences in emissivity simply because a rougher surface has a larger emitting area. Generally, the emissivity of most opaque emitting surfaces increases as wavelength becomes shorter.
c. The geometric shape of a surface affects the required emissivity setting. Convex surfaces such as cylinders or balls have emissivity values that drop with increased curvature simply because they spread their radiation over a wider angle. Concave surfaces such as the inside of a bowl or box have emissivity higher than the expected one.
d. The angle from normal (straight on or 90°) at which the surface is viewed, especially for specular (mirror-like) or semispecular (dull reflection as from a smooth metal) surface will cause emissivity to start dropping rapidly at any angle beyond about 45° as such surfaces do not emit equally at all angles. This is less of a problem with non-reflective surfaces except at long wavelengths. Also, be cautioned that viewing a surface at more than about a 30° angle from normal may cause polarization effects, and some thermal-sensors are sensitive to such effects.
e. If a thermal-sensor views a surface through a window, which is sometimes necessary, there will be both absorptive and reflective radiation losses depending on window thickness, window material and viewing angle. These losses will require the use of an emissivity setting lower than normal.
f. If the sight path between the thermal-sensor and the surface is partially obscured by smoke, steam, water droplets or particulate matter, all they may reduce the radiation received by the thermal-sensor. Ratio thermal-sensors or Peak picking techniques (covered under signal processing) are better methods.

5.4 The procedure for emissivity and temperature estimate

The pyrometer connects to pc by serial gate by means of dedicated software. In the dual colour mode, the temperature of the 3mm diameter spot (framed by the pyrometer) is acquired. The temperature, measured by the pyrometer ratio, is used to evaluate the spectral emissivity by means of single colour measurements ($\lambda = 0.9$ μm).
Switching from the dual colours mode (thermometer) to single colour mode (radiometer, 0.92 μm), the radiance and the temperature corresponding to a preset value of ε (e.g. 1) are acquired. During the post-processing of the data, the values of temperature get from the pyrometer are transferred to a simple procedure that elaborates them in the following mode. The basic assumption of a dual colour pyrometer is that the target is at least a grey-body, overcoming the problem of emissivity since it is supposed to be the same at both wavelengths. Measuring spectral radiances on two overlapping bands then provides a unique couple temperature/emissivity solving the following system based on Plank's equation.

a. The value of temperature $T_{\lambda=0.92}$, measured in the single colours mode, draws the radiance, assigning the value of unity to the emissivity and the value of 0.92 μm to the wavelength.

$$I_{\lambda,T} = \frac{C_1}{(0.92)^5 \left[\exp\left(\frac{C_2}{0.92 \cdot T_{0.92}} \right) - 1 \right]} \quad (1)$$

b. From the equation (1), the unknown ε(λ=0.92μm, T) is calculated by the inverse equation:

$$\varepsilon_{\lambda,T} = \frac{I_{\lambda,T}}{C_1} \lambda^5 \left[\exp\left(\frac{C_2}{\lambda T} \right) - 1 \right] \quad (2)$$

assigning to λ the value of 0.92 μm, to $I_{\lambda,T}$ the radiance calculated to the point (a) and to T the value of the temperature measured during the operation of the pyrometer in dual colour mode.
Figure 22 shows a typical pyrometer output. The initial set up value for the emissivity at the wavelength of 0.92 μm is irrelevant for the calculation of the emissivity. The hypothesis of grey body (i.e., k=1), in the range of the wavelengths of interest (0.92 μm and 1.06 μm), is justified by literature data for the ceramic materials.

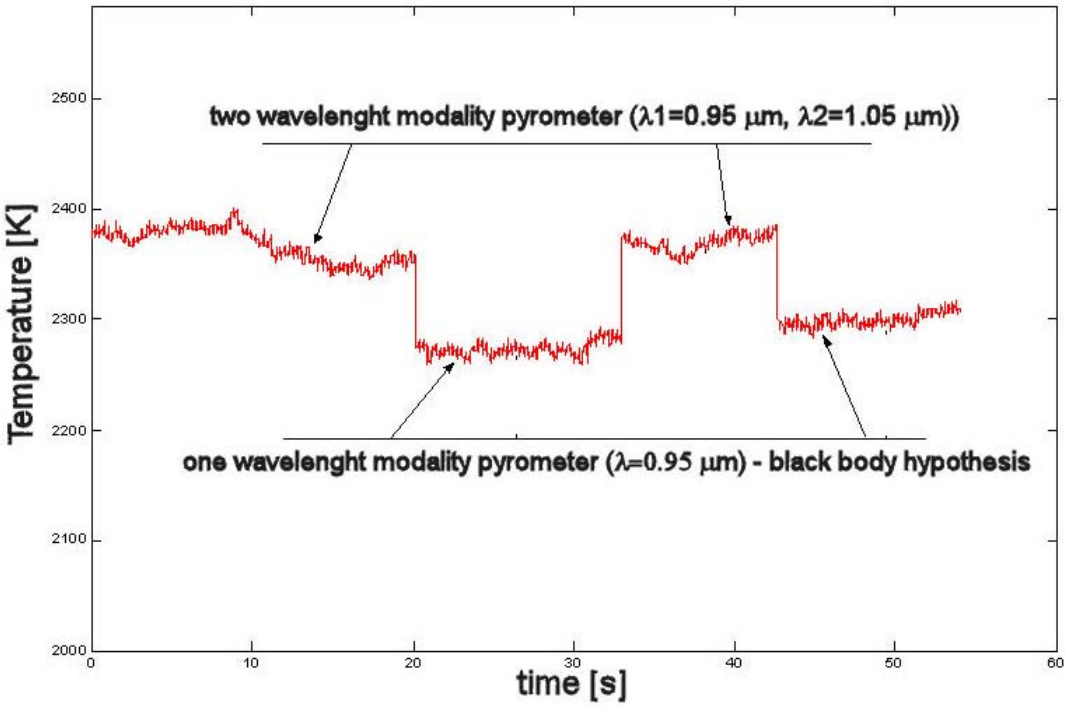

Figure 22 Temperature measured by the single colour and double colour mode pyrometer

6 Surface Catalicity Evaluation

6.1 Catalytic heating effects

Catalytic heating effects are of paramount importance in the modelling and simulation of re-entry problems. In fact, for the flight trajectory segments characterized by large values of Mach number, diffusion and recombination of atomic species on the surface can represent a consistent part of the total heat flux. The assumption of a non-catalytic surface can lead to strong underestimation of the thermal load to the vehicle's thermal protection system, the reverse being true for the assumption of fully catalytic behaviour of the vehicle surface. Adequate catalicity model must be therefore developed and inserted into CFD tools to realize accurate estimates of vehicle surface heating, with the final goal of helping TPS designers both in the design phase and in the post-flight data analysis.

6.2 Definition of recombination coefficient

The recombination probability is ratio of recombination acts on the surface of unit area per unit time to the total number of atoms collisions of current sort with unit surface per unit time interval. The following expression for effective probability of recombination in dissociated air:

$$K_{wi} = \gamma_{wi} \cdot \sqrt{\frac{R_0 T_w}{2\pi M_i}} \tag{3}$$

The heat flux measured on the investigated materials has been used to calculate the recombination rate constant on the material surface and eventually to calculate the recombination coefficient.
In the Figure 23, there is a representation of the catalytic surface effect on the surface heat flux.

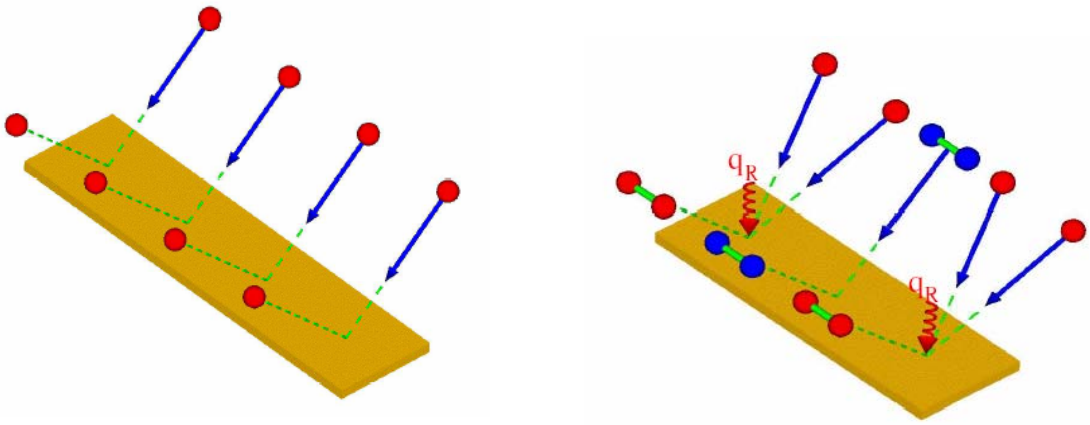

Figure 23 Surface catalytic and non-catalytic effect

6.3 The catalytic efficiency of thermal protection system

Development of reusable space vehicles requires a precise qualification of their thermal protection system materials. The catalytic properties are usually determined in plasma wind tunnels for test conditions relevant to the flight mission program. Therefore, for such a situation, it is important to have a methodology that allows the correct extrapolation of the ground test

conditions to the real flight ones. The catalytic efficiency of thermal protection system defines the finite catalytic reaction rates of gases in chemical non-equilibrium on the material surface. During re-entry, the airflow molecules oxygen and nitrogen, with respective dissociation energies of about 500 kJ/mol and 950 kJ/mol, passing through the bow shock and dissociated. The atoms can then recombine with different rates (depending on catalytic efficiency of TPS materials) to molecules on the TPS surface or in the gas phase. Due to transfer of the recombination energy to the material surface the heat flux on the re-entry vehicle depends on catalytic efficiency of the thermal protection system materials (see Figure 23). Since the catalytic properties of these materials depend on temperature, the heat flux indirectly depends on the vehicle surface temperature and, consequently, on the thermal emissivity of the TPS materials. Therefore, for the accurate prediction of thermal loads during re-entry and for the lightweight design of the TPS it is important to know both the catalytic efficiency and the emissivity of the material used.

6.4 Determination of recombination coefficient

The computation of aero-thermal field has been performed with a numerical code for hypersonic reacting flow. A numerical thermal model of the specimen has been developed to simulate the evolution of thermal field taking into account the conductivity. The thermal field in the specimen is obtained from the walls heat flux through a numerical unsteady simulation from the walls heat flux. The walls have an initial temperature of 300 K. In Figure 24 heat fluxes on the model are shown.

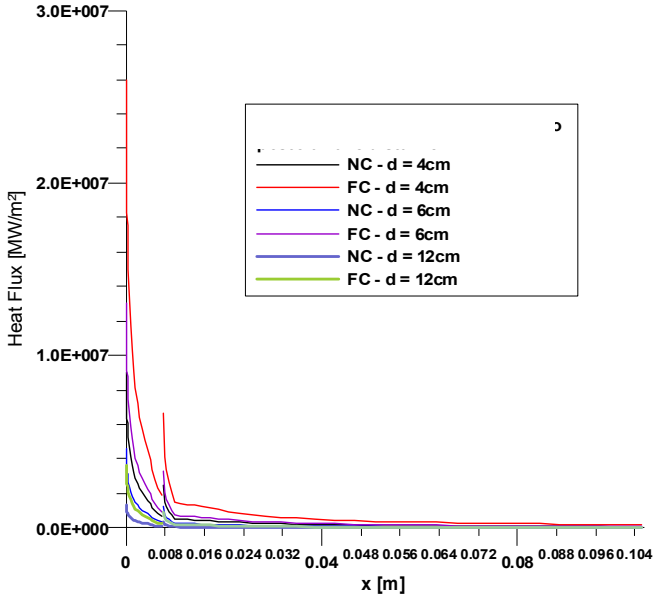

Figure 24 Surface specimen heat flux at different distances from torch exit

In Figure 25 a typical thermal field in the model is shown. For the joining with the field of local temperature in the solid ($\lambda s \neq 0$), the wall temperature is obtained imposing the local balance among the convective, conductive and radiative heat fluxes, through the following relationship

$$\left(\lambda \frac{\partial T}{\partial n} + \rho \sum_i \varphi_i D_i h_i \frac{\partial c_i}{\partial n} \right)_w - \sigma \varepsilon T_w^{\,4} = \lambda_s \left(\frac{\partial T}{\partial n} \right)_{s,w} \tag{4}$$

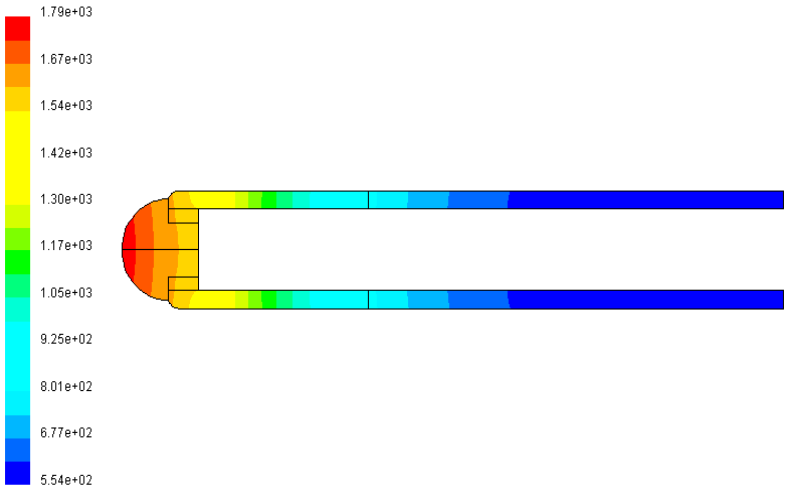

Figure 25 Temperature distribution model

To get temperatures sufficiently high (about 2000 K), after this kind of numerical analysis the model is tested at a distance of 5 cm from the torch exit.
The numerical-experimental correlation allowed a preliminary characterization of surface catalicity of the specimen, in Figure 26 the case of UHTC (ZrB_2 + SiC) is represented.
As shown in the Figure 26, the experimental results match quite well the numerical ones with non catalytic wall condition, hence, UHTC materials seem to exhibit a non catalytic nature.

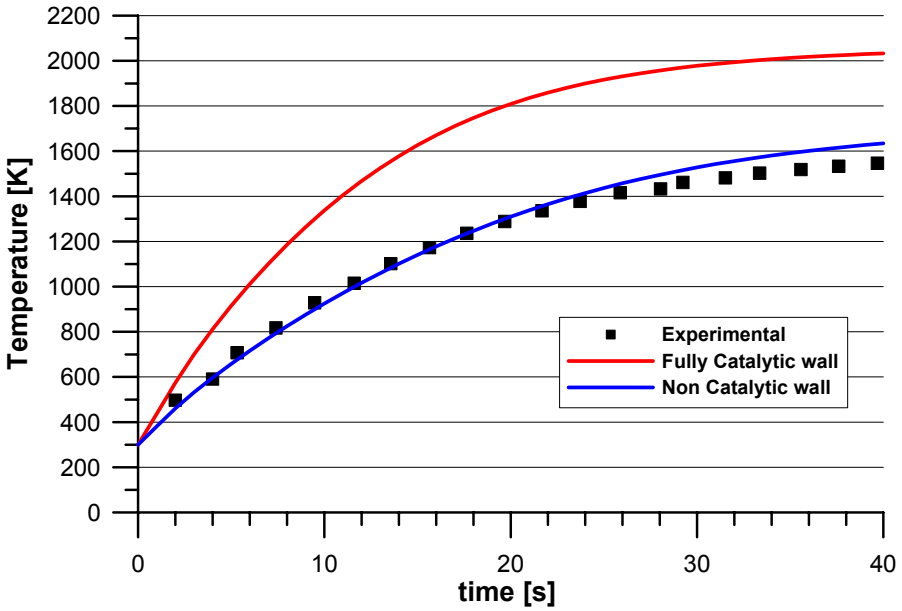

Figure 26 Temperature varying with time, 3 mm point from stagnation point

This approach of catalicity determination makes use of dedicated experimental procedures, combined with accurate computational fluid dynamics of the flow field inside the ground facility.

7 Experimental Apparatus

7.1 Description of the SPES facility

The SPES (Small Planetary Entry Simulator) facility, located in the laboratory of the DISIS (Dept. of Space Science and Engineering), University of Study "Federico II", Naples, Italy, is a continuous, open-circuit, blow-down arc facility. It is equipped with:

- A 80 kW plasma torch that operates with inert gas (He, N_2, Ar and their mixture) at mass flow rates up to 5 g/s. Specific total enthalpies up to 18 MJ/kg are achieved at gas mass flow rate of 1g/s.
- A convergent-divergent nozzle where the flow expands to a nominal Mach number of 4.8. All heater and nozzle components are cooled with demineralised water.
- A test chamber with infrared and optical windows.
- The vacuum system is a three stage system composed by mechanical pumps and two boosters allowing a pressure below 100 Pa, which is necessary for the ignition of the arc heaters.
- Swirl mixer where a second gas can be supplied to obtain desired atmosphere composition can be used.
- Automatic control system allows monitoring the facility main parameter (Arc heater voltage and current, water cooling temperature, mass flow rate and pressure).

One of the main subcomponents of the facility is the plasma torch; with arc voltages of the order of 50-60 [V] and arc current in the range between 200 and 400 [A], specific total enthalpies up to 20 MJ/kg can be achieved at a gas mass flow rate of 1g/s.
The flow is characterized by evaluation of specific total enthalpy at the exit nozzle by means an energy balance between the energy supplied to the gas by arc heater and the lost energy through the cooling system. It is possible to obtain an average value at the nozzle exit with the following formula:

$$H = \frac{VI + c_{pg1}\dot{m}_{g1}T_{g1}^{i} + c_{pg2}\dot{m}_{g2}T_{g2}^{i} - c_{pw}\dot{m}_{w}\Delta T_{w}}{\dot{m}} \tag{5}$$

Where H is the average total specific enthalpy at the nozzle exit, VI is the supplied power to the gas by arc heater, $\dot{m}_{g1}$ and $\dot{m}_{g2}$ are gases mass flow rate, and $\dot{m}_{w}$ is cooling water mass flow rate, c_{pg} and c_{w} are the gas and the water specific heats, T_{g}^{i} is the temperature of the gas at the inlet and, finally, ΔT_{w} is the temperature difference of the cooling water in inlet and outlet of the cooling system.
Main parameters of the tests are typically:

1) mixture composition;
2) mass flow rate;
3) Arc voltage and current (e.g. electric power);
4) Water cooling mass flow rate;

5) Water temperature jump between inlet and outlet of the cooling system (and therefore power subtracted by the cooling system).

Figure 27 shows the SPES facility image and Figure 28 shows a zoom next to the arc heater. Figure 31 shows the high-enthalpy gas flow in the test chamber, and the stagnation pressure flow probe.

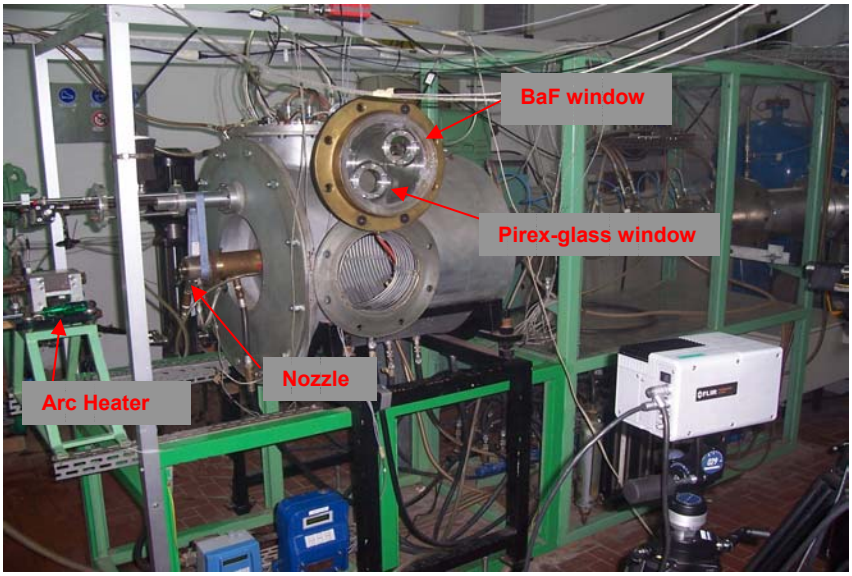

Figure 27 SPES experimental setup

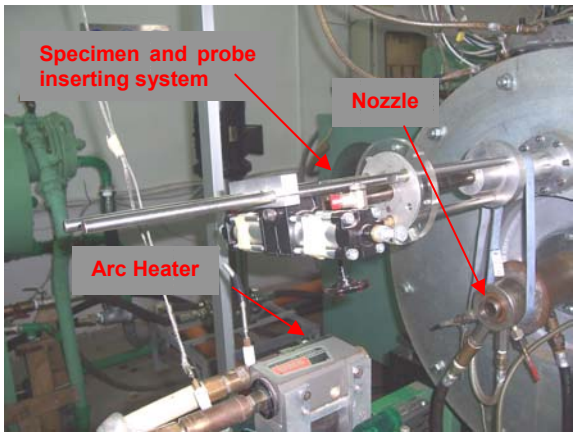

Figure 28 SPES, zoom on arc heater

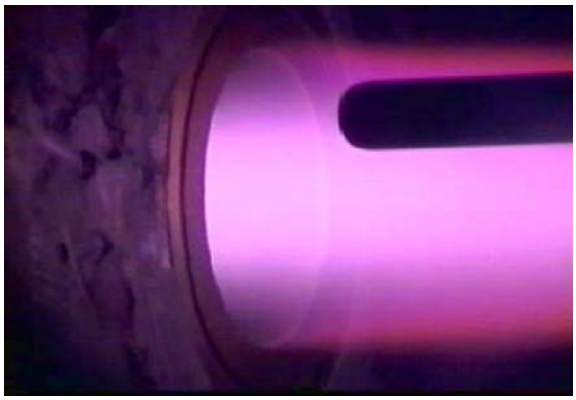

Figure 29 Pressure probe in the flux

The gas used for the experimental test is contained in high pressure tank (about 220 atm) and it flows between the blow-down arc electrodes, in which a pressure value less than 1 bar is reached. The mass flow rate, after the torch exit, expands through a convergent-divergent nozzle ($A_u / A^* = 20.66, M_u \approx 4.8$) and it arrived in a cylindrical test chamber with 7 cm diameter infrared and optical windows. The infrared window is realized in Barium Fluoride (BaF), that is transparent in the infrared wavelength, while the optical window is realized in pirex-glass. The plasma flow impacts the model that is injected into the stream by an automated arm, fixed on the test chamber lift. Finally, The plasma flow that exits the test chamber is collected into a diffuser that reduces the flow velocity to subsonic values.
The primary units of facility are: arc heater, conical nozzle, test chamber, model support system, diffuser, plasma heat exchanger and control/data acquisition. The auxiliary units of the facility are: power supply, vacuum supply, cooling fluids, compressed air, Argon supply.
In the following section, we examine the basic SPES facility components in details.

Arc Heater

The SPES facility is equipped with Prkin-Elmer METCO 9MB-M arc-heater, that can operate only with inert gas (argon, nitrogen), because to avoid corrosion problems to the electrodes; since, it can get a maximum power of 80KW.
Figure 30 shows a scheme of the arc-heater.

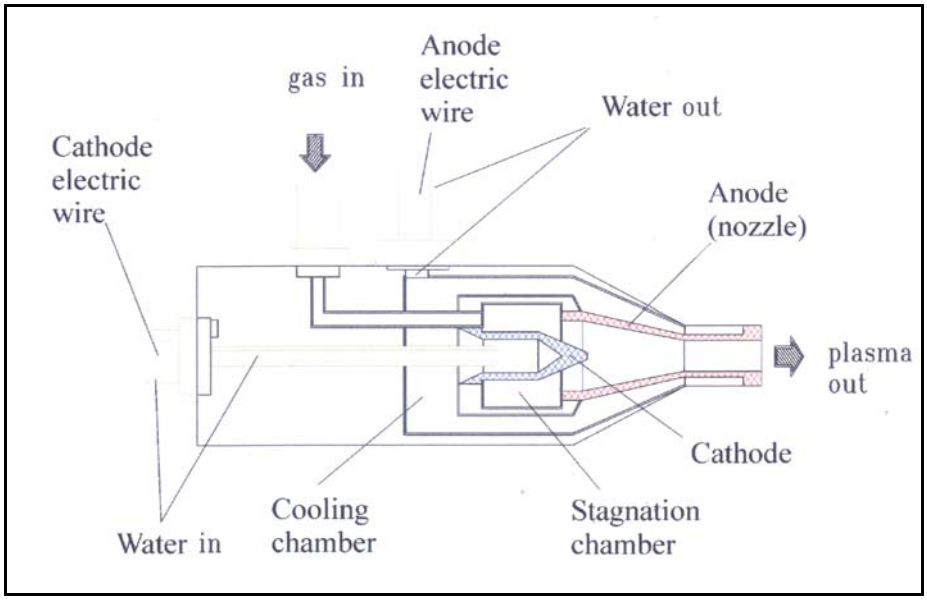

Figure 30 Arc heater scheme

Figure 31 Arc heater photo

The electrical arc, stabilized inside the arc heater, transforms the electrical energy into thermal energy and increases the temperature of the process gas. The electrical energy to the electrodes is supplied by a power supply system, where alternate current, supplied by facility boundary limits, is converted to direct current.
The process air into the arc heater is at an average pressure of 0.1÷0.2 bar and is heated to 2000-10000 K.
Demineralized water is used cooling arc heater facility. To know cooling water ΔT between inlet and outlet of the cooling system, k-type thermocouple is used. It's important because the power subtracted by the cooling system is proportioned to measured ΔT.

Mass Flow Controller

Working gas at a mass flow rate in the range of 10^{-3}-10^{-1} Kg/s at high pressure, coming from a compressed air plant, is supplied to the arc heater, with an argon mass flow of 0.01 Kg/s important to facilitate the ignition of the electrical arc and to reduce the electrode oxidation. The distribution system has two separate circuits. The primary circuit brings the inert gas (argon nitrogen) to the arc-heater, while the secondary one can distribute a requested amount of another gas (nitrogen, oxygen, carbon dioxide) to obtain a mixture in the mixing chamber, placed after the arc-heater and before the nozzle.

Supersonic Nozzle

The working gas from the arc heater expands through a conical nozzle (see Figure 32) up to the thermo-fluid-dynamic conditions required by the test. The nozzle has an area ratio $A_u / A^* = 20.66$, that allows a nominal Mach number of 4.8.

The supersonic, high-enthalpy nozzle flow of arc-heated facilities is in thermal and chemical nonequilibrium. Therefore, the application of sophisticated measurement techniques and numerical codes to such facilities is essential for a better understanding of the flow.

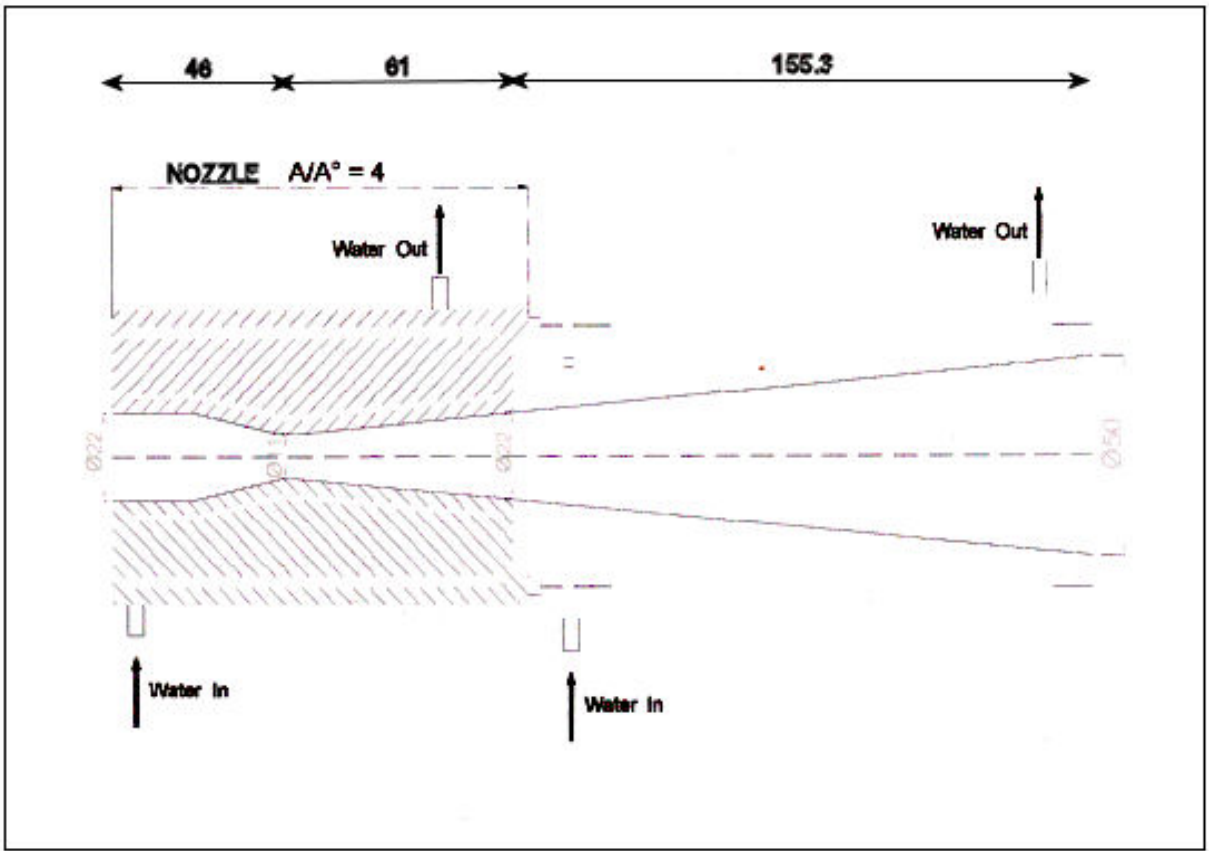

Figure 32 Conical nozzle scheme

As already described for the arc-heater, the nozzle wall are cooling with demineralized water. The nozzle's inner wall is made of copper and a relative catalicity referring to the high-enthalpy gas flow must be took into account.

The pressure in the nozzle is measured by a pressure probe insert in the nozzle wall at 2 mm from the exit section.

The vacuum system

The vacuum system generates and maintains the appropriate vacuum conditions in the test chamber required by each test. Typical vacuum values in the test chamber are between 0.1 e 1 torr. The vacuum system is a three stages system composed by mechanical pumps and two boosters allowing a pressure below 100 Pa, which is necessary for the ignition of the arc heaters.

Cooling system

There are two cooling circuits. The primary circuit works with demineralised water and it cools the arc heater facility, the supersonic nozzle and the heat exchanger.
The secondary one works instead with raw water and it cools the test chamber, the vacuum pumps and the demineralised water of the primary cooling system.

The control and acquisition system

The facility control and data acquiring system stands for the sequent:

- Automatic on/off
- To monitor arc tension and current, the cooling water temperature, the working gas mass flow rate, the pressure
- The arc current and gases mass flow rates variation, according to predefined laws

7.2 Instrumentation: the Infrared Camera

The Infrared Camera is a tool able to sense the infrared radiation and to associate a certain quantity of thermal energy to it and consequently a temperature (see Figure 33).

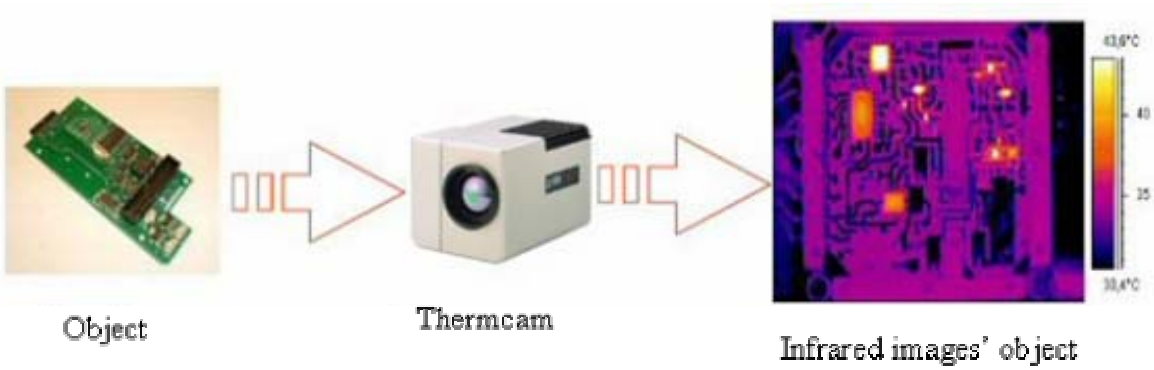

Figure 33 infrared image's object from thermcam

It suddenly shows on its display or on a monitor connected to it, underlining them with different colours, the different infrared radiation emissions, giving the so called *thermal map* of an object.
Viewing this image, set up the scale right, that is the range of temperature in which we think to effect the measure, we may understand which zones are "hot" and which "cold" in correspondence of the hottest colours (white, red, orange, yellow) and of the coldest ones (green, blue, violet, black).

Temperature measures: the emissivity's role

In the infrared camera software the right emissivity must be set up, in order to obtain the right correspondence between colours, represented in the infrared image, and temperatures, represented on screen by the instrument.
So the instrument "knows what it's looking" and after sensing the target's radiance point to point, it gives the target's temperature map, using the Planck's law for grey bodies.
The reflected temperature can be entered to the infrared camera software, to improve the accuracy in reading temperature. The quantity of infrared radiation that invests the target and its reflectivity have been took into account to compute the temperature. The right setting of the emissivity value is fundamental, when the aim is to compute the temperature of the tested object with the maximum accuracy. So, we have the following possibilities:

- to use manuals: in literature, there are tables in which there is an emissivity value for each material and surface type.
- if possible, to shade the surface with an opaque black varnish spray, whose emissivity is equal to 0.95÷0.96, or if not, to paste scotch on the surface of the target, getting the same result.
- to take a *contact thermometer* (for example a thermocouple), to measure the object temperature and then to vary the material emissivity value entered to the infrared camera software, until the temperature read in the probe is the same given by the thermometer; it's better then this, if allowed by the infrared camera software, to set up the temperature measured by the thermometer on the infrared image of the object, and directly obtain the emissivity value of the tested surface; the method just described works well to measure the emissivity.

Disturbs caused by reflection

To avoid to make errors when treating materials with reflecting surfaces in the infrared spectrum, it's necessary to apply particular solutions.
In fact, on this kind of surfaces, we can note points at higher temperature, which really are nothing else but reflections of the environment.
To resolve this problem, there are the following possibility:

- to use some opaque black spray varnish.
- to cover the objects creating reflection, using any simple cardboard panels.
- to take measurements not perpendicularly to the object, but with angles able to avoid reflections.

FLIR Thermacam SC-3000. Technical specifications

Figure 34 FLIR Thermacam SC 3000

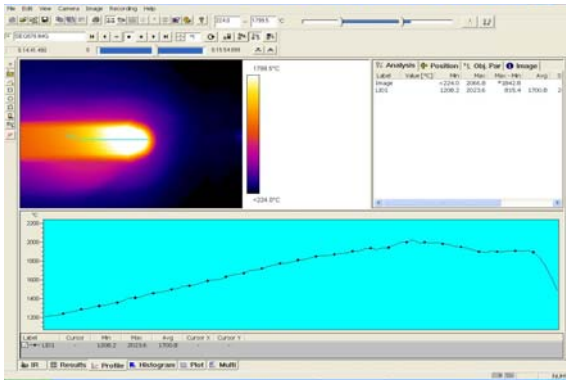

Figure 35 Thermcam SC 3000 GUI

IMAGING PERFORMANCE	
Field of view/min focus distance	**20°x15° / 0,3 m**
Spatial resolution (IFOV)	**1.1 mrad**
Thermal sensitivity	**20 mK at 30°C**
Image frequency	**50/60 Hz non-interlaced**
Electronic zoom function	**4X continuous**
DETECTOR	
Type	**GaAs, Quantum Well Infrared Photodetector (QWIP), 320x240 pixels**
Spectral range	**8 to 9µm**
Detector Cooling	**Stirling cooled to 70K, cool down time <6 minutes**
IMAGE PRESENTATION	
Video output	**RS170 EIA/NTSC or CCIR/PAL composite, S-video, and 14-bit digital serial link**
MEASUREMENT	
Temperature range	**-20°C to +1500°C, 4 ranges**
Accuracy	**±1% or ±1°C (for measurement ranges up to +150°C)**
	±2% or ±2°C (for measurement ranges above +150°C)
Atmospheric transmission correction	**Automatic, based on inputs for distance, atmospheric temperature and relative humidity**
Optics transmission correction	**Automatic, based on signals from 5 internal sensors**
Automatic emissivity correction	**Variable from 0.1 to 1.0 or select from listings in pre-defined materials list**
IMAGE STORAGE	
Type	**High capacity PC-Card, ATA compatible (160MB min)**

File formats	**14-bit radiometric IR digital image (IMG), includes header file with all radiometric data**
	8-bit standard bitmap (BMP), image only or image with screen graphics
	Every image stored in both formats
LENSES (OPTIONAL)	
Field of view/min focus distance	**2.5° - Telescope (2.5° x 1.88° / 45 m)**
	5° - Telescope (5.0° x 3.75° / 10 m)
	10° - Telescope (10.0° x 7.5° / 2 m)
	106 µm Close-up lens (34 mm x 25 mm / 110 mm)
	31 µm Microscope lens (10 mm x 7.5 mm / 26 mm)
Lens identification	**Automatic**
POWER INPUT	
Voltage	**12V DC, nominal**
Power Consumption	**22 watts**
AC Adapter	**Included**
ENVIRONMENTAL SPECIFICATION	
Operating temperature range	**-15°C to +50°C (5°F to 122°F)**
Storage temperature range	**-40°C to +70°C (-40°F to 158°F)**
Humidity	**Operating and storage: 10% to 95%, non-condensing**
Encapsulation	**IP 54 IEC 529 (metal casing)**
Shock	**Operational: 25G, IEC 68-2-29**
Vibration	**Operational: 2G, IEC 68-2-6**
PHYSICAL CHARACTERISTICS	
Weight	**3,2 kg (7.0 lbs.)**
Size	**220 mm x 135 mm x 130 mm (8.7” x 5.3” x 5.1”)**
INTERFACE	
Remote control options	**Remote focus (standard), RS-232 (standard)**
	Remote control panel (optional)

Table 4 SC 3000 Technical data sheet

Infrared detector

The infrared detector is composed by 320 x 240 photodiodes gallium arsenide array. The most common type of infrared detector are listed in the following table 1.
The diodes are *infrared detector elements* which, when stroked from an infrared radiation, emit an electric signal whose intensity is proportional to incident radiation intensity.
Analyzing these electric signals, matching different intensities with different colours on the display, we have the thermal image which is the thermal map of the object.
As reported in the technical datasheet, the total field of view is about 0.33 rad, and each diode sees a little part of the field of view of about 1.1 mrad.

The infrared camera software

The heating of the Infrared Camera itself, during its functioning, can be a remarkable “ground noise” for the diodes, so the measure of the temperature can fail.

To avoid this matter, a diodes cooling system is necessary (figure 4.15(b)), it can be a forced ventilation type (such as the FLIR Therma*CAM*™ SC3000) or a cryogenic liquids (such as liquid nitrogen) circulation type.
Figure 34 shows a typical window of the infrared Camera software interface, which it can do the sequent things:

- It allows to set up all the parameters related to the target and to the environment, such as the surface emissivity, the temperature and the relative humidity of the atmosphere, the distance from the target, as well as it allows to set up the parameters related to the best viewing of the thermal image, as the scale, the colours type, the temperature range to visualize (automatic or manual).
- It gives as output data, the thermal image (with the related scale), the temperature of one or more spots, which can be put in every point of the image, the temperature profile along a line, placed optionally on the image and it displays (if requested) the time sequence of images with temperature varying with time, in the point where the spot has been placed.
- It allows, as said, to compute the tested surface emissivity, if in the spot placed in a point of the image, the known (obviously in a different manner) temperature in the point itself is set to the spot.

Finally, we can say that the Infrared Camera, as thermal instrument, has the typical thermographic advantages but in contrast with other instruments, it has two features (the former is good, the latter is bad):

- it gives a thermal map of wide target, not a punctual measure, so that it allows to compute thermal gradients also.
- it needs the tested surface emissivity, without which, a quantitative measure of temperature is impossible.

Type	**Spectral range (μm)**
Gallium arsenide (GaAs) photodiodes	**8-9**
Indium gallium arsenide (InGaAs) photodiodes	**0.7-2.6**
Germanium photodiodes	**0.8-1.7**
Lead sulfide (PbS) photoconductive detectors	**1-3.2**
Lead selenide (PbSe) photoconductive detectors	**1.5-5.2**
Indium arsenide (InAs) photovoltaic detectors	**1-3.8**
Platinum silicide (PtSi) photovoltaic detectors	**1-5**
Indium antimonide (InSb) photoconductive detectors	**1-6.7**
Indium antimonide (InSb) photodiode detectors	**1-5.5**
Mercury cadmium telluride (MCT, HgCdTe) photoconductive detectors	**2-25**

Table 5 Infrared detectors

7.3 Instrumentation: the Pyrometer

The pyrometer is a radiometer, it receives a quantity of infrared radiation from the object which the temperature should be determine.
A single diode converts the radiant energy in an electric signal of intensity proportional to incidental radiation intensity on it. Connecting the pyrometer to a computer by serial gate, it is possible to read the time history temperature on the observed object at fixed wavelength and emissivity. The relationship to the base of the principle of operation of the pyrometer is the Planck's law for non-black body:

$$I_{\lambda,T} = \frac{\varepsilon_{\lambda,T} C_1}{\lambda^5 \left[\exp\left(\frac{C_2}{\lambda T} \right) - 1 \right]} \tag{6}$$

where:

$I_{\lambda,T}$ is the spectral radiance of a radiant surface;
C_1 is the first constant of radiation ($1{,}1911 \times 10^8 W \cdot \mu m^4 \cdot m^{-2}$);
C_2 is the constant second of radiation ($1{,}4388 \times 10^4 \mu m \cdot K$);
λ is the wavelength (μm);
T is the absolute temperature (k);
$\varepsilon_{\lambda,T}$ is the spectral emissivity of the radiant surface and is dimensionless.

By a pyrometer, it's possible to determine the emissivity of the considered material specimen through the Planck equation by knowing the temperature in the same point. The problem, then, has been moving on the determination of the temperature of the considered point.
The pyrometer Impac ISQ5 (see fig. 2) may be used whether in single-colour mode at λ=0.92 μm and dual-colour mode (λ_1 = 0.92 μm for the 1° channel and λ_2 = 1.06 μm for the 2° channel).

Dual-colour mode pyrometer

By dual-colour mode pyrometer, the radiance of an object can be measured in two different wavelengths. In this case, it is possible to measure the body's temperature in the following manner.
Hypothesis: the emissivities' ratio k, measured at two different wavelengths, is known.
Planck's law for non black bodies at two different wavelengths and for two measured radiance values is as follow:

$$\frac{I_1}{I_2} = k \frac{\lambda_2^5 \left(\exp\left(\frac{C_2}{\lambda_2 T} \right) - 1 \right)}{\lambda_1^5 \left(\exp\left(\frac{C_2}{\lambda_1 T} \right) - 1 \right)} \tag{7}$$

where $k = \frac{\varepsilon_1}{\varepsilon_2}$**, and with**

ε_1 emissivity of the surface at the wavelength λ_1 and at temperature T.

ε_2 emissivity of the surface at the wavelength λ_2 and at temperature T.

The operative wavelengths for this pyrometer are very close, since material's emissivity values at two wavelengths are very similar, therefore, the emissivity ratio, k, at two different wavelengths can be set up to unity, i.e. k=1. In this case, the measured temperature is independent by the emissivity value. Therefore, by means of this two measures it is possible to determine the temperature if the k ratio among the emissivities of the material at the two different wavelengths is known.

The dual-colour mode pyrometers are used to make difficult measures, e.g. elevated temperatures, atmosphere interferences, as smokes, particles in suspension, or media interposition between the object and the instrumentation. Other cases are unknown emissivity values or low varying with the wavelength. The disadvantage is that the spot pyrometer is order of millimetre, therefore it is not possible obtaining a thermal map of the object. The pyrometers with silicon, germanium or In GaAs detectors have shines filters for the sunlight or artificial light, because the latter hasn't any effect on the measure (the wavelengths range of interest is extreme proximity with the visible part of the wavelength spectrum).

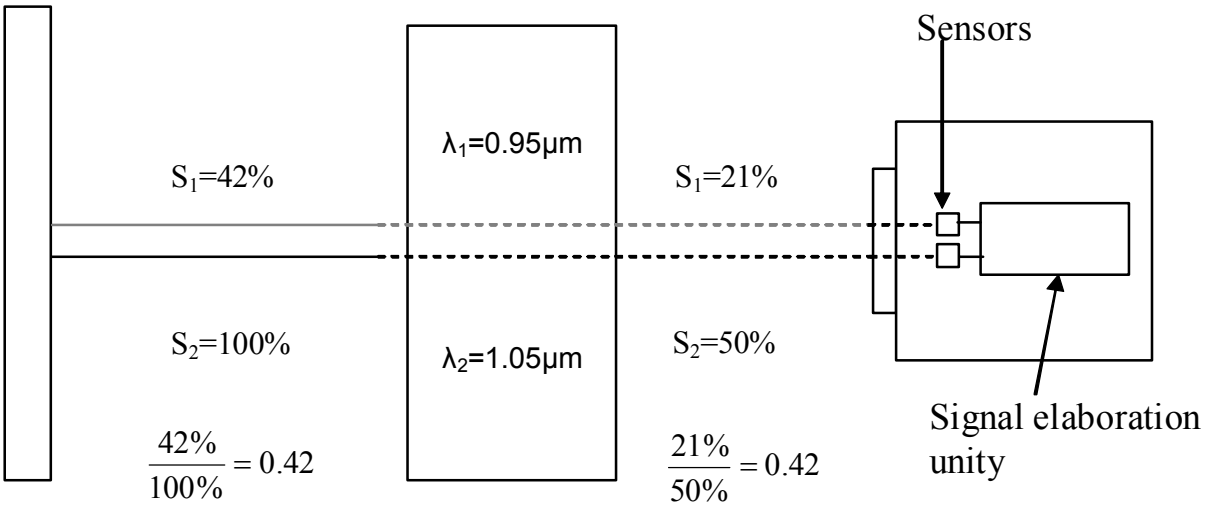

Figure 36 Two wavelengths mode pyrometer

Figure 37 The MIKRON IMPAC ISQ5 pyrometer

The MIKRON IMPAC ISQ5 pyrometer: technical datasheet

The infrared pyrometer utilize in experimental tests is MIKRON IMPAC ISQ5 (see Figure 37). It is a digital noncontact temperature measuring instrument in medium and high ranges. It

contain a simple integrated control panel, a linear adjustable current output and a serial interface. Via interface it is possible to read out the measuring temperature as well as change device parameters (e.g., ratio connection). The technical data are resumed in the following table 1.
By the pyrometer software, it is possible setting the k and ε parameters and the change between the one colour mode and dual colour one, in real time, i.e. during the acquisition of the signal.

Temperature range	**1000…3000 °C**
Spectral ranges	**channel 1: 0.95 µm**
	channel 2: 1.05 µm;
Lens assembly	**Focusable, 250 mm…∞**
Measurement uncertainty (on black body source)	**<1500°C: 0.5% of measuring value / °C ± 2 K**
	>1500°C: 1.0% of measuring value / °C
Resolution	**< 1 °C**
Temperature coefficient	**±0.25 K per K change of device case temperature**
Repeatability	**0.2% of measuring value / °C ± 2 K**
Response time t_{90}	**<10 ms, adjustable up to 10 s**
Ration correction	**ε1/ε2: 0.800…1.250**
Switch off	**Below minimum intensity (2%..50%, adjustable via interface)**
Analog output	**Linear, switchable 0/4…20 mA, burden:0…500 Ω**
Power supply	**24 V DC ±25%, stabilized, ripple < 50 mV**
Power consumption	**< 3 VA (with laserpointer)**
Serial interface	**RS232 or RS485 adressable, half duplex, baud rate up to 38.4 kBd**
Peak memory	**Single or double storing peak memory clearing**
Insulation	**Supply, analog output and serial interface are galvanically separated**
Environmental rating	**IP65 (according to DIN 40 050)**
Safety system	**I (VDE 0411**
Operating ambient temperature	**0…70°C (housing temperature)**
Storage temperature range	**-20…70°C**
Weight	**ca. 550 g**
EMC	**CE label, in accordance with UE rules about electromagnetic**

Table 6 The MIKRON IMPAC ISQ5 pyrometer: technical datasheet

8 On-Ground Experimentation

The selected configuration of the test-bed is shown in Figure 38 and Figure 39. The hemispherical specimen is supported by a ceramic cylinder (Allumina) and by an Inconel holder able to withstand high temperature (in the order of 1000°C) for a sufficient long time. Figure 40, Figure 41 and Figure 42 show the metallic support, the insulator and the UHTC specimen, respectively.

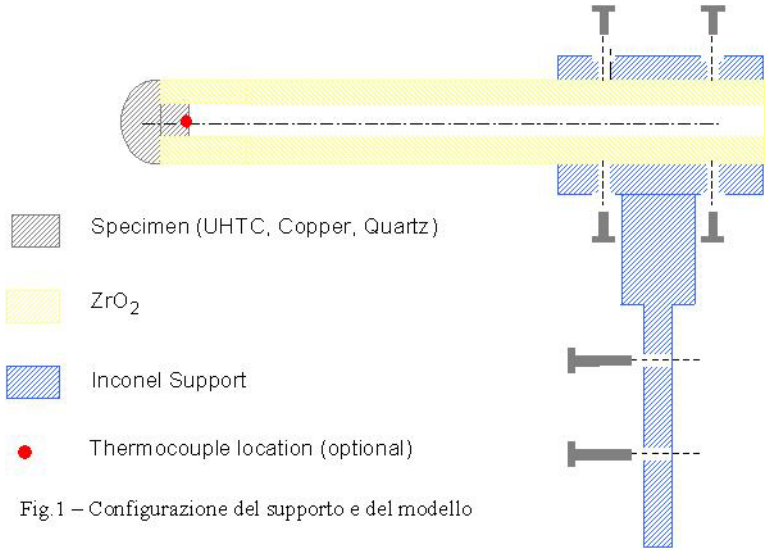

Figure 38 Configuration of the test bed

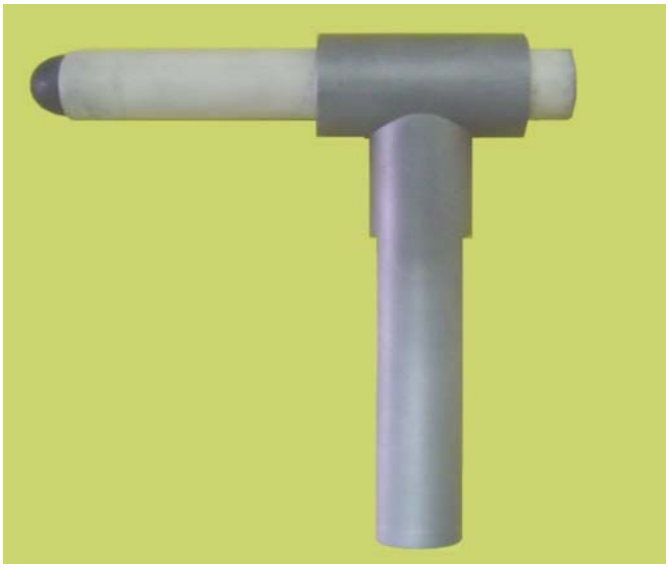

Figure 39 picture of the specimen, insulator and holder

Figure 40 Inconel support

Figure 41 Allumina insulator

Figure 42 UHTC specimen

The length of the Inconel support (see Figure 40) is 40 mm, the external and internal diameters are 25 mm and 19 mm, respectively. The overall length of the metallic holder is 125 mm.
The cylindrical insulator, shown in Figure 41, is made of Allumina and has a length of 100 mm; its external diameter is 17.5 mm, while the internal diameter is 12mm.
The curvature radius of the hemispherical specimen (see Figure 42) is 7.5 mm. The back cylinder has a length of 5 mm and radius of 4 mm. A small ring of graphite (thickness of 2mm) has been introduced between the specimen and the insulator.
Pictures of the complete experimental setup are shown in the paragraphs dedicated to the every experimental test.

8.1 Wind tunnel facility test

Because of the high costs of flight experiments and the shortcomings of numerical tools with respect to design verification and qualification of hot structures of re-entry vehicles, long-duration, high-enthalpy, ground-test facilities are still the key tools for such applications. During

re-entry, the gas around a space vehicle is heated to a very high temperature level, typically several thousand Kelvin. At these high temperatures, the simulation of re-entry aerodynamics requires not only the duplication of Mach and Reynolds numbers to account for compressibility and viscous effects, but also for matching real-gas similarity parameters.
In the hypothesis that the wind tunnel is capable to supply an air stream at the very same values of free flight, i.e. $(H_\infty)_t = H_\infty$ and $(p_{02})_t = p_{02}$, the Zoby engineering formula (see ref. 31) would then predict : $(\dot{q}_0)_t = \dot{q}_0$. Indeed, this is not the true, because a part of the energy is stored in the dissociation energy in the tunnel air stream. Infact, let us consider a high enthalpy flow across a nozzle. Upstream of the nozzle the total enthalpy, composed by the sensible enthalpy (c_pT) and the chemical enthalpy $\sum_i c_i (\Delta h)_i^f$.
When trying to simulate free-flight aerothermodynamic conditions in wind tunnel, since a complete duplication of all the relevant flight conditions cannot be achieved (e.g. model scale, p_∞, V_∞, chemical conditions), one must select and choose a finite number of parameters leading to the simulation of the aerodynamic heating. In the present context, the convective heat flux distributions over the body surface should like to reproduce, with particular reference to the stagnation point conditions. Let us give the guidelines necessary to identify the most appropriate wind tunnel settings simulating free-flight conditions. In a first approximation, engineering formulas can be used for the stagnation point heat flux, as Zoby's formula (see ref. 31), in international units (MKS):

$$\dot{q}_0 = 3.55 \times 10^{-4} \sqrt{\frac{p_{02}}{R}} \left(H_\infty - h_w \right) \tag{1}$$

where R is leading edge radius of curvature, H_∞ is the air stream total enthalpy (per unit of mass), p_{02} and hw are stagnation point pressure and wall enthalpy, respectively. This equation provides the value of the stagnation point heat flux for total enthalpy flow up to 10^6 J/kg and for a fully catalytic surface. Other formulas have been obtained following the original Fay-Riddell procedure (see ref. 13) by fitting a number of numerical computations and heat flux measurements in high enthalpy arc-jet wind tunnel.

8.2 Numerical analysis

The numerical analysis will be carried out to identify the size of the specimen to achieve heat fluxes and temperatures of interest.
The CFD computations was carried out solving the full Navier-Stokes equations for a turbulent multi-reacting gas mixture in chemical non equilibrium to evaluate the convective surface heat flux and pressure distribution on the specimen.
The commercial solver FLUENT code (2005) was used in this work, in combination with a number of "ad hoc" developed user defined functions, to model hypersonic flows in chemical and vibrational nonequilibrium and to investigate different conditions of the surface catalytic properties (non catalytic, fully catalytic, partially catalytic).
Numerical simulations were focused on the analysis of the following subjects:

- the effects of the surface catalicity of the materials;
- the distribution of the surface heat flux;
- the aerodynamic heating, caused by surface heat flux, in the standard operative conditions of the wind tunnel.

The numerical model used for a reacting flow in thermo-chemical non-equilibrium conditions has been validated by means of comparisons with numerical and experimental results available in literature (see ref. from 1 to 5). More specifically, the possibility to evaluate the surface

catalytic property by numerical-experimental correlation of the surface heat flux of specimens at the typical plasma torch conditions has been demonstrated in ref. 2.
The plasma torch facility was used heating the specimen up to temperatures in the order of 2000 °C, considering the its typical operative conditions. It is able to operate with inert gases (He, N_2, Ar) with a power up to 80 kW and mass flow rates up to 5 g/s.
The specific total enthalpy at the torch exit is evaluated by a balance between the energy supplied to the gas by the arc heater and the lost energy through the cooling system, using the following relation:

$$H = \frac{VI + c_{pg}\,\dot{m}_g\,T_g^i - c_w\,\dot{m}_w\,\Delta T_w}{\dot{m}} \qquad (2)$$

where

H is the average total specific enthalpy at the torch exit,
V is the voltage and I is the current at the arc heater,

$\dot{m}_g$ is the gas mass flow rate,

$\dot{m}_w$ is the mass flow rate of the cooling water,

c_{pg} and c_w are the gas and the water specific heats,

T_g^i is the temperature of the gas at the inlet,

ΔT_w is the temperature difference of the cooling water.

The simulations were carried out assuming steady conditions and local radiative equilibrium, i.e. neglecting the conduction in the solid. In order to achieve very high temperatures the torch was operated at atmospheric conditions, because the heat flux depends not only on the total specific enthalpy but also on the stagnation pressure (see ref. 31). Therefore, for a fixed total specific enthalpy a UHTC specimen achieves the maximum temperatures at higher pressure.
Due to the extremely high thermal loading on the materials during the re-entry phase, oxidation and other surface chemical reactions have to be taken into consideration leading to variations of emissivity and catalytic properties. All the simulations performed show that there is a different behaviour between the cases of non catalytic and fully catalytic wall.
The nitrogen flux of 1g/s, with a power transferred to the fluid by arc-heater facility of about 15 Kw, partially dissociated, interacts with the cold air at the exit torch. The present oxygen in the atmosphere starts to dissociate and to react with the nitrogen forming a mixture that it is modelling as mixture composed by five species: N_2, O_2, O, N, NO.

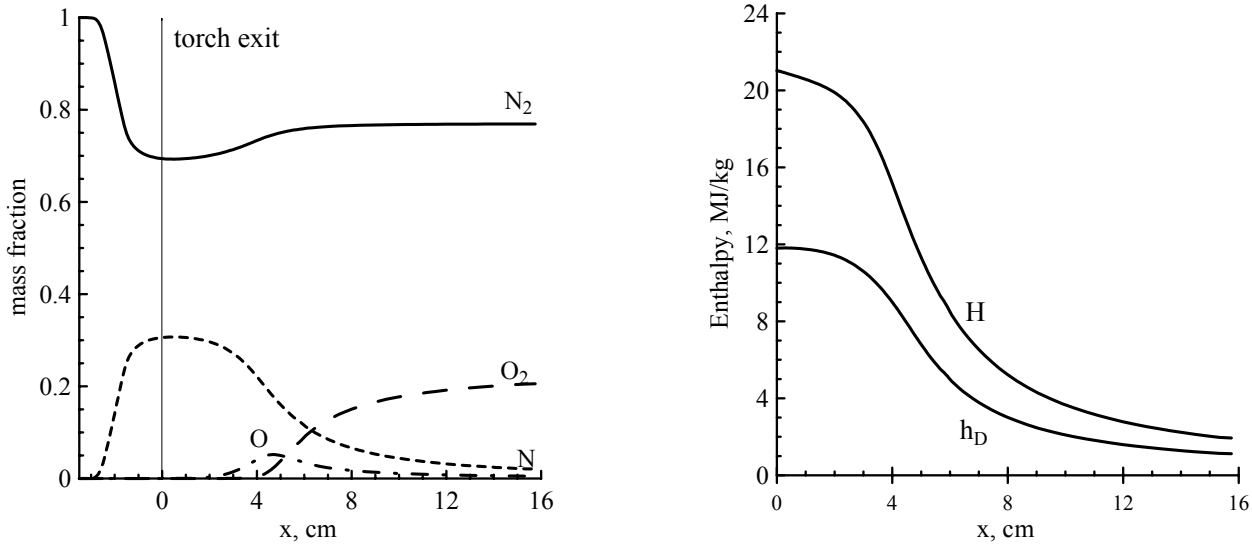

Figure 43 (a) Species' mass fractions and (b) specific total enthalpy (H) and chemical enthalpy (h_D) along the torch axis

The total specific enthalpy decreases rapidly long the axis torch (see Figure 43 (b)). This suggests varying the distance of the model in comparison with the exit torch to get different heating conditions. In particular, the range of interest is understood among 4 cm and 12 cm, with a consequent variation of total specific enthalpy among $1.52*10^7$ J/kg and $2.79*10^6$ J/kg, respectively.

The stagnation point heat flux by numerical simulations is near that semiempirical formulas one (ref. 6):

$$\dot{q}_{FC} = 2.75 \times 10^{-5} \sqrt{\frac{p_{02}}{R}} (H_0 - h_w)^{1.17} \qquad \dot{q}_{NC} = 2.75 \times 10^{-5} \sqrt{\frac{p_{02}}{R}} (H_0 - h_D - h_w)^{1.17}$$

where the NC and FC sub-symbols announce condition of non catalytic and catalytic wall, respectively, H_0 is the total average specific enthalpy to the exit torch, h_D is the chemical enthalpy and h_w is the wall enthalpy.

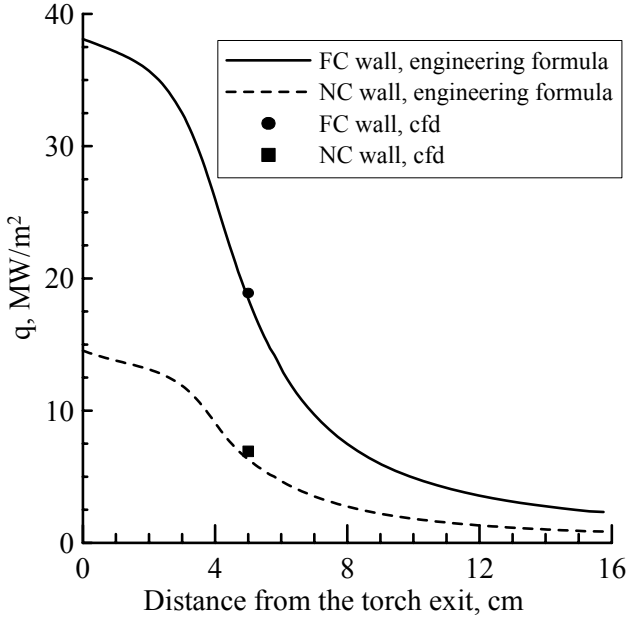

Figure 44 Stagnation point heat flux computed at different distances from the torch exit. The two lines correspond to the engineering formulas. The two points are evaluated with cfd-code.

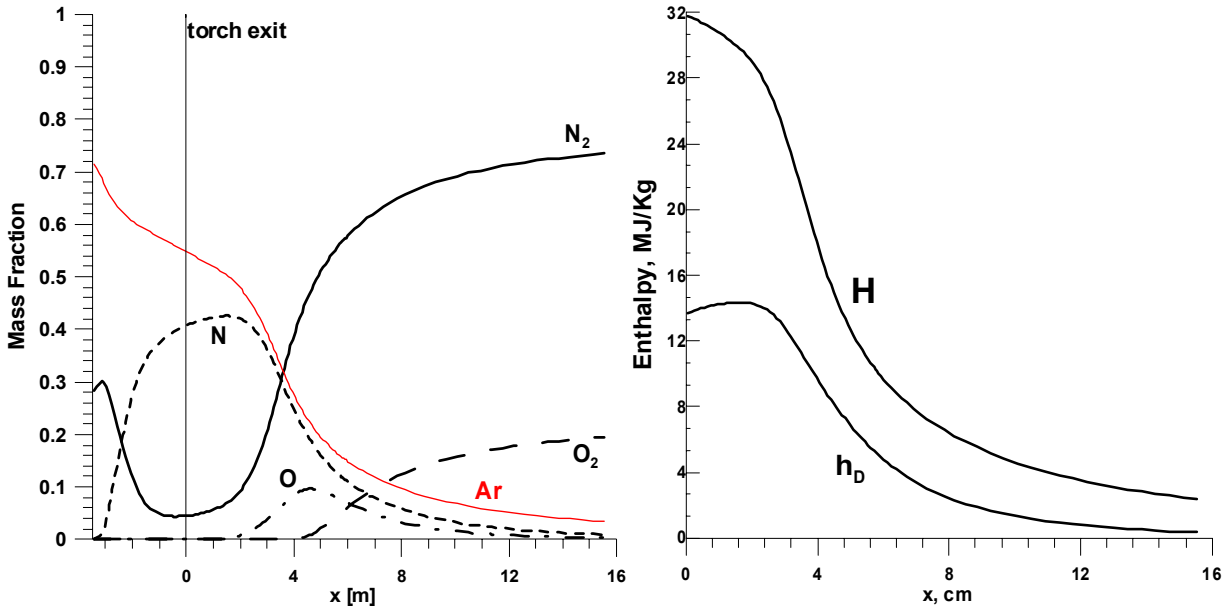

Figure 45 (a) Species' mass fractions and (b) specific total enthalpy (H) and chemical enthalpy (h_D) along the torch axis

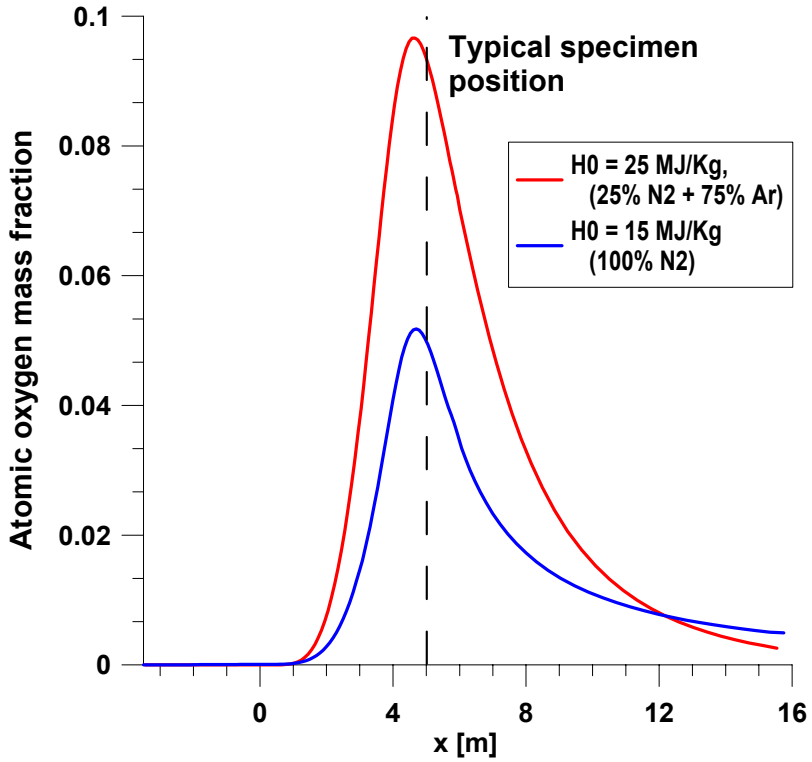

Figure 46 Atomic oxygen mass fraction along the torch axis

The thermal behaviour of the gas is heavily influenced by chemical reactions of the mixture constituents, which are primarily dissociated and recombination reactions. A comparison of characteristic reaction and low times provides information on the significance of the thermo-chemical state of the flow field. The characteristic parameter is the surface Damköhler number, which is defined as the ratio of the characteristic particle diffusion time to the characteristic time for a surface reaction. An experimental investigation of such problems can only be carried out in arc-heated wind tunnels, which are known to be restricted in the simulation of flight Reynolds numbers because of low stagnation pressure, but are very useful in studying local gas-surface interaction phenomena because of their long testing time.

The oxidation and erosion behaviour of TPS materials are strongly affected by the thermo-chemical state of the gas and the surface properties of the material. Therefore, a reliable qualification of the hot structure components in ground-test facilities also requires dedicated data on the flow regime.
Because of the severe flow conditions in high-enthalpy facilities, flow characterization is only possible as a combined effort of classical measurement techniques and numerical tools. All parameters that are not accessible to measurement are characterized by computation.
A good reproduction of the behaviour of the atomic species, especially oxygen, in the ground facility is important to ensure that oxidation of the TPS material is correctly simulated.
In Figure 43a and Figure 45a, the species' mass fractions along the torch axis are shown in the case of H_0=15 MJ/Kg and H_0=25 MJ/Kg at torch exit, respectively. In the Figure 46, there is a comparison between the species' mass fractions along the torch axis between the two cases. From these figures, we see that to higher H_0 value corresponds an higher oxygen dissociation degree, i.e. the surface material is invested by an higher atomic oxygen flux. In these conditions, the material's oxidation resistance could not be sufficient.

8.3 Plasma Torch Calibration

Experimental tests have been carried out with a plasma torch, using different Argon and Nitrogen mixtures as working fluids. Figure 47 shows the measured cooling water ΔT varying with power given to the plasma torch.
Primary calibration tests have been carried out to identify the test conditions in terms of total specific average enthalpy at the torch exit, obtained with equation (3) here reported for clarity. Figure 48 shows total specific average enthalpy varying with power given to the plasma torch.

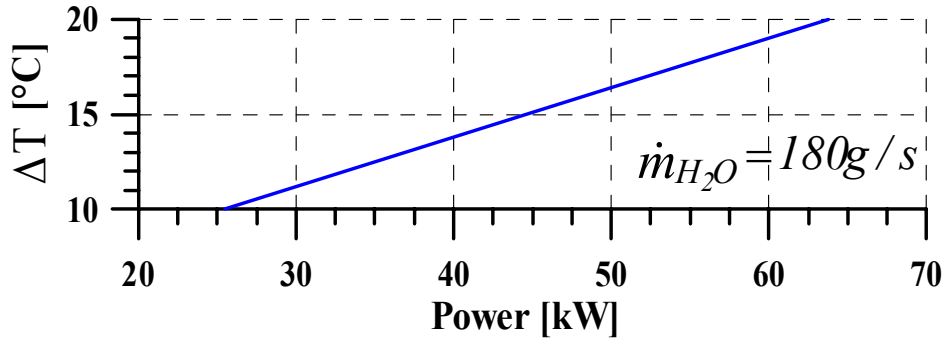

Figure 47 Measured cooling water ΔT varying with given power

$$H_0 = \frac{VI + c_{pg}\,\dot{m}_g\,T_g^{\,i} - c_{pw}\,\dot{m}_w\,\Delta T_w}{\dot{m}} \qquad (3)$$

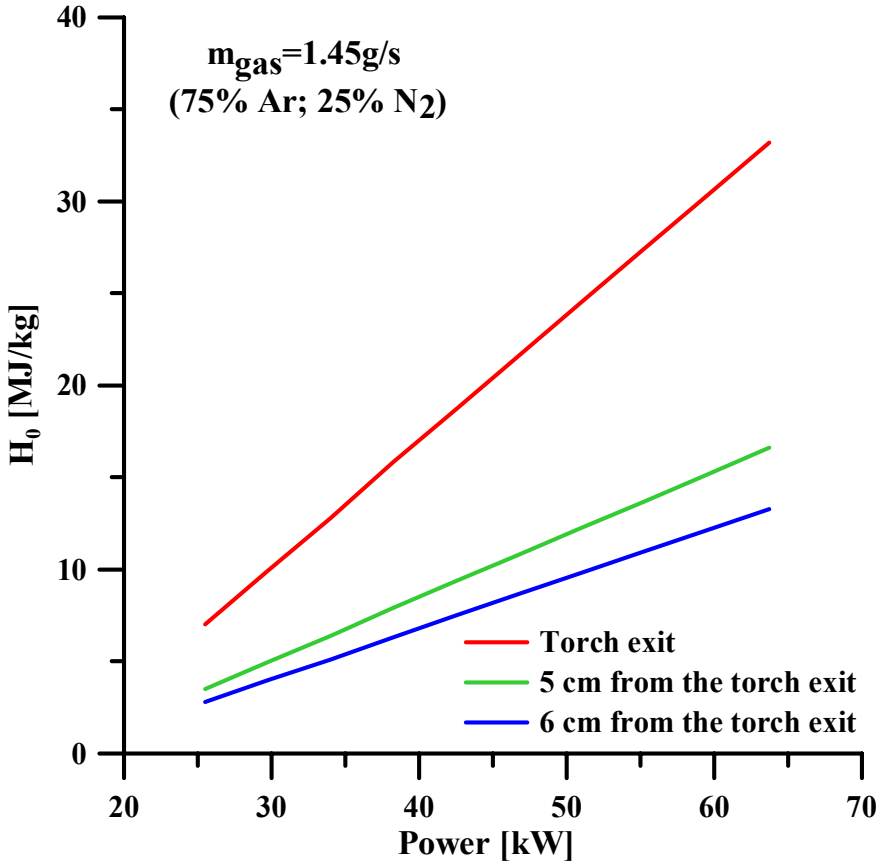

Figure 48 Total specific average enthalpy varying with given power

8.4 Experimental Tests for Setup Definition

Emissivity measures of a tungsten filament

To validate the method to estimate surface emissivity, before testing the interesting ZrB_2 models, a common halogenated light bulb's tungsten filament emissivity (well known in literature) was estimated. Temperature values reachable by the very hot string can be greater then 3000 °C.
Tungsten properties, mainly emissivity variation with the wavelength, are well known by literature data (see the diagram reported in Figure 49, [ORIEL Instruments]).

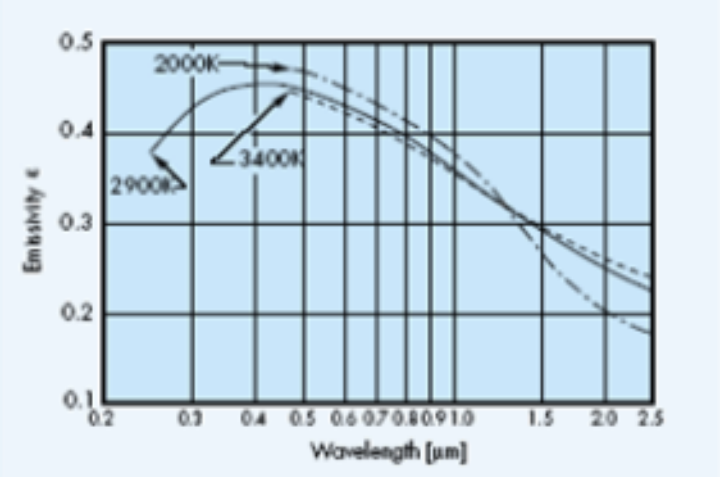

Figure 49 Tungsten emissivity varying with wavelenght

Using a voltage regulator, tungsten filament temperature was varied from 2000 K to 2600 K. The constant in the dual-colour pyrometer mode k =1 was then changed to 1.023. At each temperature range, the emissivity was evaluated switching between the two pyrometer modes.
At fixed wavelength $\lambda = 0.95$ μm, the emissivity value was varied to obtain same "apparent" temperature value in both pyrometer modalities, then the obtained emissivity value was compared with data reported in literature. Figure 50 shows the described procedure at temperature value of 2000 K. In the considered range, the measured emissivity value is very close to 0.4, according to data reported in literature (see Figure 49)

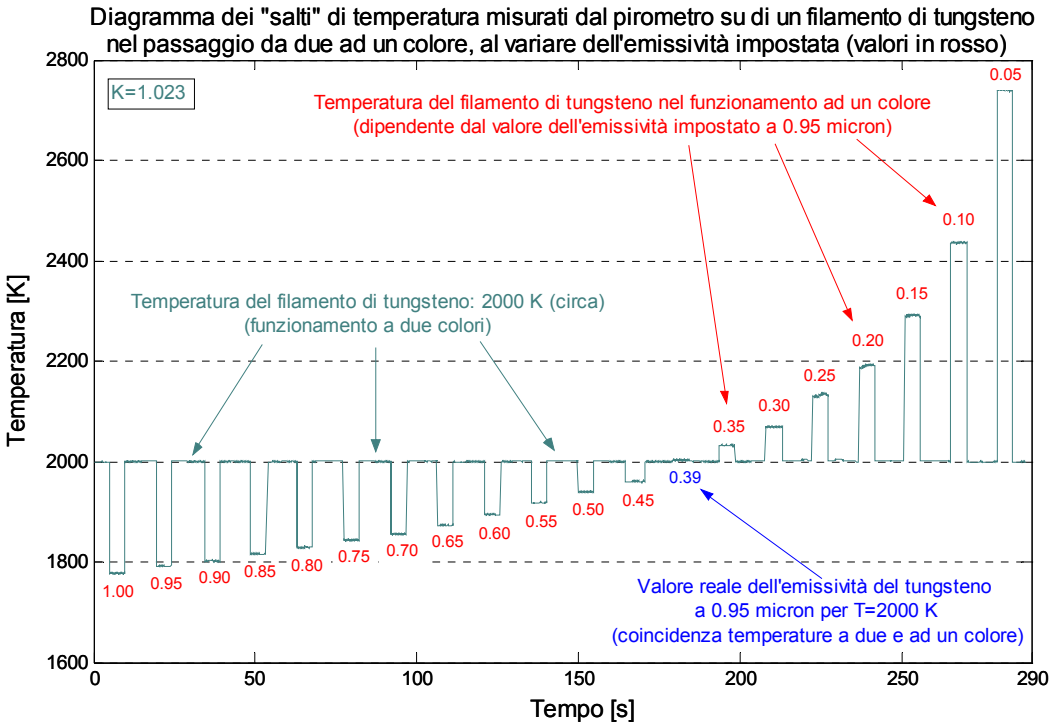

Figure 50 Experimental method to obtain tungsten emissivity

8.5 Experimental Test with ZrB_2 specimen with Nitrogen flux

The awareness of the wall emissivity is a challenging task for UHTC. Because of extremely high thermal loading of the material during the re-entry phase, chemical reactions at the surface have to be taken into account leading to variations of emissivity.

As a first test, a pure ZrB_2 specimen (sphere-cone, flat bottom configuration), with a 5 mm curvature radius, was exposed to high specific enthalpy nitrogen flow at an angle of attack of about 30° and a distance of about 5cm from the torch exit, in atmospheric pressure. This flow was generated by the plasma torch of the SPES facility at the conditions reported in table 1.

shows the infrared image of the specimen and the spot of about 3 mm considered for pyrometer measures. The experimental test time was about 2 minutes and 30 seconds long.

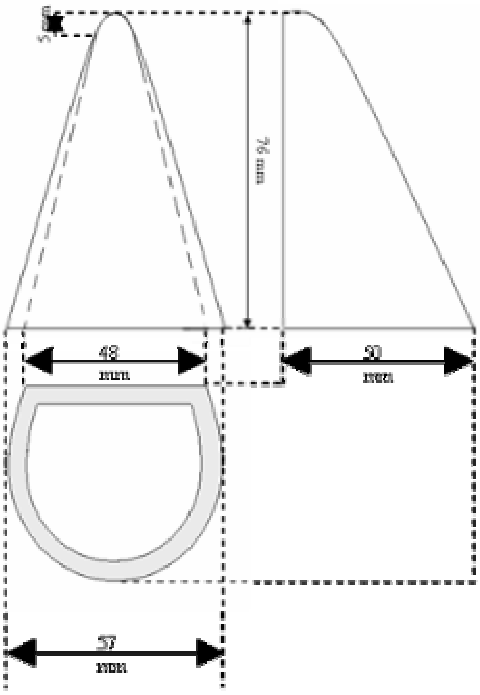

USV nose prototype scheme

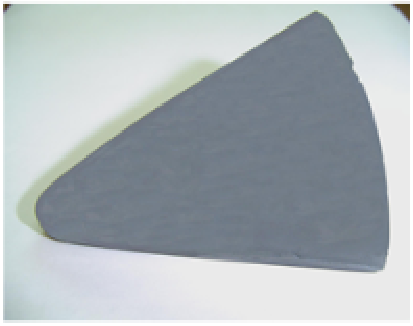

USV nose prototype photo

$\dot{m}_{H_2}$	1 [g/s]
P	21 [KW]
I	350 [A]
V	61 [V]
$\overline{H}_0$	14.1 [MJ/Kg]

Table 7 Plasma torch conditions

Figure 51 The specimen and the torch exit

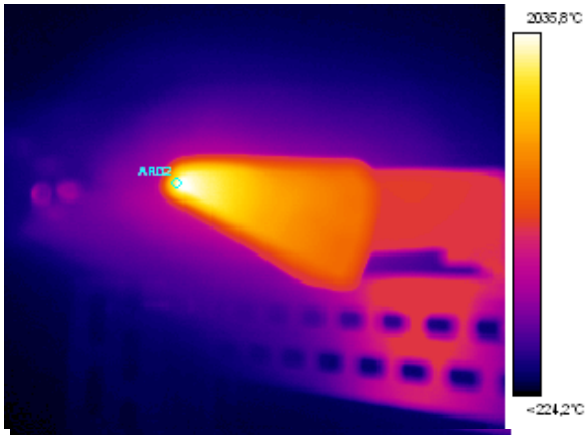

Figure 52 Thermocam image of the specimen and the spot considered for pyrometer measures

By post-processing data, as shown in Figure 53, an emissivity value between 0.7 e 0.72 was evaluated. At the end of the test a white sheet, maybe ZrO_2, was observed on the leading edge of the specimen (see Figure 55). This sheet was leaved and find new ZrB_2 layer not completely oxidized.

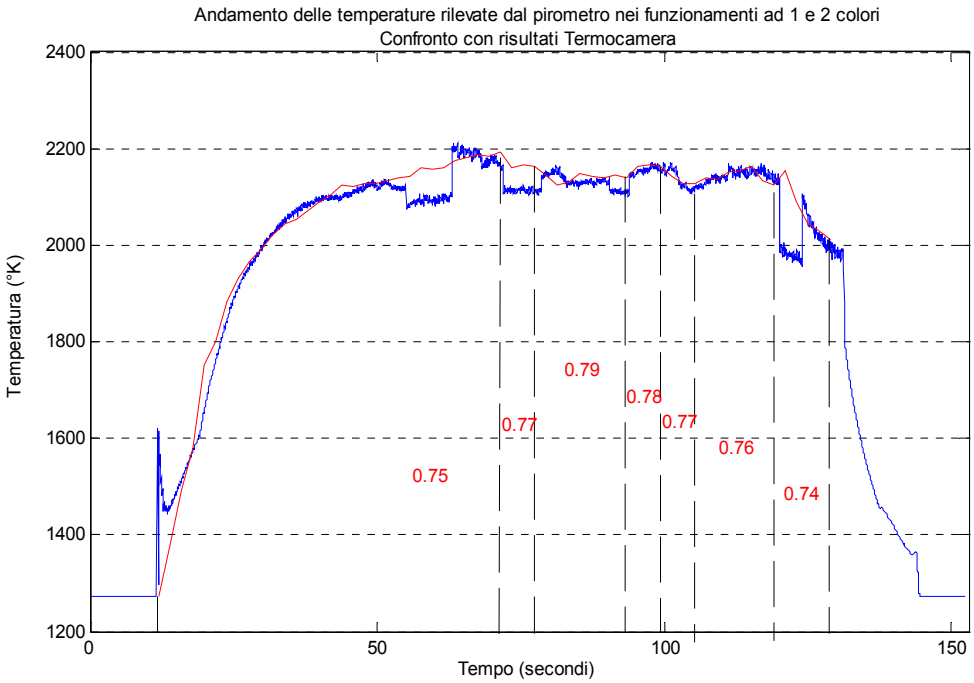

Figure 53 Temperature varying with time during experimental test on ZrB_2 specimen

Figure 54 shows a comparison between temperature values in a point at about 3 mm from the stagnation point for condition of fully catalytic wall, non catalytic wall and partially catalytic (considering some value of surface recombination parameter k_w).

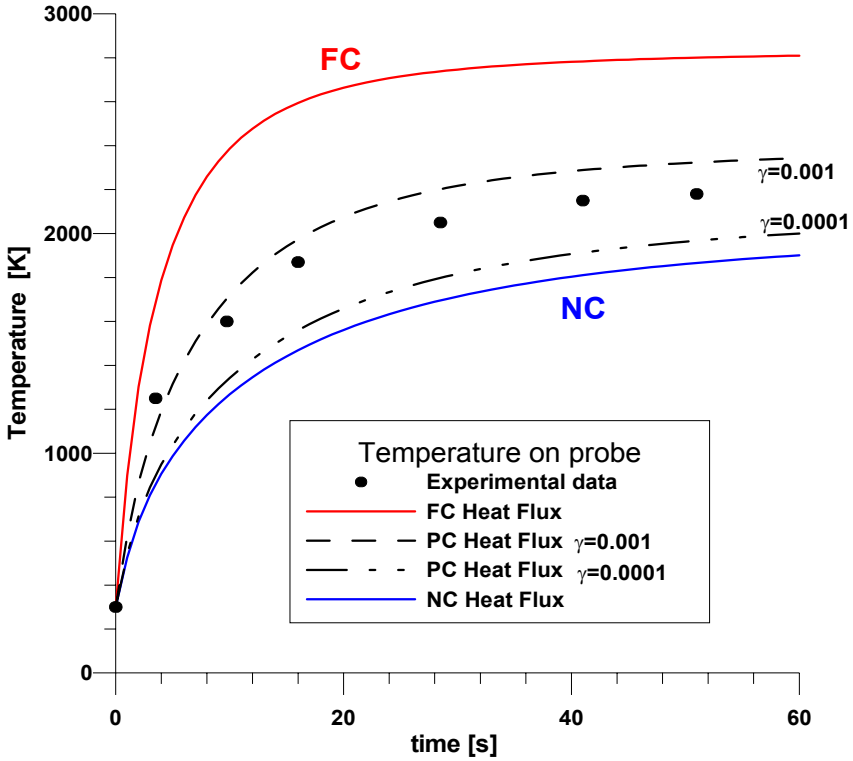

Figure 54 Temperature varying with time during experimental test on probe

Comparing the numerical and experimental results, it was found a partial cataliytic behaviour for ZrB2 specimen with a recombination coefficient value γ_{wi} between 10^{-3} and 10^{-4}, as shown in Figure 54.

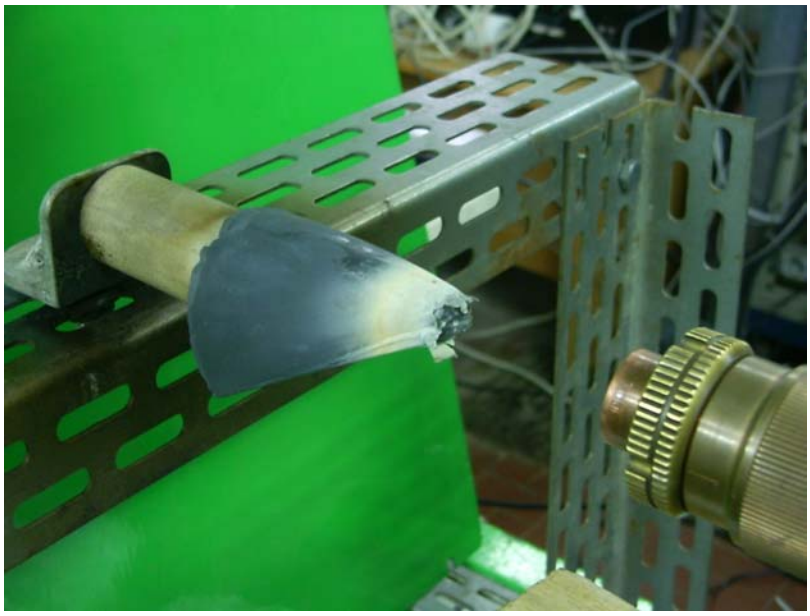

Figure 55 the leading edge of the specimen was damaged during the test

9 Plasma Wind Tunnel Test

9.1 Experimental setup

This chapter deals with an experimental test in the SPES facility (described in the previous chapter) at hypersonic conditions.
The specimen in UHTC (ZrB_2 + SiC) is fixed to allumina cylinder, that is fixed in the support in Inconel, as previously described in the chapter about on-ground experimentation. The specimen was inserted in the high-enthalpy flow by a mechanical arm, which operates at the outside of the gallery, in order to inserting the model in the flux. During the test the mass flow rate of Nitrogen (N_2) was 1g/s, the electrical power was 21 kW. The stagnation pressure was 25 torr, the nozzle exit pressure and pressure in the test-chamber was 1.7 torr and 0.9 torr, respectively. The specific total enthalpy values at the torch exit was about 18 MJ/Kg and at the nozzle exit was about 10 MJ/Kg, respectively. Before to insert the UHTC specimen in the flow, a pressure probe measures the total pressure. Once the specimen is exposed to hypersonic flow, the time history surface temperature is stored by infrared camera and pyrometer.
To characterize the flow an evaluation of specific total enthalpy at the exit nozzle is necessary. By means an energy balance between the energy supplied to the gas by arc heater and the lost energy through the cooling system it is possible to obtain an average value at the exit nozzle with the following formula:

$$H = \frac{VI + c_{pg1}\dot{m}_{g1}T^{i}_{g1} + c_{pg2}\dot{m}_{g2}T^{i}_{g2} - c_{pw}\dot{m}_{w}\Delta T_{w}}{\dot{m}} \tag{4}$$

where H is the average total specific enthalpy at the exit nozzle, VI is the supplied power to the gas by arc heater, $\dot{m}_{g1}$ and $\dot{m}_{g2}$ are mass flow rate in the primary and secondary inlet, respectively.

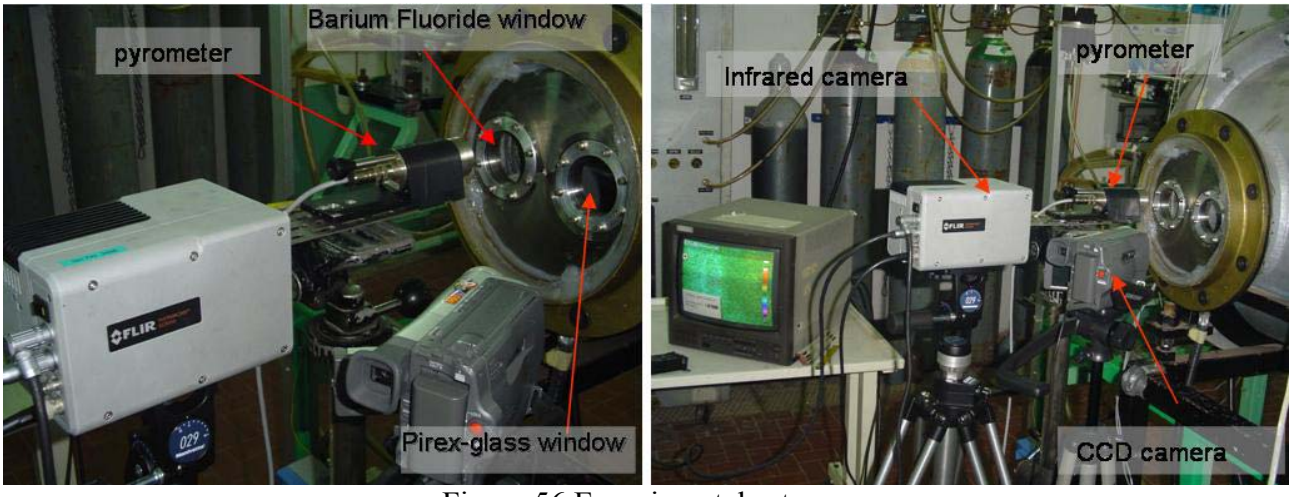

Figure 56 Experimental setup

The infrared analysis was performed by the Impac ISQ5 pyrometer and the FLIR SC-3000 infrared camera. The instrumentation, placed out of the tunnel facility, was seen the specimen during the experimental test through a barium fluoride window (at the end of paragraph, there is the description of effect of the barium fluoride window) in its operational wavelengths, i.e. λ=0.92 μm for the pyrometer and λ=9 μm for the infrared camera, respectively. Moreover, a

CCD camera was used to capture the time evolution of experimental test thorough a pirex-glass window.
Figure 56 shows the experimental set-up and Figure 57 shows the specimen in the facility test-chamber.

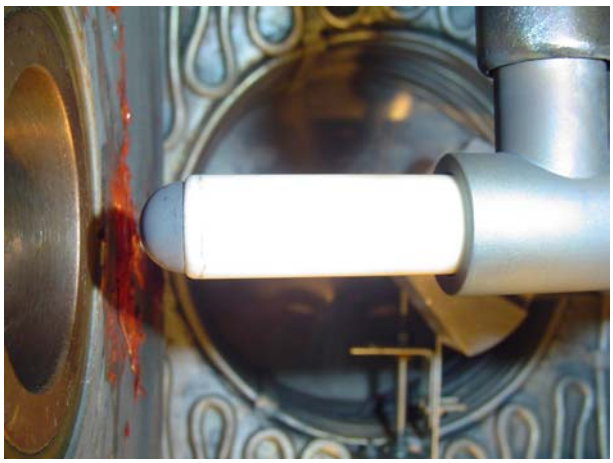

Figure 57 The specimen in the facility test-chamber

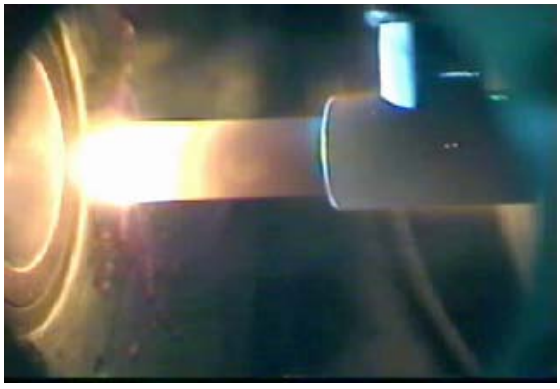

Figure 58 (a) and (b) The specimen during the experimental test.

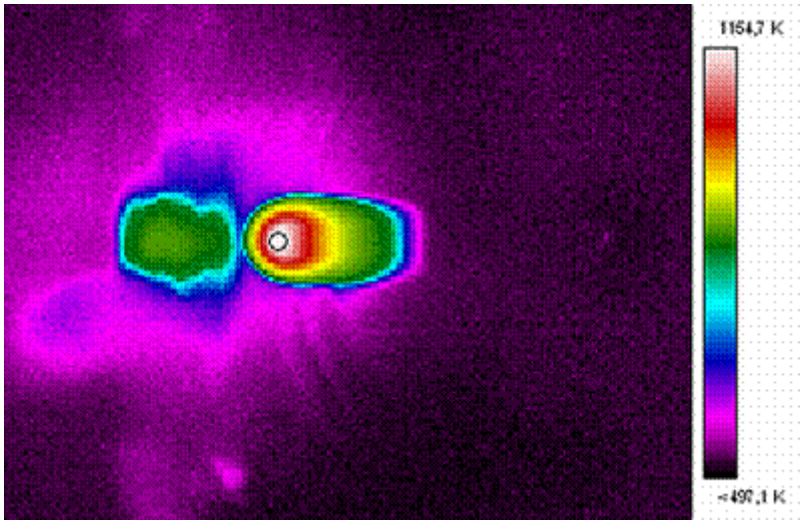

Figure 59 The specimen infrared image during the test

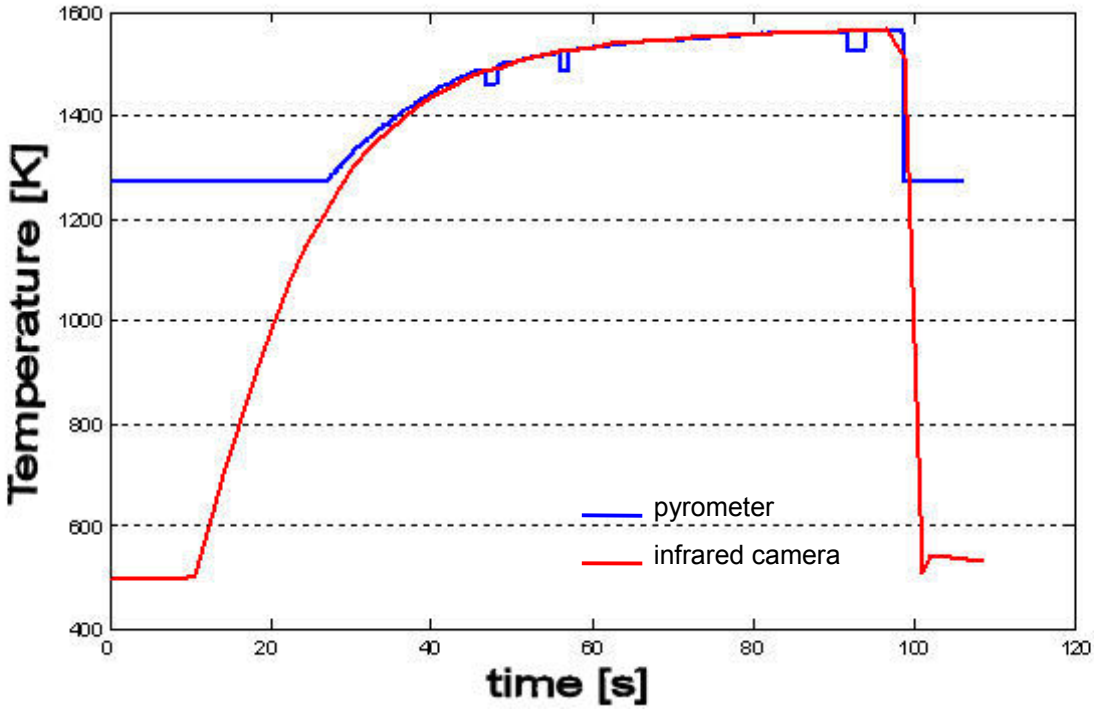

Figure 60 Time history surface temperatures measured by the pyrometer and the infrared camera

9.2 Experimental test with N2 flow

The experimental test time was about 1 minute and 30 seconds long and the final temperature was about 1600 °K. The pyrometer function has been changed three times to the single wavelength mode, in order to measure the surface emissivity at the wavelength of 0.92 μm. The estimated value of the emissivity was about 0.79.

Figure 10 shows that, for an emissivity of 0.77, the value of the temperature measured with the infrared camera at λ = 9 μm is almost coincident with that obtained by the pyrometer. This confirms that the surface emissivity does not change very much with the wavelength.

Figure 59 shows a specimen infrared image during the test. In this image, a spot of about 3 mm is represented. This spot is the measured pyrometer probe.

Numerical simulations of the flow field coupled to a thermal analysis of the material have been carried out at the same test conditions, to reproduce the experimental results and to provide a preliminary characterization of the surface catalicity of the UHTC (ZrB_2 + SiC). The results are shown in Figure 61.

9.3 Experimental-Numerical Correlation

The Figure 62 shows that the experimental results match quite well the numerical ones with non catalytic wall condition. This shows that, according to other literature studies, UHTC materials exbit at very high temperatures, a non catalytic behaviour.

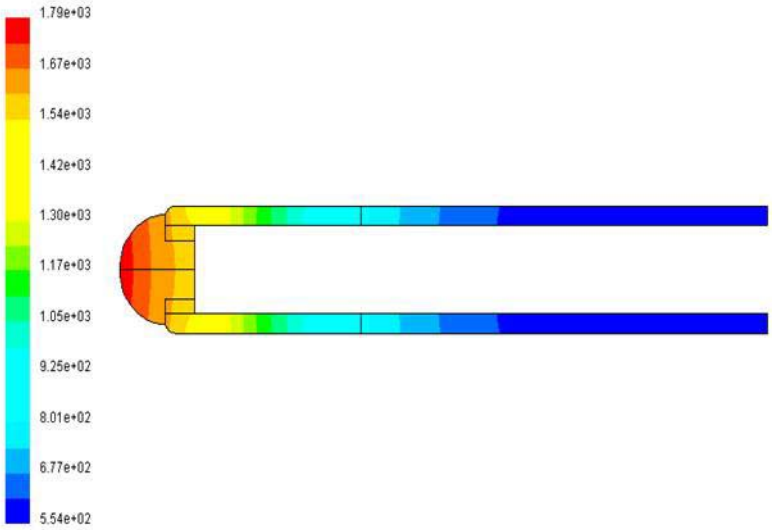

Figure 61 Computed temperature distribution

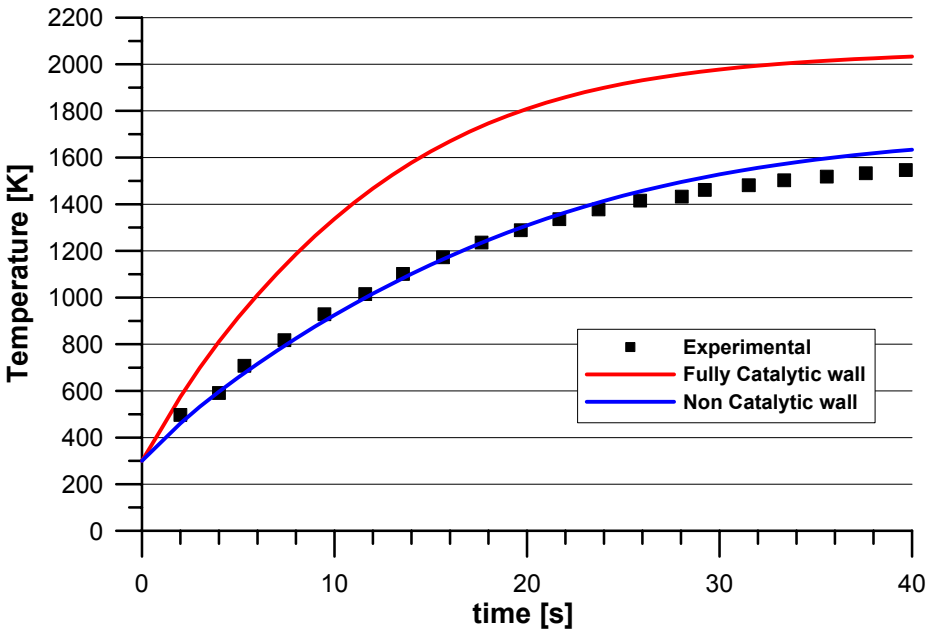

Figure 62 Comparison between experimental data and numerical results based on different assumptions on the surface catalytic properties

9.4 Emissivity characterization

Figure 63 (a) shows the images of two UHTC specimens: the right one has been exposed to the high enthalpy flow, the left one is virgin. It is evident that the colour of the material surface is

different after the exposition to the high enthalpy flow. This can be explained by the surface reactions that have changed the surface composition during the test.

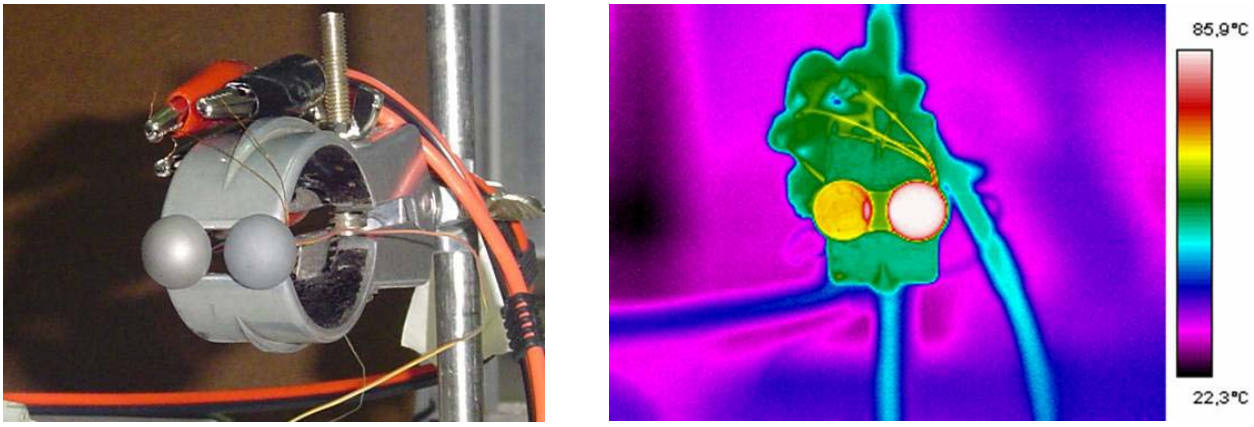

Figure 63 (a) Comparison between two UHTC specimens: the right one has been exposed to the high enthalpy flow; the left one is virgin and (b) infrared image of the two specimens

To evaluate the emissivity of the two specimens an experimental analysis has been carried out heating the models at different temperatures (using an electric resistance or another heating device). The temperature has been measured with thermocouples and looking at the specimens with the infrared camera. Figure 63 (b) shows also an infrared image of the two specimens. The infrared camera was detected different surface temperatures; indeed, this is due to two different spectral emissivity value, because the temperature detected by the thermocouples are coincident within an error of ± 0.5 °C.

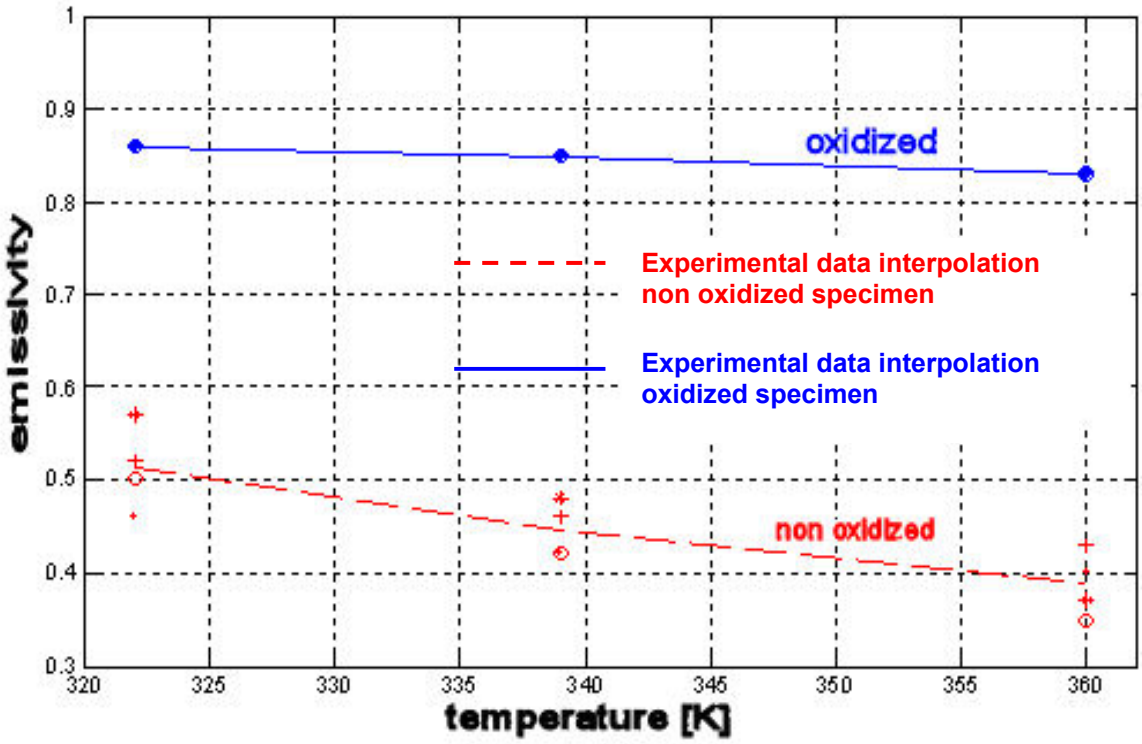

Figure 64 A comparison between oxidized and non-oxidized heated specimen

The infrared camera software allows evaluating the emissivity if the value of the temperature is known. In this way the surface emissivity has been measured at different temperatures.
Many tests have been also carried out and the results are shown in Figure 64.

After the test, the specimen emissivity is higher than the virgin material one. In fact, the UHTC specimen, after the test, exhibits an emissivity between 0.4 and 0.5, for temperatures between 320 K and 360 K, with a value decreasing with the temperature. This trend has been confirmed by many other tests. During the high-enthalpy flow exposition, the surface composition specimen changes and the emissivity becomes relatively high.

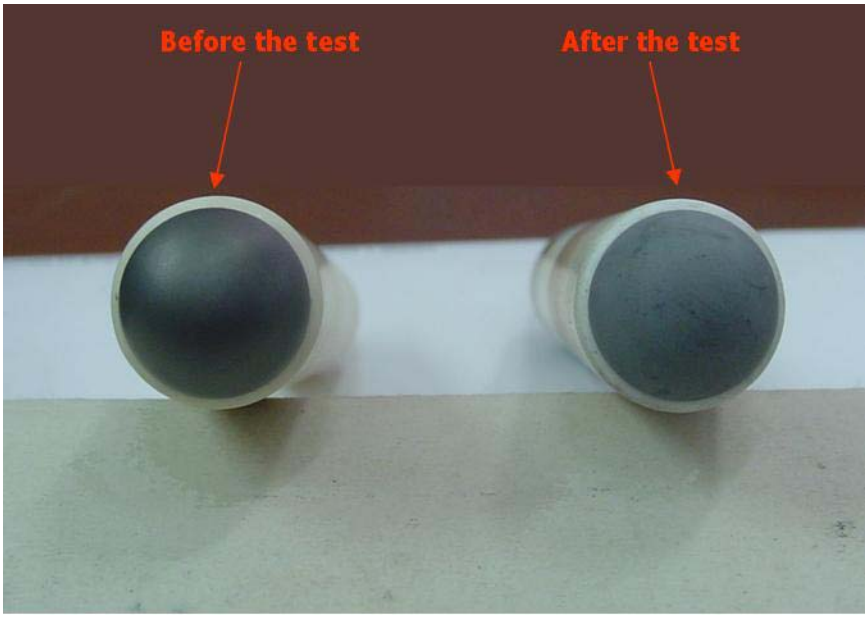

Figure 65 the specimen before and after the wind tunnel test

From measured effects with a balance of precision, has been possible record only a negligible variation of mass of the high-enthalpy exposed specimen.
Figure 65 shows the different coloration of the two specimen (oxidized and non oxidized), in particular, the opacity is noticed praiseworthy to the oxide superficial layer on the specimen after the test.
The oxidized specimen emissivity, at temperatures included between the environmental temperature and 100 °C, is more elevated than non oxidized specimen one. The oxidized specimen emissivity values are included among 0.57 and 0.35 and diminish sensitively with increasing temperature.
This dependence from the temperature results much less marked for the oxidized specimen, whose emissivity values are a bit more than 0.8, according to what stated by the pyrometer and the infrared camera at higher temperatures raised in hypersonic gallery and during the test at atmospheric pressure.

9.5 Absorbing effects due to Barium Fluoride

The transparency in the infrared wavelength of the fluoride barium window is not of 100%; the transmissibility versus wavelength, given by constructor, is shown in Figure 66.

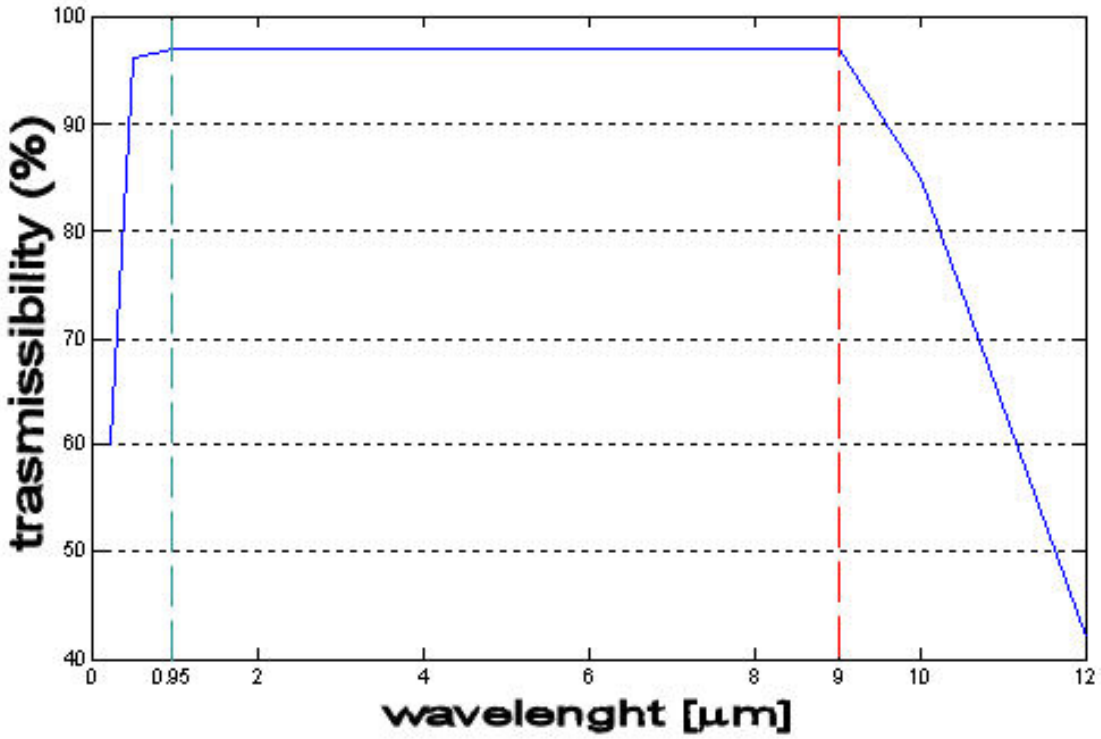

Figure 66 fluoride-barium window transmissibility

To take into account the fluoride-barium window transmissibility in the infrared wavelength, the Planck's law is modified as following:

$$I_{\lambda,T} = \tau \frac{\varepsilon_{\lambda,T} C_1}{\lambda^5 \left[\exp\left(\frac{C_2}{\lambda T} \right) - 1 \right]} \tag{5}$$

where τ is window transmissibility.

Since, instrumentation measures the 'new' emissivity $\varepsilon' = \tau \cdot \varepsilon$.
As shown in Figure 66, in the utilized wavelength range ($\lambda_1 = 0.95$ µm and $\lambda_2 = 1.05$ µm for the pyrometer and $\lambda = 9$ µm for the infrared camera) the fluoride barium window transmissibility should be $\tau = 0.97$.

10 Tests with UHTC and Tungsten specimens with Nitrogen flow

Figure 67 shows a picture of the experimental configuration before the tests, while in Figure 68 there are images of the two experimental tests.
In these experimental tests, two specimens of same geometry and size, but with different materials (UHTC and Tungsten) have been tested at the same flow conditions. In both cases, the model was located at a distance of 5 cm from the exit of the torch.
Figure 69 and Figure 70 show a sequence of infrared images during the experimental test with the Tungsten and UHTC specimen, respectively.

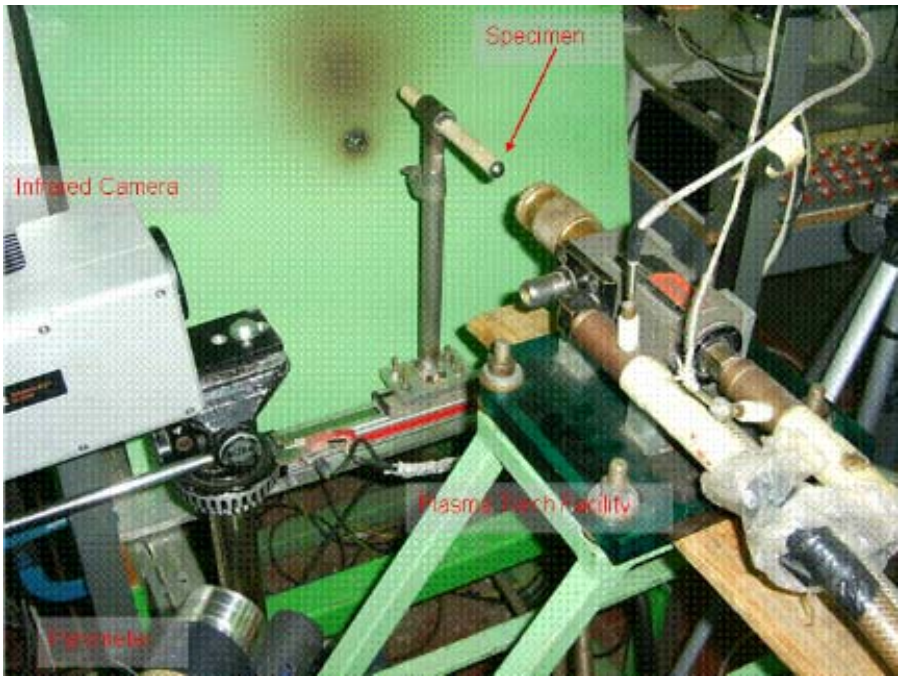

Figure 67 experimental configuration before the tests.

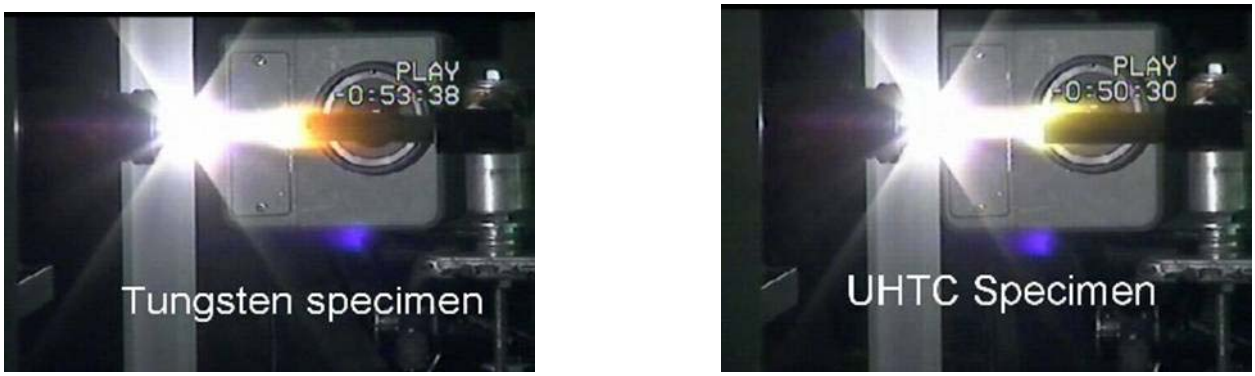

Figure 68 Images of the plasma torch tests

t = 5 s *t = 10 s*

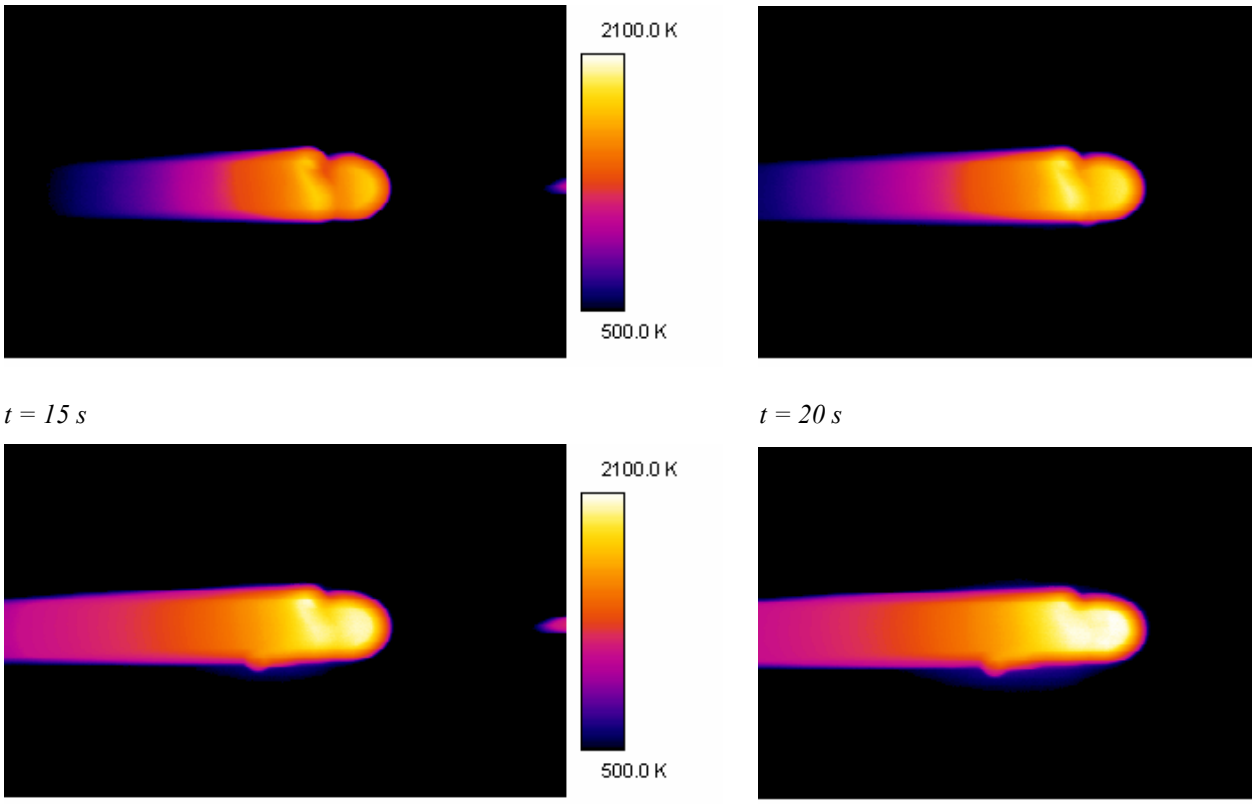

Figure 69 Infrared images during the test with the tungsten specimen

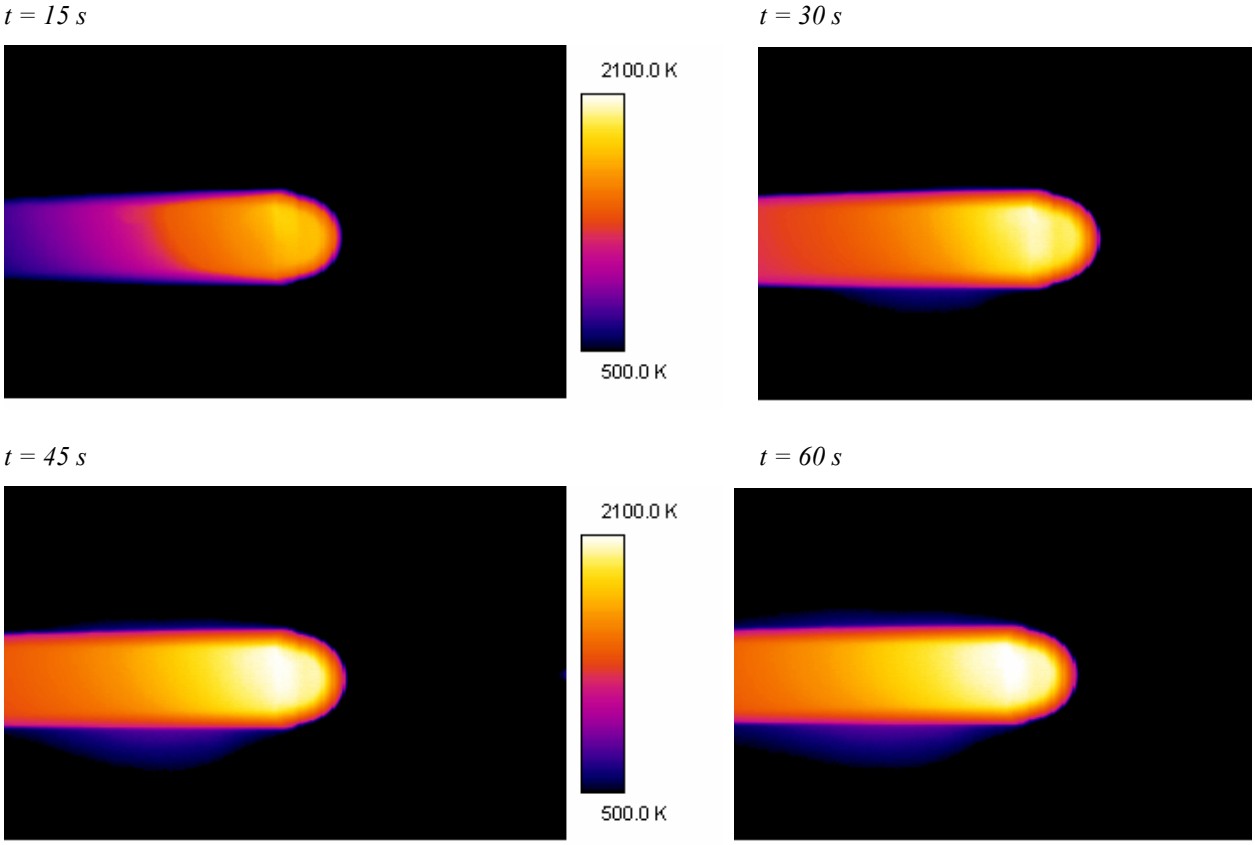

Figure 70 Infrared images during the test with the UHTC specimen

The time histories of the temperatures during the tests are shown in Figure 71, and the tests conditions are reported here, too.

In the case of the tungsten specimen (clearly oxidized when exposed to a high flow with oxygen), the measured emissivity value was $\varepsilon = 0.8$. In the UHTC (ZrB_2 + SiC) specimen experimental test, at the end of the test (temperature of about 2000 K) the estimated emissivity value was $\varepsilon = 0.95$.

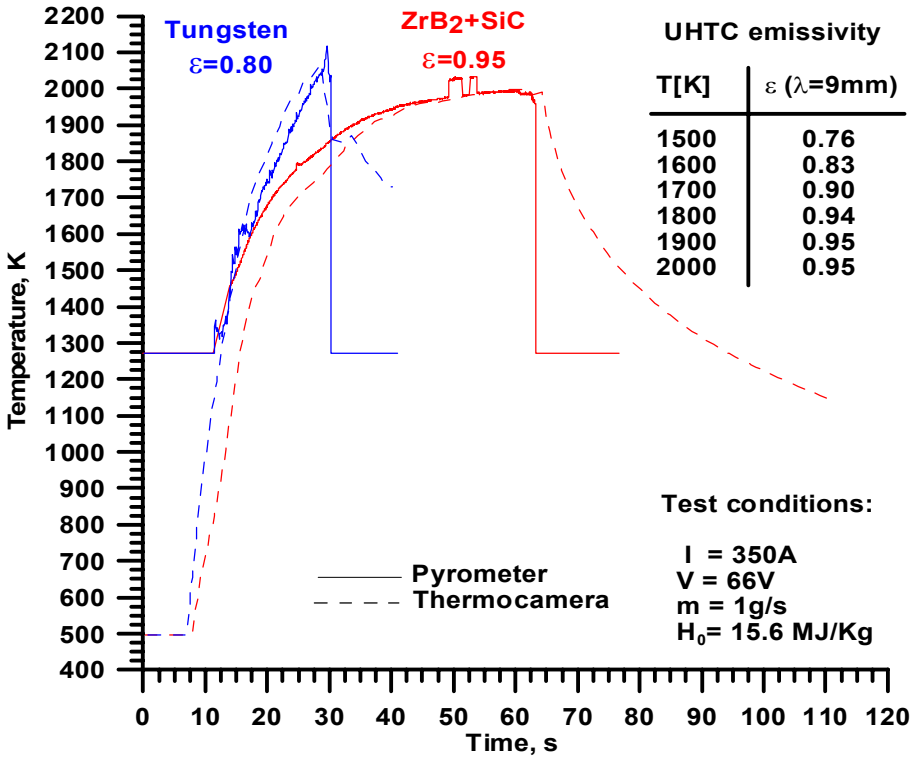

Figure 71 Temperatures measured during the tests

Numerical simulations have been carried out to obtain an indirect evaluation of the surface catalytic recombination constant k_{wi} related to the surface recombination coefficient γ_{wi} ($\gamma_{wi} = 0$ for a non catalytic wall and $\gamma_{wi} = 1$ for a fully catalytic wall).

The time history temperature during the tests has been computed for different values of γ_{wi} and compared to the experimental one, obtained with the pyrometer at a point located at 3 mm distance from the stagnation point.

Comparing the numerical and experimental results, it was found a partial cataliytic behaviour for Tungsten ($\gamma_{wi} = 0.001$, corresponding to $k_{wN} = 0.16$), as shown in Figure 72. These values are in agreement with literature data.

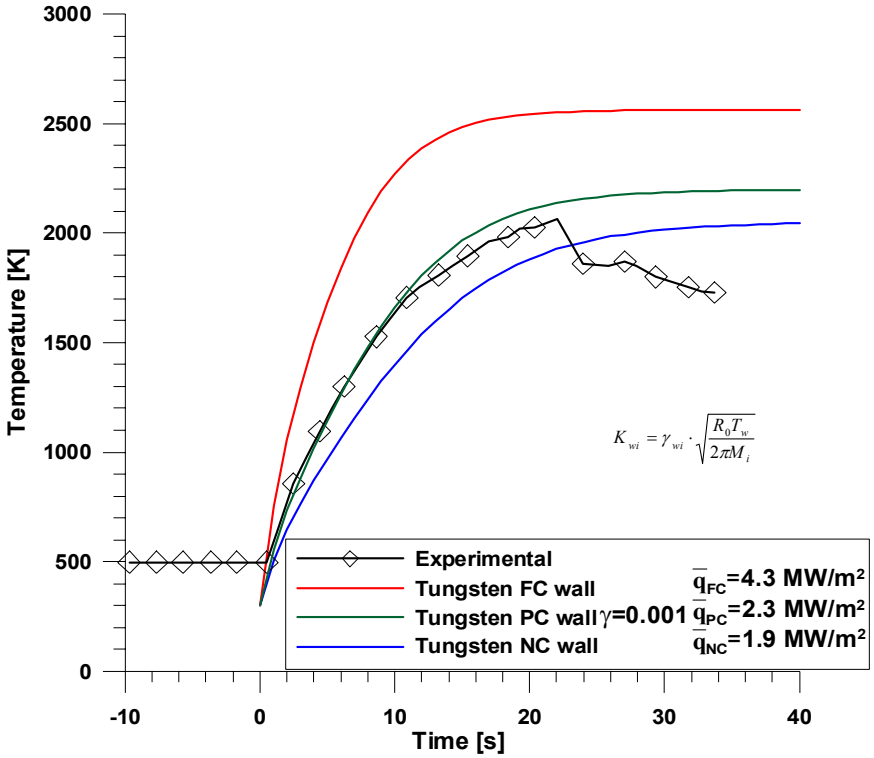

Figure 72 Comparison between experimental and numerical results for the test with the Tungsten specimen. The temperature is computed at 3mm distance from the stagnation point

The UHTC (ZrB2 + SiC) specimen exhibits a non catalytic behaviour, as already found before and as shown by Figure 73.

The non catalytic behaviour seems to be related to the formation of a surface layer of SiO_2, as shown by the microscopic analysis of the specimen after the test (see Figure 74). In fact literature data suggest that the surface of SiO_2, has a very low catalytic recombination behaviour (Ref. 8,9). The presence of a surface layer of SiO_2 is also in agreement with the high values of the surface emissivity, according to the literature (Ref. 10).

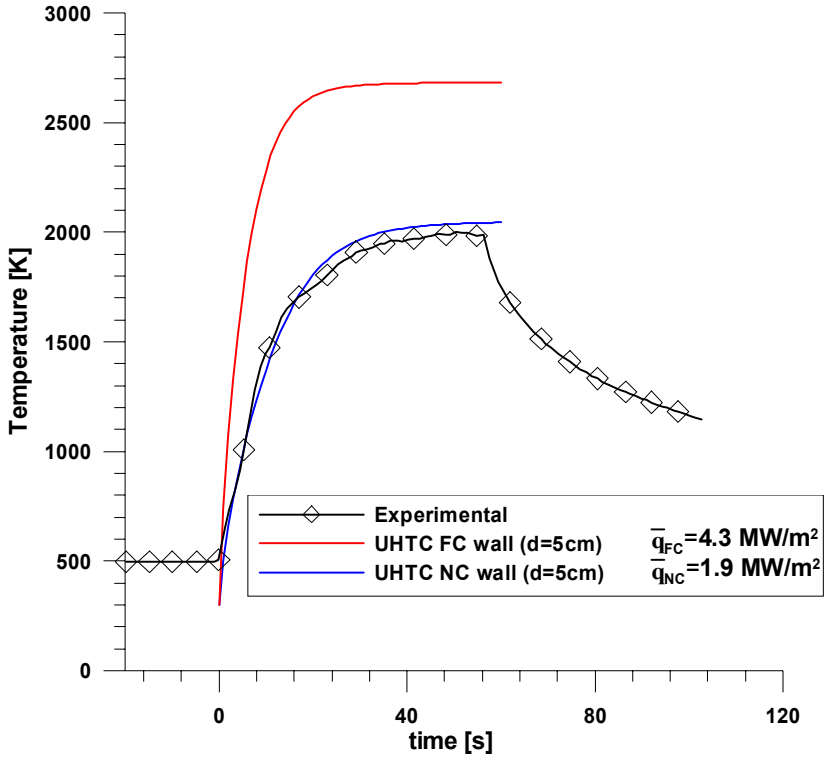

Figure 73. Comparison between experimental and numerical results for the test with the UHTC specimen. The temperature is computed at 3mm distance from the stagnation point

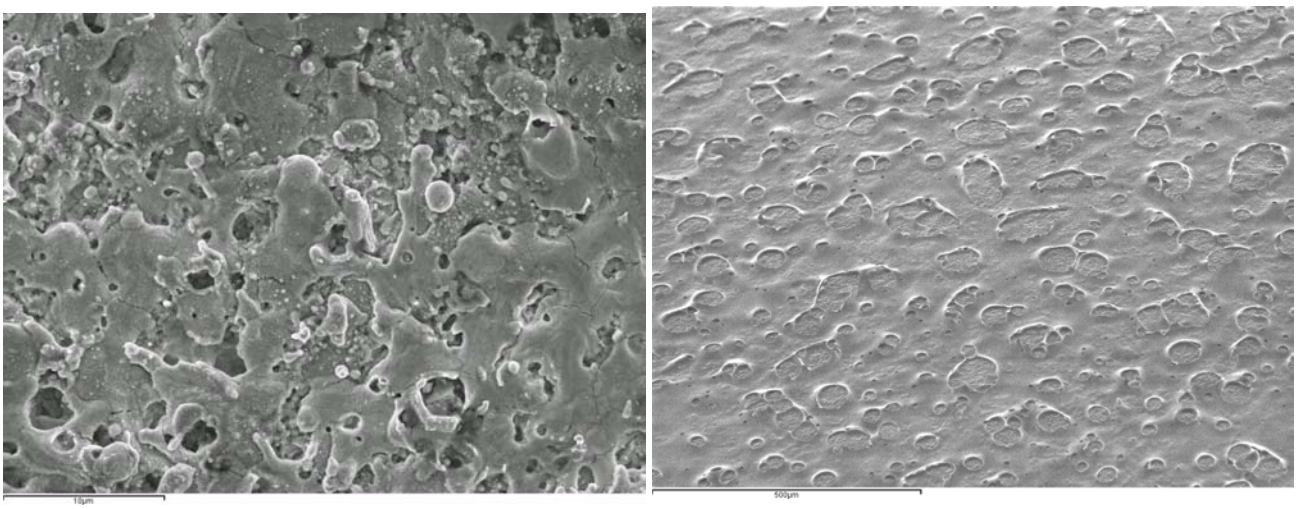

Figure 74 surface's virgin specimen at left and surface 'specimen after the test at right, with layer of SiO_2

11 Experimental Tests with UHTC specimens with Nitrogen and Argon Mixture Flow

Other two tests have been carried out in atmospheric pressure, with the same previously described experimental setup. The Figure 75 shows the experimental setup with the specimen on the support, 5 cm far away from the torch exit, the pyrometer on the left and the infrared camera on the right.

In the first experimental test, the tester was invested by a flux of about 1 g/s Ar and 0.5 g/s N_2, with an average power of 19 KW and a total average specific enthalpy of about 12.6 MJ/Kg at torch exit. The Figure 76 shows the time history temperature on the UHTC (ZrB_2 + SiC) specimen, noticed with the pyrometer and the thermograph: a temperature of about 1800°C has been reached after about a minute.

During experimental test, the change from the one-wavelength pyrometer mode to dual-colour pyrometer mode was made, measuring, in this way, a superficial emissivity value of the UHTC material between 0.85 and 0.89. The shows different infrared images grabbed during the test at different times.

After the experimental test, the same characteristics, corresponding substantially at the test described previously, was observed on the exposed plasma-torch specimen. The specimen surface has a wrinkled protective superficial layer of SiO_2, typically light-grey coloured, as shown in Figure 79.

Figure 75 Experimental setup

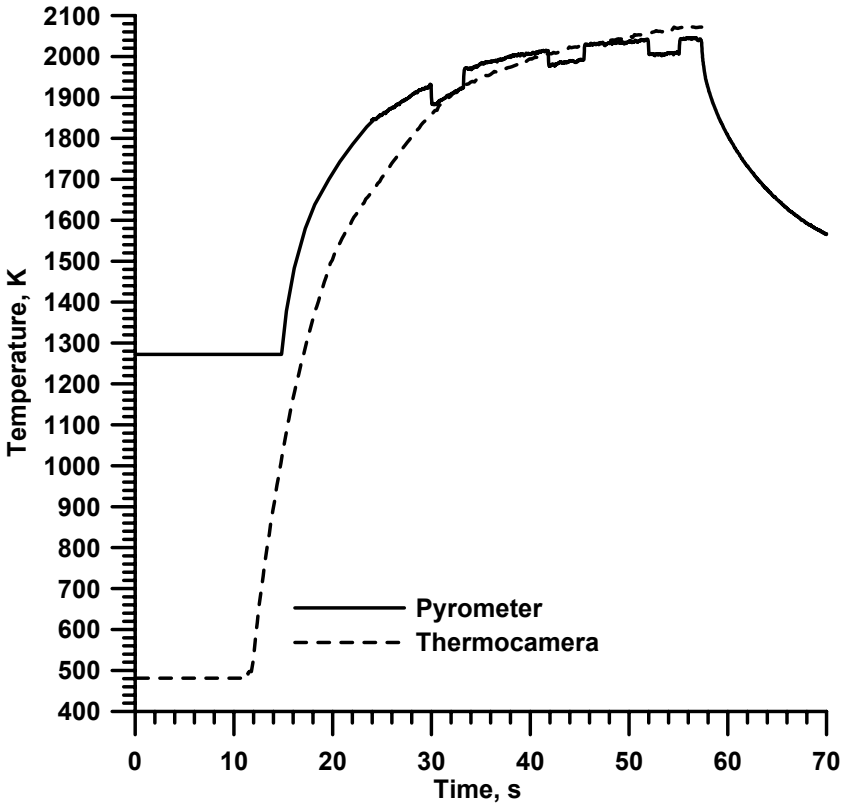

Figure 76 Temperature varying with time, during the test

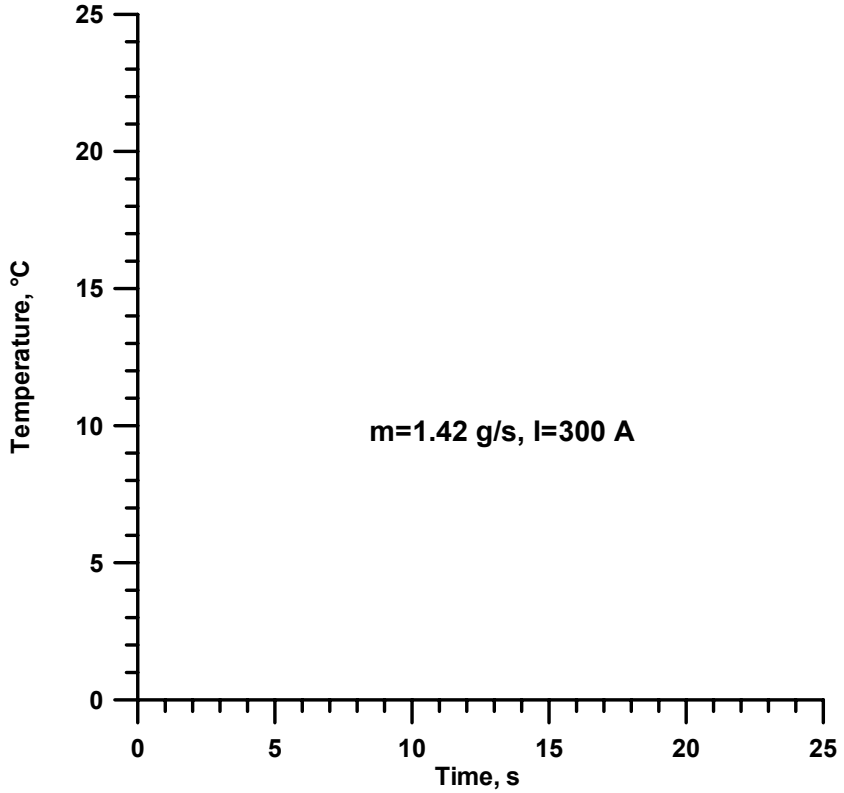

Figure 77 Experimental – numerical correlation

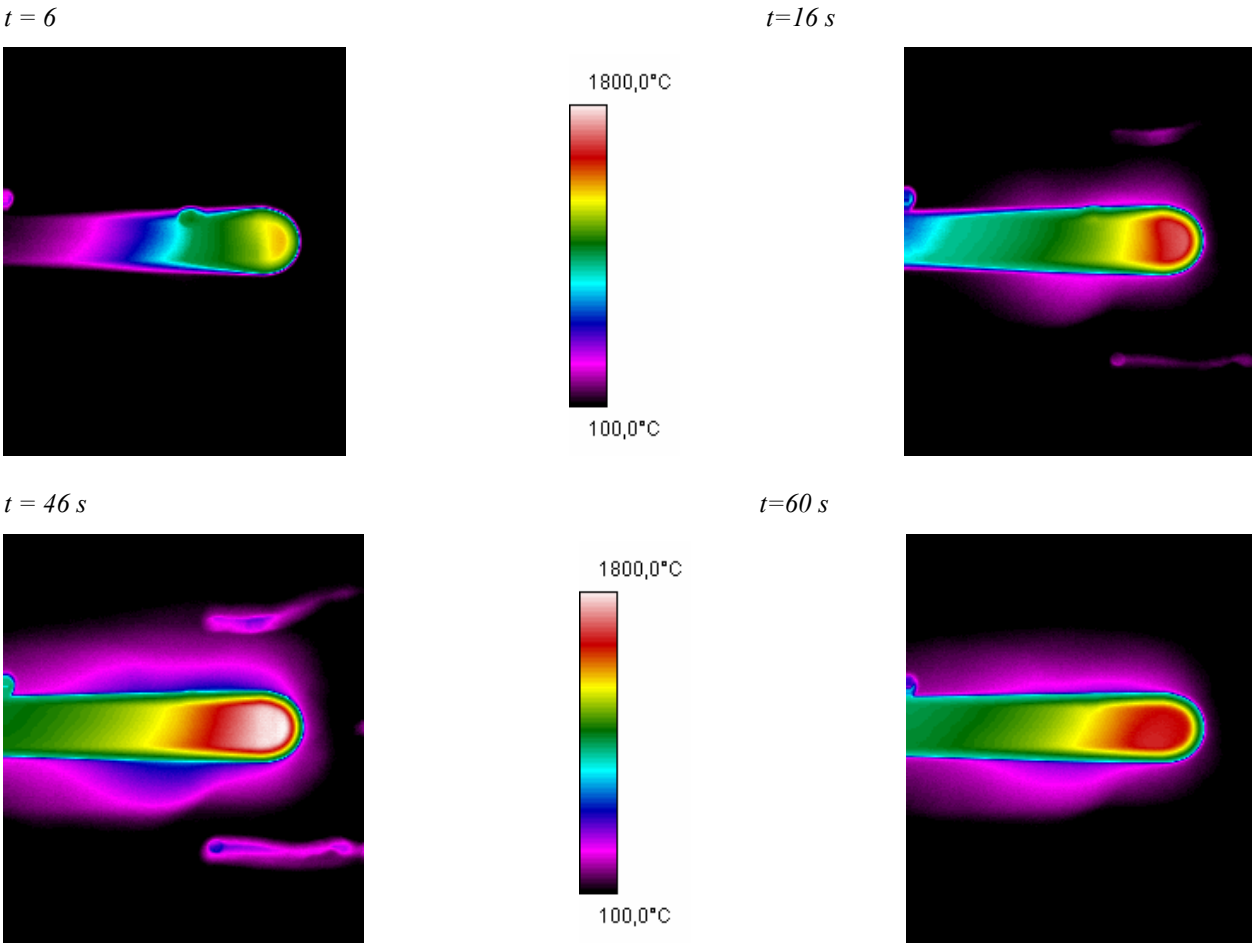

Figure 78 Infrared images at different times during the first experimental test. At time t=60 s, the model is in cooling phase.

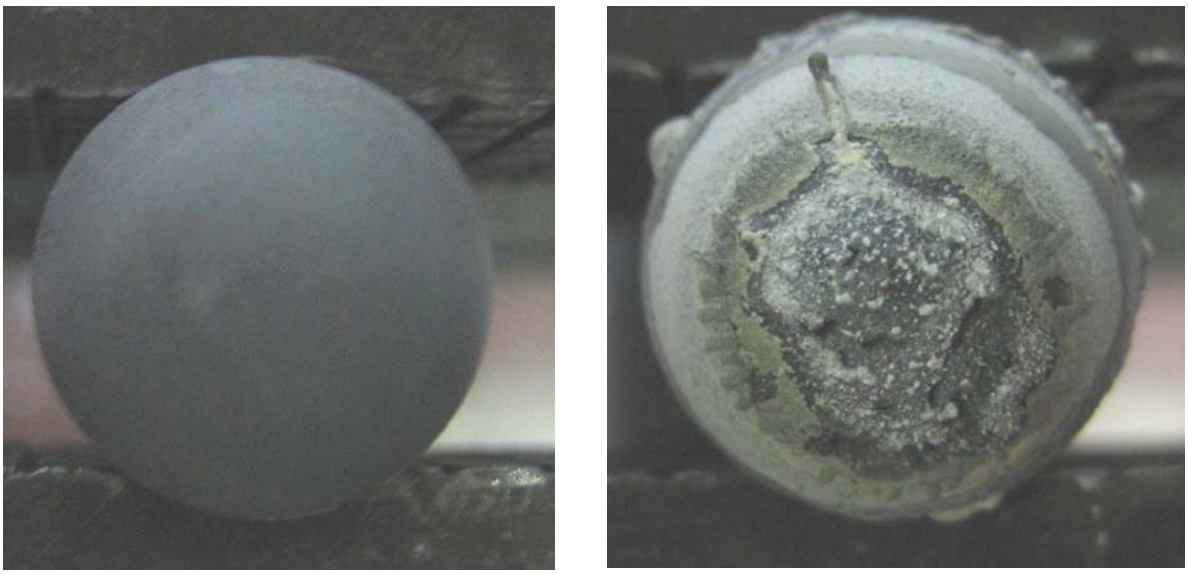

Figure 79 UHTC specimen after the first test (T=1800°C) (a) and after the second test (T=2400°C) (b)

In the second experimental test, the model was invested by a flux of about 0.85 g/s Ar and of 0.65 g/s N_2 with an average power of 26 KW, corresponding to a total average specific enthalpy of 17.5 MJ/Kg at torch exit, to investigate the time history temperature.

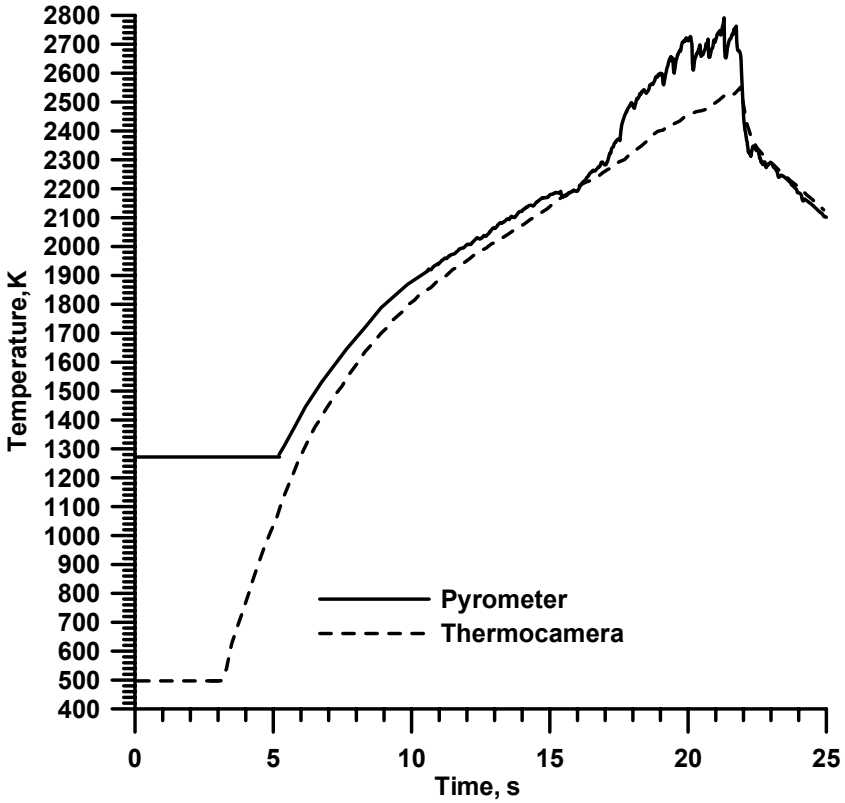

Figure 80 Temperature varying with time, during the test

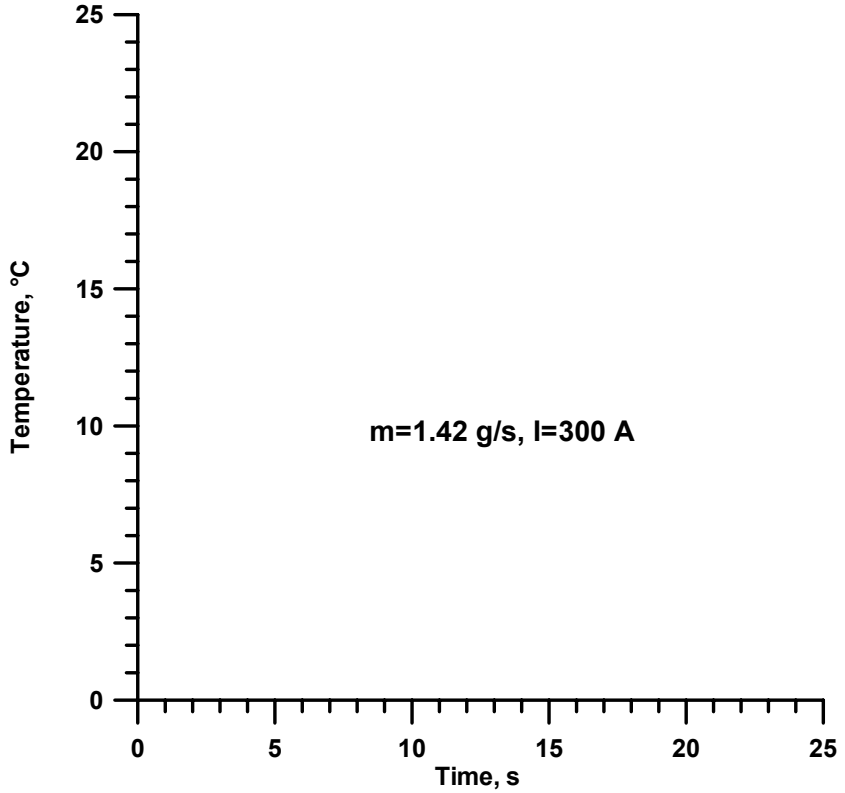

Figure 81 Experimental – numerical correlation

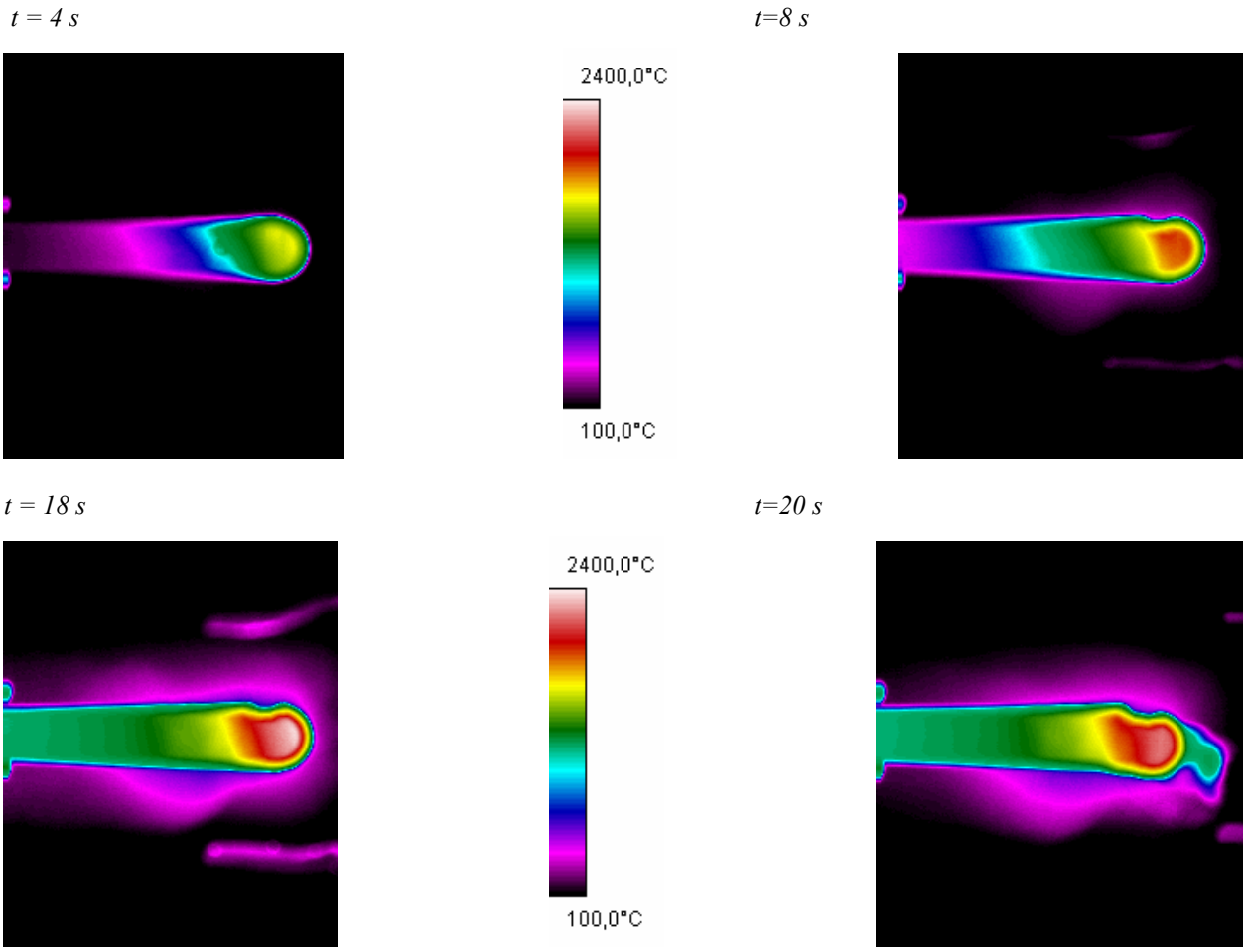

Figure 82 Infrared images at different times during the second experimental test

The temperature on specimen in the experimental test is shown in Figure 80, and infrared images acquired during the test are shown in. In this case, after about 20 seconds, a temperature of 2400°C was reached.

The allumina support hold up the specimen during all the tests, but it was strongly damaged with evident break-ups in correspondence of the junction between the two materials.

Evident superficial chemical reactions took place on the UHTC model surface, as underlined not only by the observation of the champion after the test (Figure 79 (b)), but even from the infrared images, that show evident vapours issue from the surface in the phase of maximum heating, as shown in for t=20s.

After the described experimental test, a microscopic analysis detected the formation of a SiO_2 superficial layer, a ZrO_2 sub-layer, and a following zone characterized by a depletion of SiC at the boundary of the original UHTC (ZrB2 + SiC) material, as shown in Figure 83 and Figure 84.

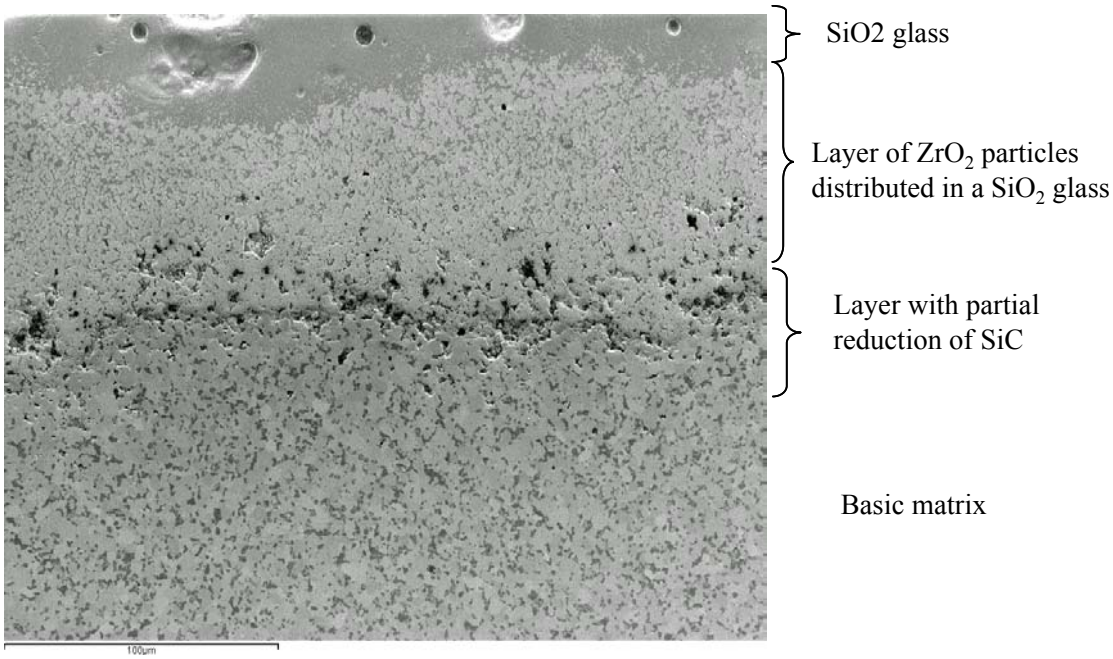

Figure 83 Specimen microscopic image after the described experimental tests

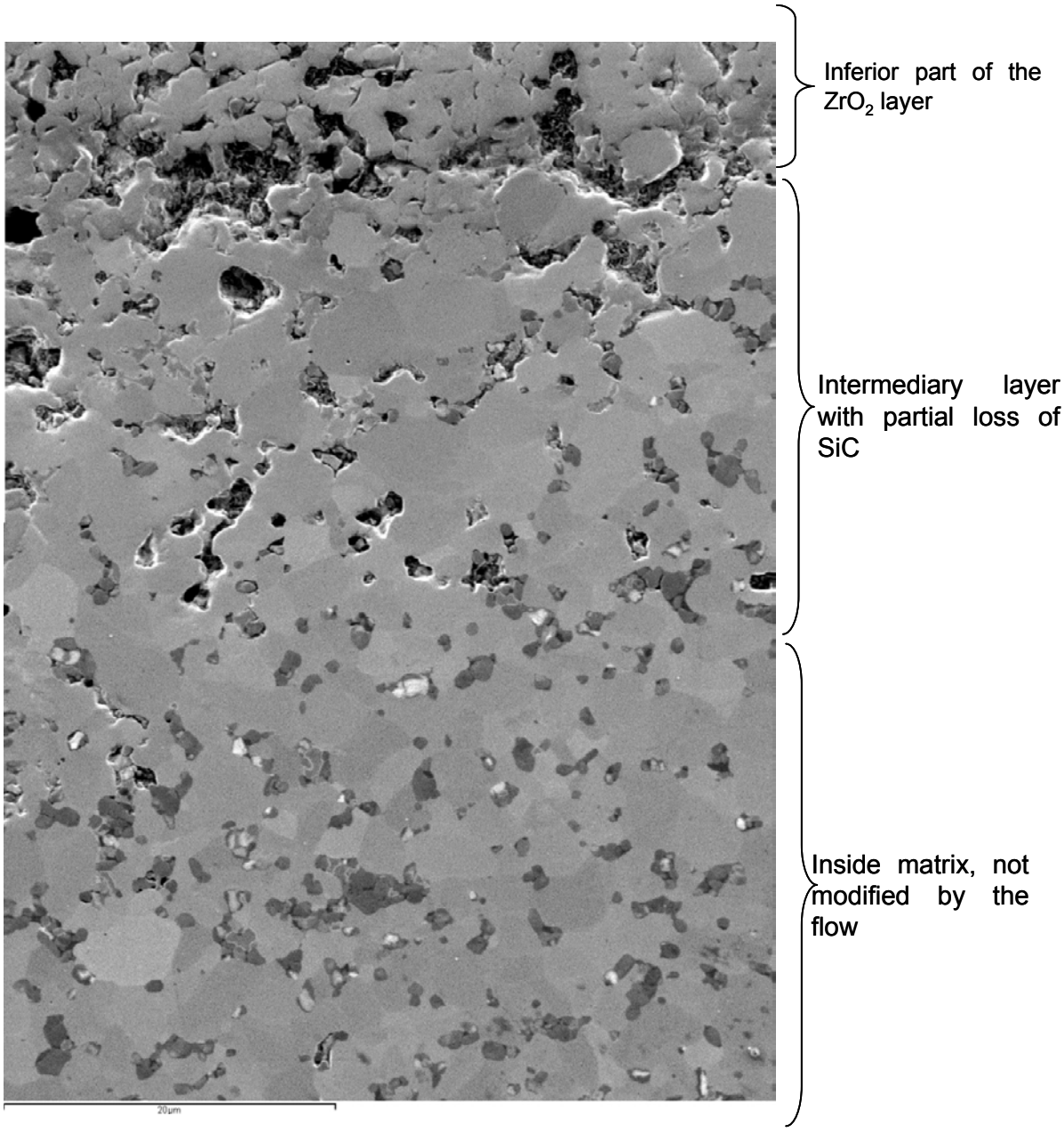

Figure 84 Enlargement of the region with partial reduction of SiC and of the inside part of the material

12 Experimental Tests with UHTC specimens with Nitrogen Flow

After the experience about the UHTC specimen tests previously descripted, a new strategy was assumed. Fixing working fluid's mass flow rate, the power at arc-heater was gradually raised to heat the specimen up to high temperature with a controlled raise.
The power at arc-heater, and so in series the total specific average enthalpy at torch exit, raised every time the measured temperature on specimen get to a plateau.
Figure 85 shows two images of the experimental set-up. The shape and size for the UHTC specimen and for the holder are the same already investigated in previous tests.
The holder is connected to a mechanical computerized system that can be translated at the desired position. For the present tests, the specimen has been positioned at 5 cm far away from the torch exit, as shown in Figure 86. This distance was established by a numerical analysis to obtain heat flux interesting value and, hence, temperature specimen in the range of interest, said around 2000 °C. The diagnostic system includes a dual-colour pyrometer and an infrared thermo-camera, both positioned outward chamber-test.

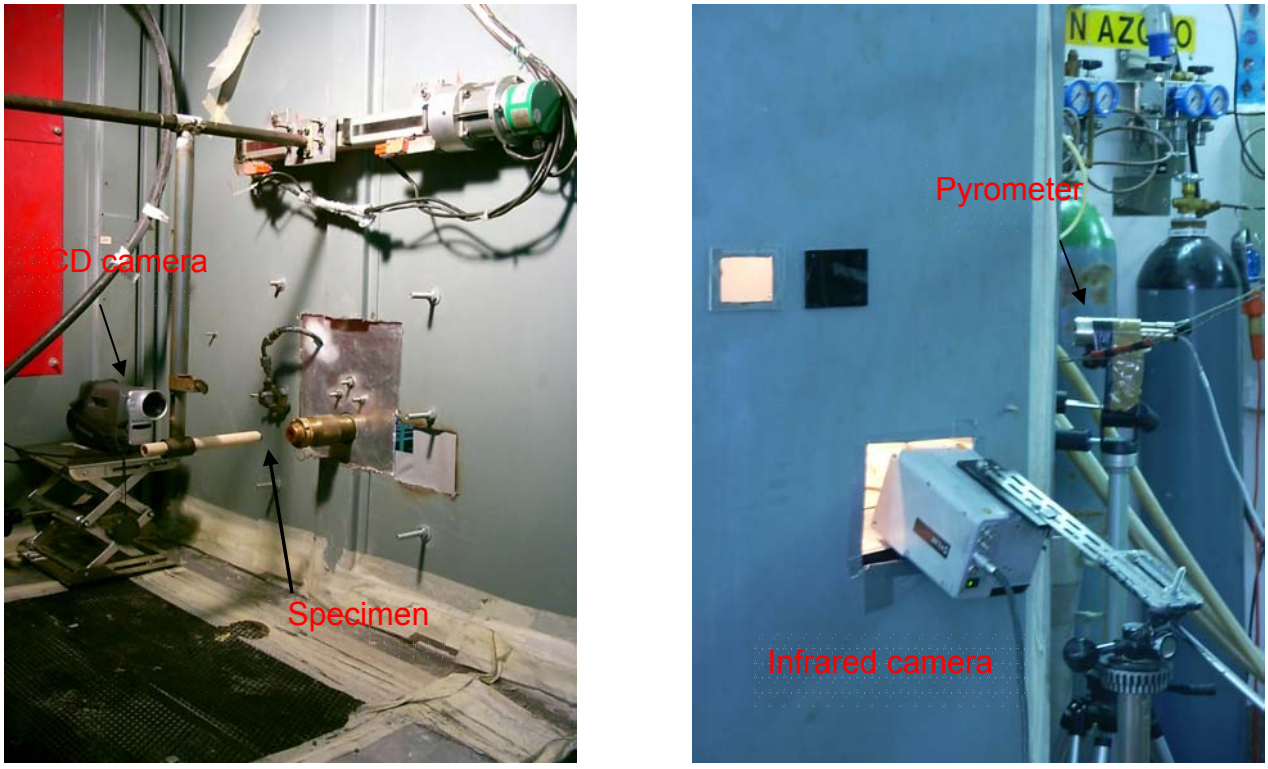

Figure 85 Experimental setup

Two tests have been carried out. The time histories temperature detected by pyrometer are shown in Figure 89.In both cases a nitrogen plasma flow was supplied with a mass flow rate of 1 g/s.
During first experimental test, the initial electrical power was 21 KW and the total average specific enthalpy was about 14.8 MJ/Kg at exit torch.
As shown in Figure 89 (red-line), when the temperature reached a steady value of about 1800°C (after about a minute), the current was raised from 350 A to 400 A. Correspondingly, the power

was raised from 21 KW to 26 KW, so that the total average specific enthalpy was raised from 14.8 MJ/Kg to 16.6 MJ/Kg at exit torch.
At these conditions, the temperature of the UHTC specimen reached a value of about 1900°C.
During the test, changing the pyrometer operation mode from a single-colour to a dual-colour, the spectral emissivity of the UHTC specimen was evaluated between 0.85 and 0.89.
Figure 89 shows different infrared images detected during the test at different times.
During second experimental test, the initial electrical power was 21 KW (corresponding to current and voltage of 350A and 60V, respectively). The total average specific enthalpy was about 17.3 MJ/Kg at exit torch.

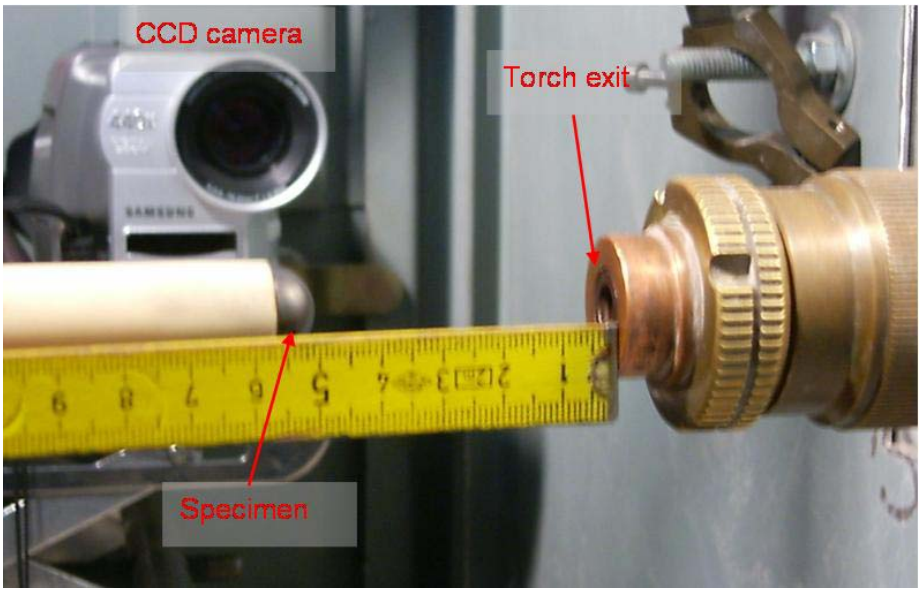

Figure 86 the specimen has been positioned at 5 cm far away from the torch exit

When the temperature reached a steady value, as shown by Figure 88 (black-line), the current was raised from 350A to 400A. Since, the power was raised from 21 KW to 26 KW, and the total average specific enthalpy was raised from 17.3 MJ/Kg to 19.7 MJ/Kg.

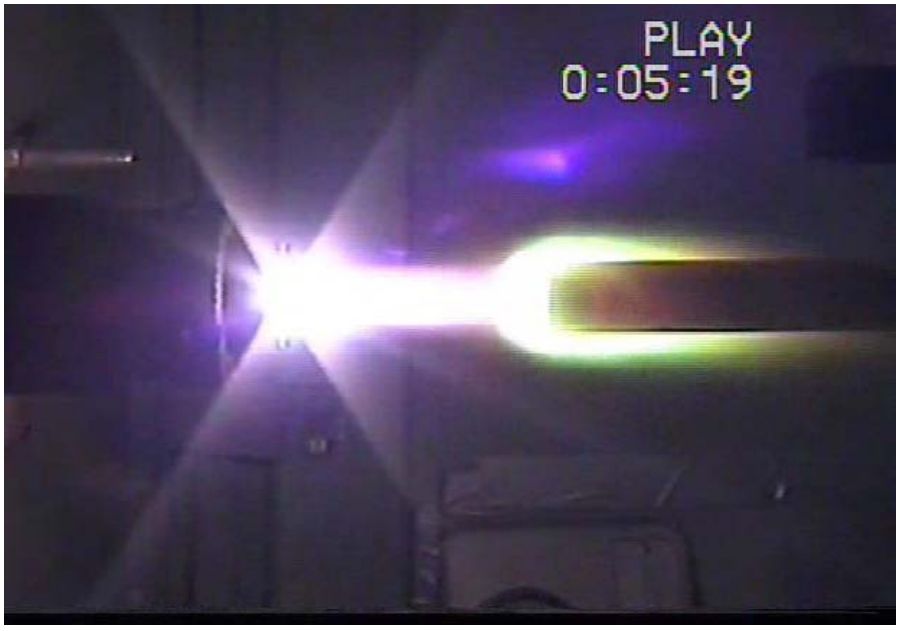

Figure 87 the specimen during the test

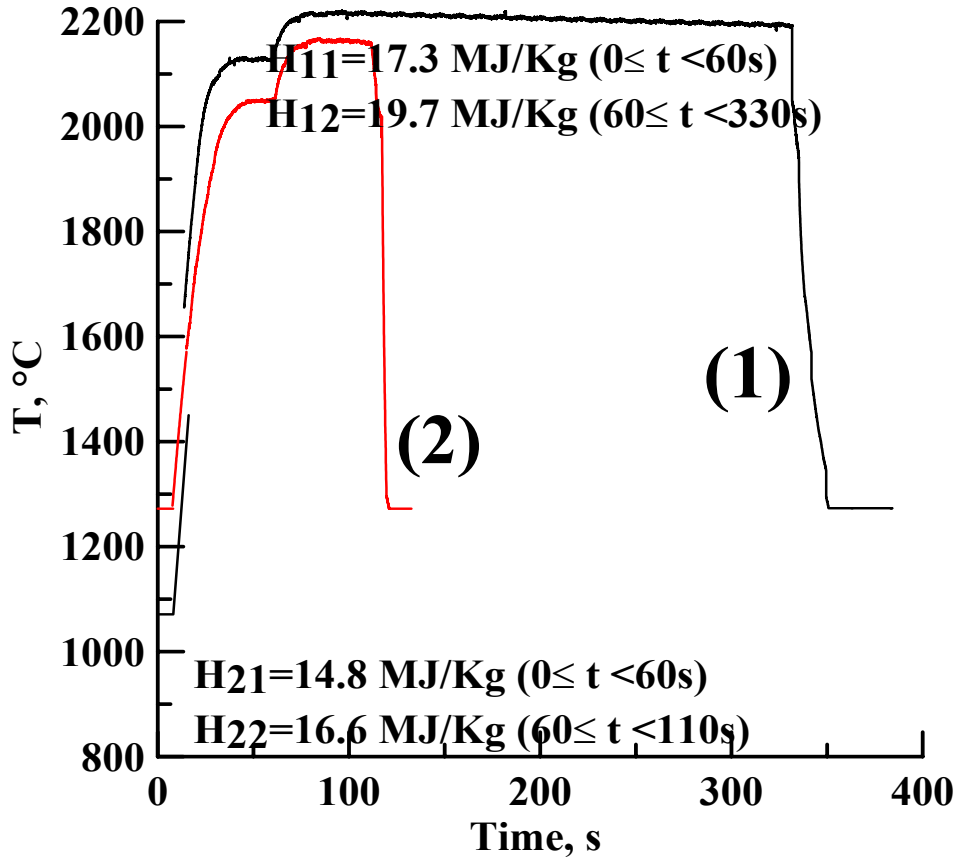

Figure 88 Temperature varying with time, during the two experimental tests

t = 20 s

t = 45 s

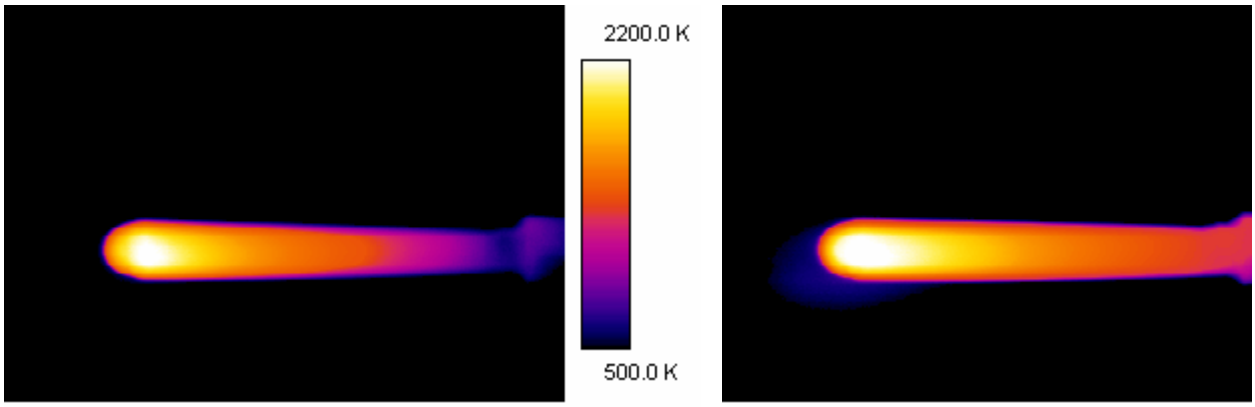

t = 80 s

t = 110 s

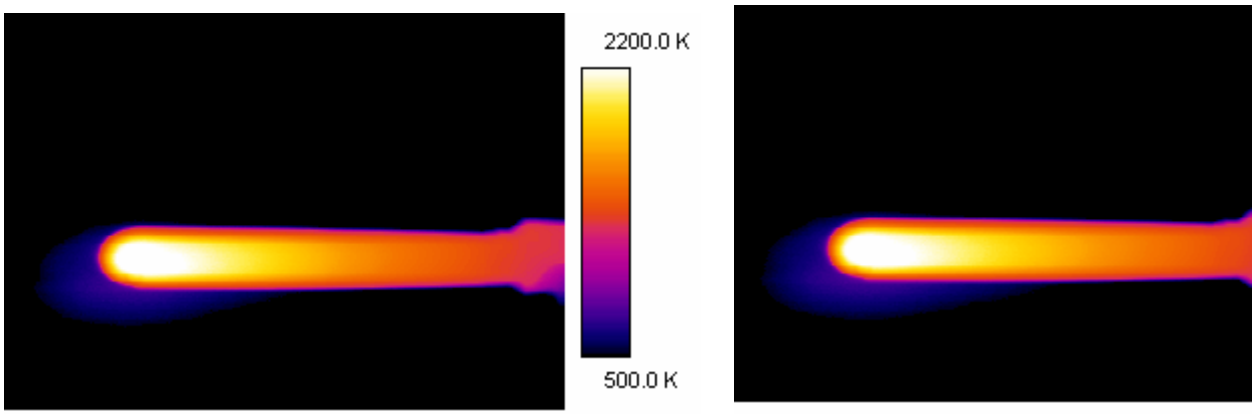

Figure 89 infrared images grabbed during the first experimental test at different times

Figure 90 (a) UHTC specimen and (b) the model, after the first experimental test

Figure 91 UHTC specimen after the second experimental test

Figure 92 UHTC specimen after the first experimental test (left) and second one (right)

t = 30 s *t = 60 s*

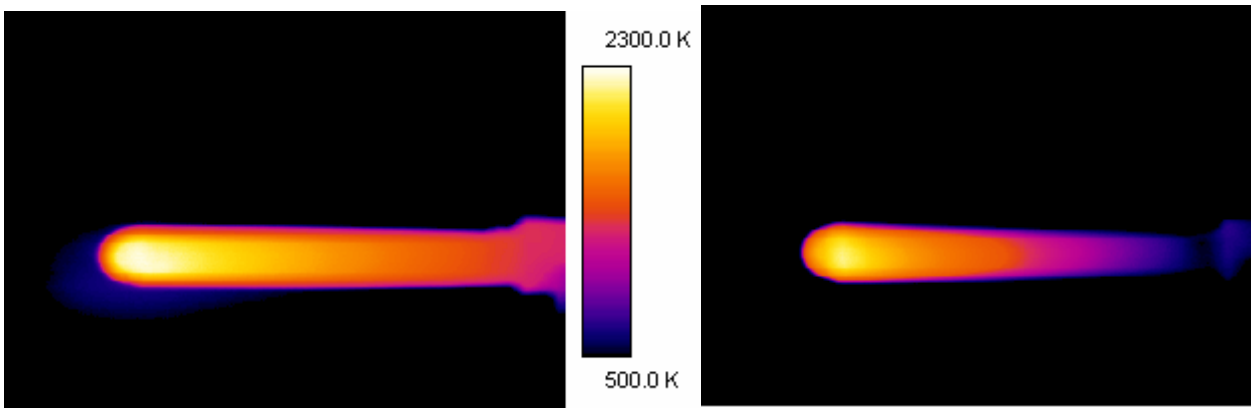

t = 120 s *t = 330 s*

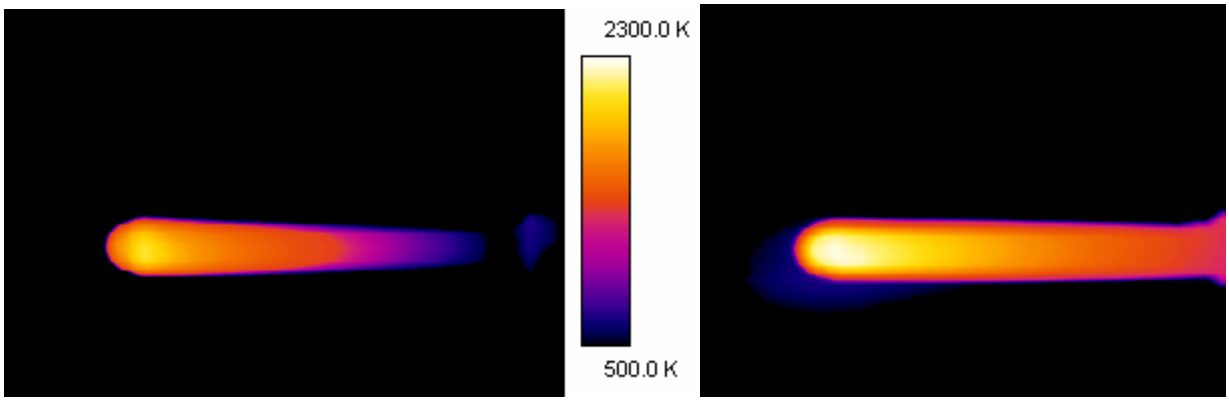

Figure 93 infrared images grabbed during the second experimental test at different times

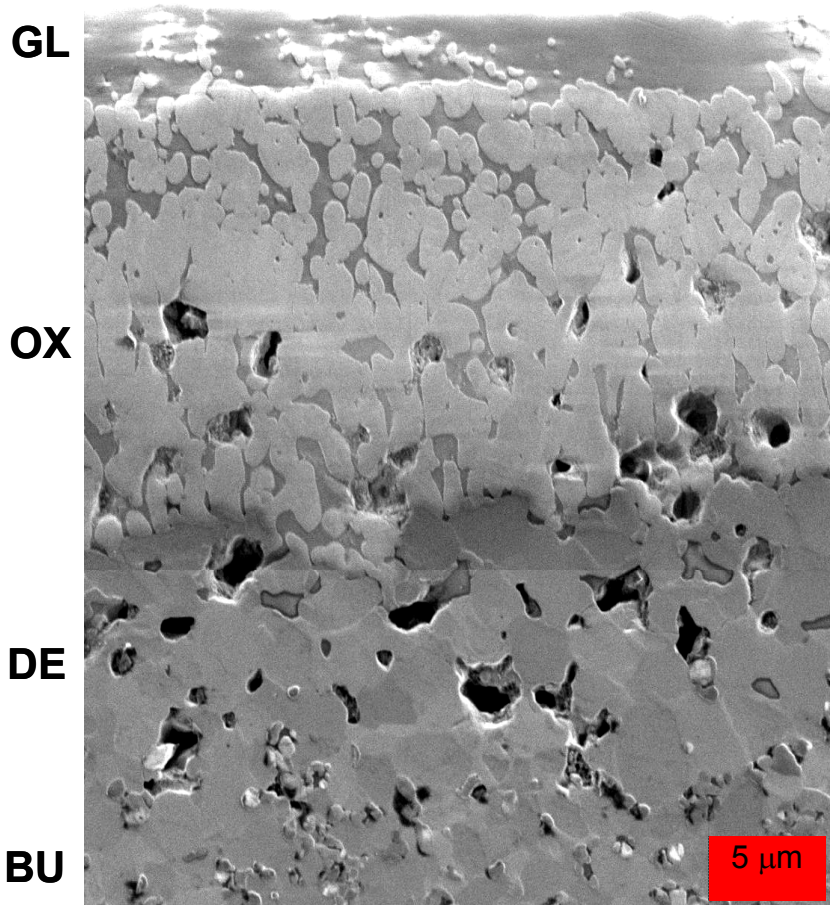

Figure 94 Microscopic image of a section's UHTC specimen after the test

Microscopic analysis of the specimen after the test pointed out that it was covered by an external SiO_2 surface layer (GL). Moving from the surface to the interior material, a ZrO_2 sub-layer (OX) and then by a region characterized by a depletion of SiC (DE) at the boundary of the original UHTC (ZrB_2 + SiC) material (BU), as shown in Figure 94.
These results show that the UHTC material seems to well withstand temperatures up to 2000 °C in the plasma torch environment, due to the presence of a stable protective oxide layer. On the contrary, inspection of the specimen after the high-enthalpy test, since in presence of high dissociation degree of oxygen, shows that at these conditions to strong surface reactions occur so that the material is completely damaged (see Figure 79).
The catalytic performances of UHTC materials differ substantially from those of pure metals or pure ceramics. It is also evident that the catalytic behavior of UHTC materials under transient, high-temperature plasma exposures must be closely coupled with development of oxide layers. Since, it is important to estimate recombination efficiencies of dissociated oxygen as well as to take into account the evidence of environment-induced oxidation that modifies the surface catalytic efficiency.

13 Experimental Tests with NOSE and UHTC specimen with Nitrogen and Argon Mixture Flow

The experimental tests described in this chapter were made with the experimental setup shown in Figure 75, the specimen was a 5 cm far away from the exit torch. The experimental conditions of the tests are following described. The NOSE USV geometry is reported in
The mass flow rate was about 1.45 g/s with 75% of Argon and 25% of Nitrogen composition. The initial power at arc-heater was about 34 Kw and the total specific average enthalpy (H_0) at torch exit was about 12.8 MJ/Kg. During the experimental test, varying the current at arc-heater, the power at arc-heater varied and accordingly to it the H_0 also varied. The variation of the current at arc-heater was made in correspondence of a temperature plateau. The power at arc-heater varied from about 34 Kw to about 64 Kw, while the H_0 varied from about 12.8 MJ/Kg to about 33 MJ/Kg.
Figure 96 shows the time history temperature during the test. The duration of the test was 420 seconds. Every time the temperature reached a plateau, the current at arc-heater was increased and so, accordingly to this raise, the H_0 at torch exit was also increased. So, the specimen's temperature was gradually increased up to a very interesting value. The final measured temperature was about 2250 °C and the evaluated emissivity was $\varepsilon = 0.9$. In the Figure 98 are shown infrared images of the NOSE-USV specimen at four different time during the experimental test. The only effect of the high temperature flux on the specimen was a very located surface oxidation, maybe ZrO_2, being this "stain" of white colour, as shown in Figure 97. At the moment of writing this thesis, the microscopic analysis is not yet made.

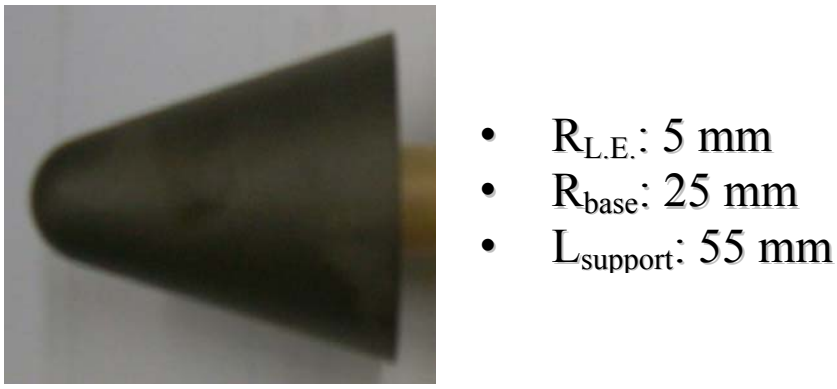

Figure 95 Specimen before the exposure to the flux

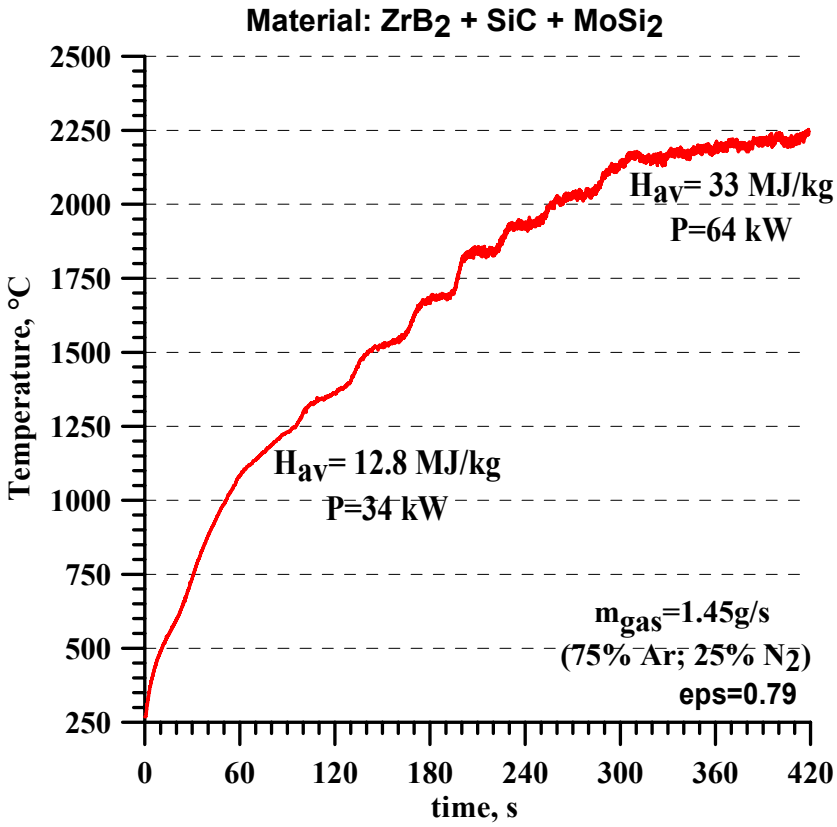

Figure 96 Time history temperature during experimental test


Figure 97 Specimen after the exposure to the flux

t = 120s

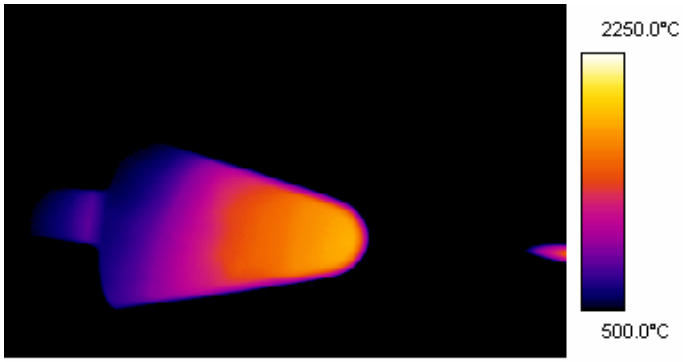

t = 210 s

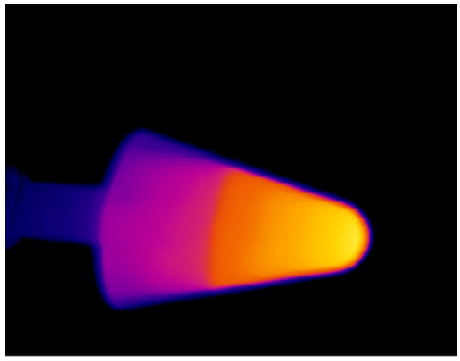

t = 330 s

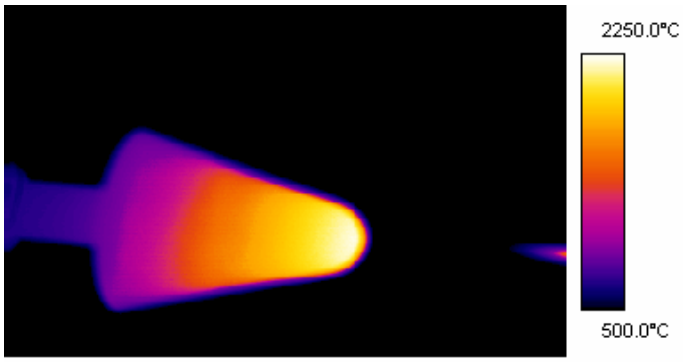

t = 419 s

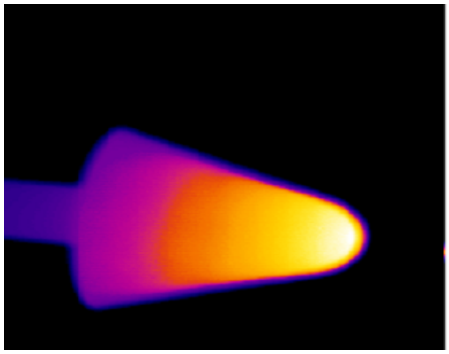

Figure 98 Infrared images of the USV nose during the experimental test

After the test on the NOSE-USV, another specimen was tested with the same procedure. The specimen was made of same composition of NOSE-USV but it had a semi-spherical shape. The power at arc-heater varied from about 26 Kw to about 51 Kw, while the H_0 varied from about 6.9 MJ/Kg to about 24.4 MJ/Kg. The experimental setup is the same as before and it is shown in Figure 75, the specimen was a 5 cm far away from the exit torch. Figure 99 shows the time history temperature during the test. The duration of the test was about 240 seconds and the maximum temperature on the specimen was about 2000 °C with an evaluated emissivity $\varepsilon = 0.9$. In the are shown infrared images of the UHTC specimen at four different time during the experimental test. This sequence shows that the specimen was almost fell down, but it is luckily re-entered in its housing. The only effect of the high temperature flux on the specimen was a very located surface oxidation, maybe ZrO_2, being this "stain" of white colour, as shown in Figure 100. At the moment of writing this thesis, the microscopic analysis is not yet made.

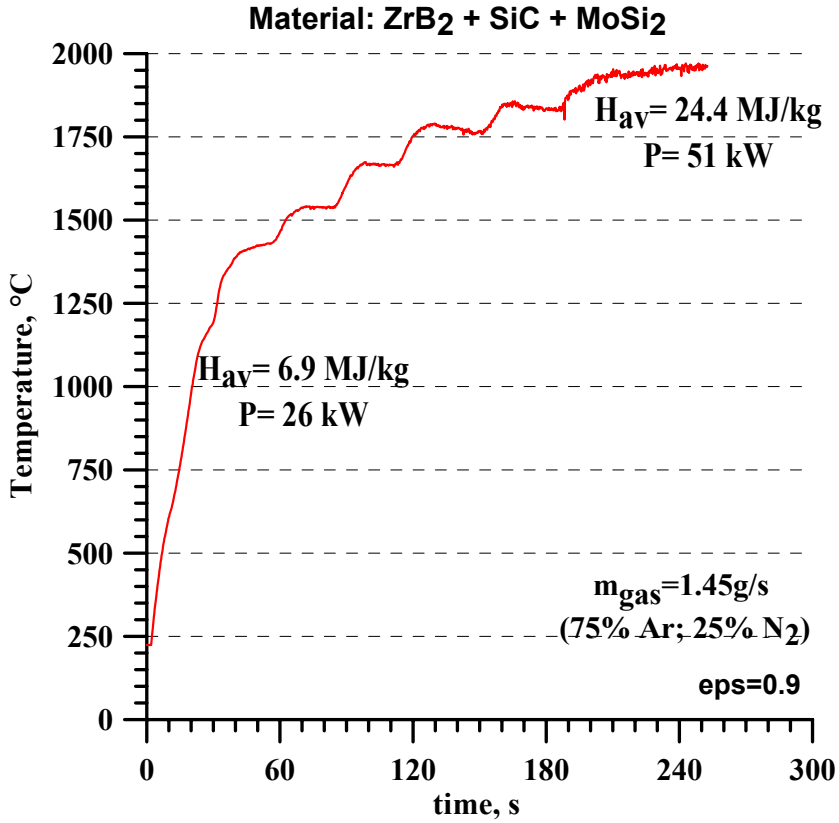

Figure 99 Time history temperature during experimental test


Figure 100 Specimen after the exposure to the flux

t = 120 s *t = 180 s*

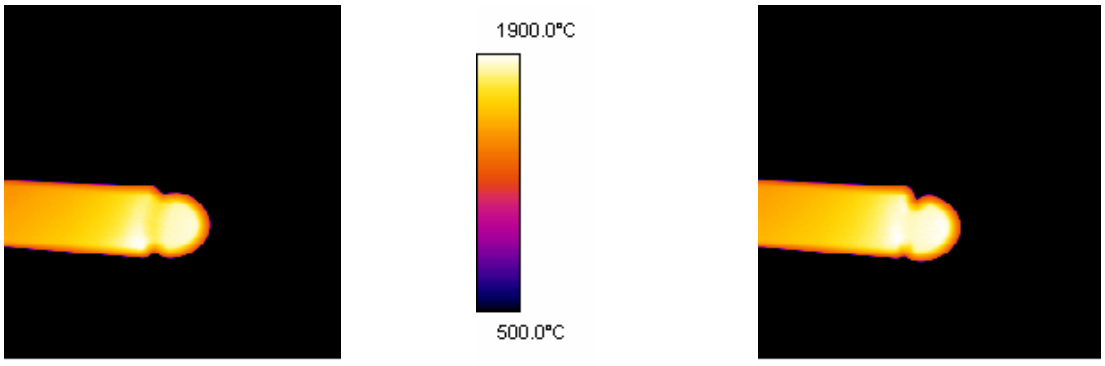

t = 210 s *t = 240 s*

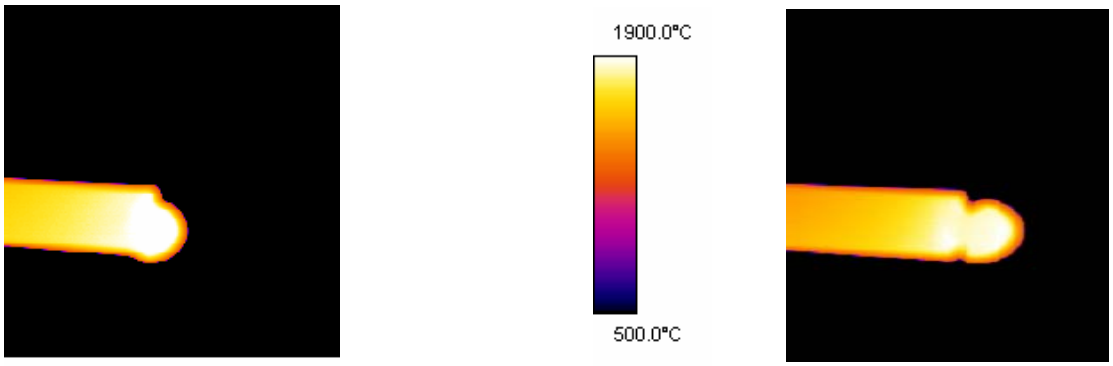

Figure 101 Infrared images of the UHTC specimen during the experimental test

14 Conclusions

The work was focused on the design of a structural element (Hot Structure), said Winglet, to study new UHTC materials for the space research program EXPERT in ESA.
In the frame of the EXPERT scientific program, the winglet was sized to realize the scientific aims, with respect to system requisitions. In particular, the interaction between P/L and metallic TPS of the capsule was analyzed, verifying the agreement with the admissible skin temperature value.
On-ground experimentation on UHTC materials allowed to determine a candidate for fly experimentation. In particular, ZrB2+SiC exhibit non catalytic behaviour and high emissivity.
In this experimental campaign, a new method to caracterize emissivity and surface catalicity properties of advanced ceramic materials (UHTC) was made, by means of experimental tests with a plasma torch and with infrared instruments. UHTC materials oxidization resistance was tested, in typical re-entry atmosphere (high oxygen dissociation at high temperatures). For the final results, see the following table which sum up the experimental tests.
A question should be further to investigate is the following: what relations between emissivity and surface oxidation? From the results of present discussion seems that the surface oxidation increase the emissivity of the material's surface, but more experimental tests are necessary to verify this idea.

Legenda:
FC = fully catalytic;
PC = partially catalytic;
NC = non catalytic

specimen shape	chemical composition	time duration (mm.ss)	ε stimata	cataliticità (1)
semisfera	ZrB_2 + 20%SiC	1.31	0.8	NC
conetto	ZrB_2	2.33	0.8	PC $\gamma_w=10^{-3}$
semisfera	tungsteno	0.20	0.8	PC $\gamma_w=10^{-3}$
semisfera	ZrB_2 + 20%SiC	1.00	0.95	NC
semisfera	ZrB_2 + 20%SiC	0.49	0.9	NC
semisfera	ZrB_2 + 20%SiC	0.20	0.9	NC
semisfera	ZrB_2 + 20%SiC	5.30	0.9	
semisfera	ZrB_2 + 20%SiC	1.50	0.9	
NOSE USV	ZrB_2 + SiC + $MoSi_2$	6.59	0.79	
semisfera	ZrB_2 + SiC + $MoSi_2$	4.22	0.9	

Appendix A: The Infrared Analysis

The electromagnetic spectrum

The electromagnetic spectrum (usually just spectrum) is the range of all possible electromagnetic radiation. The spectrum, shown in the Figure 102, extends from just below the frequencies used for modern radio (at the long-wavelength end) to gamma radiation (at the short-wavelength end), covering wavelengths from thousands of kilometres down to fractions of the size of an atom. In our universe the short wavelength limit is likely to be the Planck's length, and the long wavelength limit is the size of the universe itself, though in principle the spectrum is infinite. Note that there are no defined boundaries between the types of electromagnetic radiation. Some wavelengths have a mixture of the properties of two regions of the spectrum. For example, red light resembles infra-red radiation in that it can resonate some chemical bonds.
Nearly all objects in the universe emit, reflect and/or transmit some light. The distribution of this light along the electromagnetic spectrum (called the *spectrum of the object*) is determined by the object's composition. Several types of spectra can be distinguished depending upon the nature of the radiation coming from an object.

Infrared radiation

The infrared part of the electromagnetic spectrum covers the range from roughly 300 GHz (1 mm) to 400 THz (700 nm). It can be divided into three parts:

- **Far-infrared**, from 300 GHz (1 mm) to 30 THz (10 μm). The lower part of this range may also be called microwaves. This radiation is typically absorbed by so-called rotational modes in gas-phase molecules, by molecular motions in liquids, and by phonons in solids. The water in the Earth's atmosphere absorbs so strongly in this range that it renders the atmosphere effectively opaque.
- **Mid-infrared**, from 30 to 120 THz (10 to 2.5 μm). Hot objects (black-body radiators) can radiate strongly in this range. It is absorbed by molecular vibrations, that is, when the different atoms in a molecule vibrate around their equilibrium positions. This range is sometimes called the *fingerprint region* since the mid-infrared absorption spectrum of a compound is very specific for that compound.
- **Near-infrared**, from 120 to 400 THz (2500 to 700 nm). Physical processes that are relevant for this range are similar to those for visible light.

The divisions have been related to the transmission of the atmosphere for different types of applications.

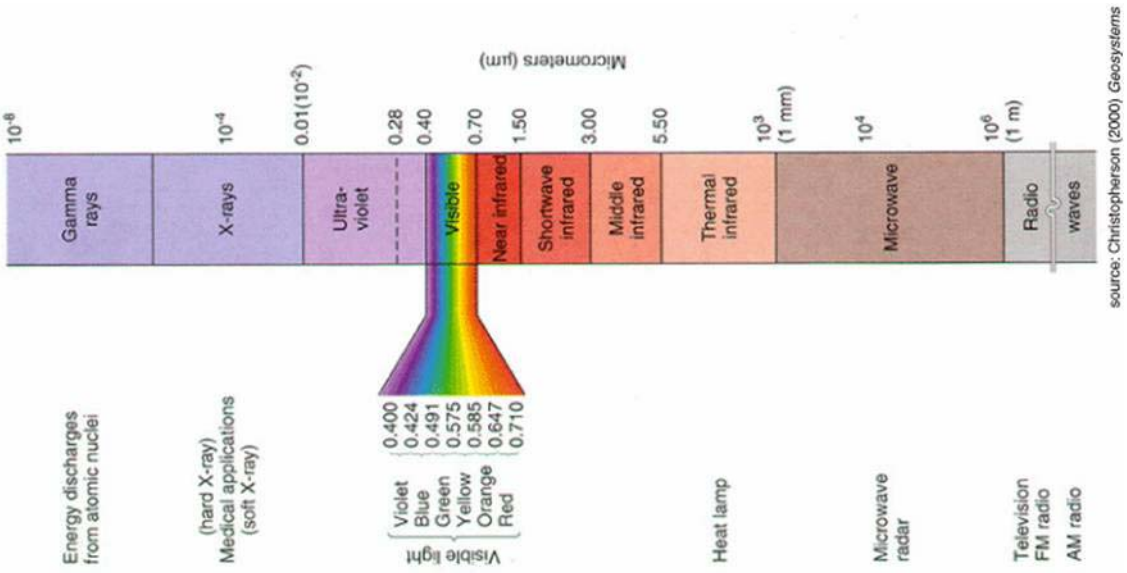

Figure 102 Electromagnetic spectrum

Although the thermal-infrared spectral region covers the range from approximately 3 to 100 μm, only the spectral intervals around 3.7 μm (3.5-4 μm) and between 8 and 14 μm are of interest. From general studies of radiation, we know that the atmosphere is moderately transparent to radiation only in these spectral regions, called "windows", whereas it is fairly opaque in the intervening wavelengths (see Figure 108).

Relationship among radiation, temperature, and surface emissivity

In remote sensing, we are concerned with interpreting measurements of radiation from a distant source. In the thermal infrared, we relate this measurement to the kinetic temperature (e.g., from a thermometer) of the radiating body, which initially is considered to be a perfect radiator or black body. Thus, the relationship between radiance and temperature is given by Plank's law.

$$I_{\lambda,T} = \frac{C_1}{\lambda^5 \left[\exp\left(\frac{C_2}{\lambda T}\right) - 1 \right]} \tag{6}$$

Where I is the spectral radiance [W m-2 mm-1], at wavelength l [mm], C_1 and C_2 are physical constant ($C_1 = 3.74\ 10^8$, $C_2 = 1.439\ 10^4$), and T, in degrees K, represents the physical temperature of the object. In practice, real objects are not ideal blackbodies, with the significance of the quality factor, emissivity, being discussed shortly.

For interpretation of remotely sensed data, we generally require the inverse function because the sensor measures radiance from which we derive the value of temperature implied by Plank's law. This inverse relationship is obtained by simple algebraic transformation of eq. 1. because real objects are not ideal blackbodies, it is customary to use subscripts to indicate apparent or radiance temperature as opposed to the actual temperature of the object.

As mentioned previously, there exist two atmospheric windows in the thermal infrared. These windows differ in the sense that by day, both radiated emitted from the Earth and reflected sunlight contribute significantly to radiation observed in the 3.7 μm window, whereas the contribution of reflected sunlight may be neglected compared to Earth radiation in the 8-14 μm window.

This ambiguity of reflected and emitted radiation could, in principle, be removed. Reflectance ρ is related to the quality factor for blackbodies, emissivity ε, by the general relation:

$$\rho_\lambda + \varepsilon_\lambda = 1 \qquad (7)$$

Before proceeding, we present the description of nonblackbody effects. The Planck formulation is an idealization of the true radiative properties of material, as the radiance of a body at kinetic temperature T is reduced by emissivity factor according to $E_\lambda = \varepsilon_\lambda I_\lambda$, where E is the measured radiance. Emissivity depends on the substance and varies with wavelength, ranging from approximately 0.5 to nearly 1.0 over the range of common materials and thermal-infrared wavelengths. In the 10-14 μm window, emissivity values are generally in the range 0.8 to 0.99, so that the following simplification is appropriate for many calculations.
One must distinguish between radiances measured at a particular wavelength and the total emitted radiant flux. The total radiant energy emitted by an object is found by integrating eq. 1 over wavelength. This leads to the Stefan-Boltzmann law, where the emissivity is the wavelength averaged value, $W_{emitted} = \varepsilon\sigma T^4$, and σ is the Stefan-Boltzmann constant (=5.67·10-8 [$Wm^{-2}K^{-4}$]).
However, emissivity is not constant with wavelength, so that in the analysis of thermal infrared data, we must take care to distinguish between the value of emissivity appropriate for energy calculations and the value that applies to radiometric measurements in the atmospheric windows.

Optic ownership of the materials

As already said, all objects emit, reflect and/or transmit some electromagnetic radiations. The so-called *spectrum* of the object is determined by the object's composition and by its superficial roughness.

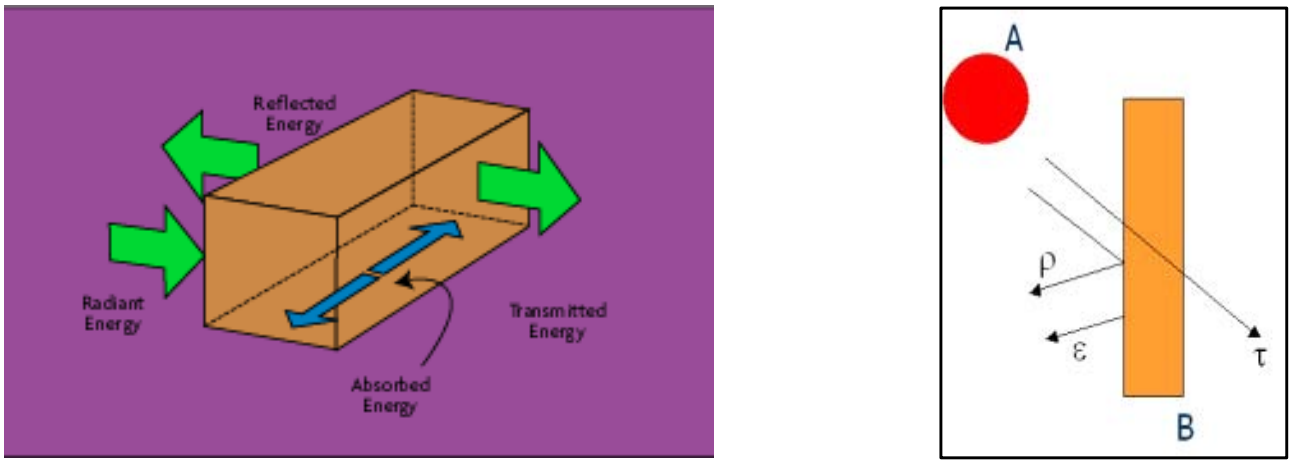

Figure 103 Optical ownership of the materials

The conservation energy principle for an object that emit, reflect and/or transmit, can be written in the following manner.
$E_i(\lambda) = E_r(\lambda) + E_a(\lambda) + E_t(\lambda)$
where, $E_i(\lambda)$ is incident energy, $E_r(\lambda)$ is reflected energy, $E_a(\lambda)$ and $E_t(\lambda)$ are absorbed and transmitted energy, respectively.
We define the following adimensional ratio that depends by composition and roughness of surface of the object.
$\rho = E_r/E_i$ reflected coefficient
$\tau = E_t/E_i$ transmitted coefficient
$\alpha = E_a/E_i$ absorbed coefficient
They are function of wavelength and temperature and they are between 0 and 1 for the conservation principle of energy, just. Hence, the conservation energy principle can be written now as following

$$\rho + \tau + \alpha = 1 \qquad (8)$$

If the object is at a constant temperature, then the rate at which it emits energy must equal the rate at which it absorbs energy, otherwise the object would cool (emittance greater than absorption), or warm (emittance less than absorption).

Black-body: definition

The concept of the blackbody: surface that neither reflects nor transmits, but absorbs all incident radiation, independent of direction and wavelength. The fraction of radiation absorbed by a real body is called absorptivity, and it is 1 for an ideal blackbody. For non-blackbodies, the absorption is a fraction of the radiation heat transfer incident on a surface. In addition to absorbing all incident radiation, a blackbody is a perfect radiating body. To describe the emitting capabilities of a surface in comparison to a blackbody, Kirchoff defined *emissivity* ε of a real surface as the ratio of the thermal radiation emitted by a surface at a given temperature to that of a blackbody at the same temperature and for the same spectral and directional conditions. This value also must be considered by a non-contact temperature sensor when taking a temperature measurement. The total emissivity for a real surface is the ratio of the total amount of radiation emitted by a surface in comparison to a blackbody at the same temperature. If precise temperature measurements are required, the surface's actual emissivity value should be obtained (see Figure 104).

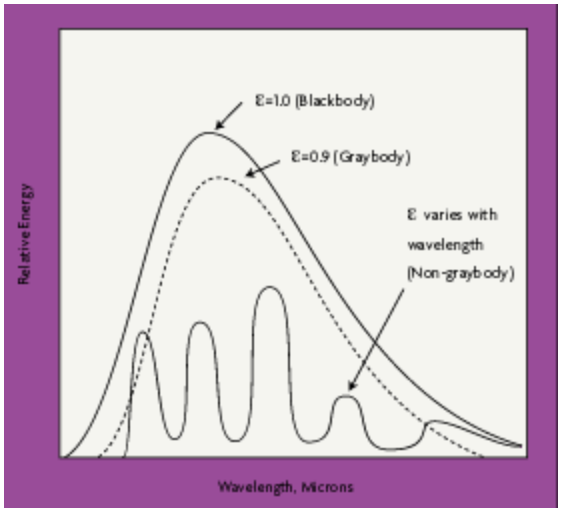

Figure 104 Emissivity varying with wavelength

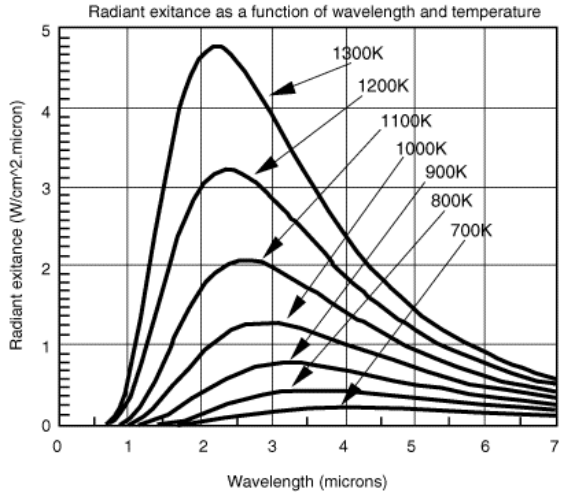

Figure 105 Blackbody spectral distribution

Although some surfaces come close to blackbody performance, all real objects and surfaces have emissivity less than 1. Non-blackbody objects are either grey-bodies, whose emissivity doesn't vary with wavelength, or non-grey-bodies, whose emissivity varies with wavelength, as shown in Figure 104. The closest approximation to a blackbody is a cavity with an interior surface at a uniform temperature T_s, which communicates with the surroundings by a small hole having a diameter small in comparison to the dimensions of the cavity. Most of the radiation entering the opening is either absorbed or reflected within the cavity (to ultimately be absorbed), while negligible radiation exits the aperture. The body approximates a perfect absorber, independent of the cavity's surface properties. The radiation trapped within the interior of the cavity is absorbed and reflected so that the radiation within the cavity is equally distributed.

The spectral characteristics of blackbody radiation are function of temperature and wavelength, referred to as the Planck distribution law, is:

$$I_{\lambda,T} = \frac{C_1}{\lambda^5\left[\exp\left(\frac{C_2}{\lambda T}\right)-1\right]} \qquad (9)$$

where $C1=2hc_0^2= 3.742\ 10^{-16}$ [W/m^2] and $C_2=hc_0/k=1.439\ 10^{-2}$ [m K].

Planck's distribution shows that as wavelength varies, emitted radiation varies continuously. As temperature increases, the total amount of energy emitted increases and the peak of the curve shifts to the left, or toward the shorter wavelengths. In considering the electromagnetic spectrum, it is apparent that bodies with very high temperatures emit energy in the visible spectrum as wavelength decreases, as shown in Figure 106.

Figure 105 shows that there is more energy difference per degree at shorter wavelengths. From Figure 105, the blackbody spectral distribution has a maximum wavelength value, l_{max}, which depends on the temperature. The dashed line locates the maximum radiation values for each temperature, at a specific wavelength. Notice that maximum radiance is associated with higher temperatures and lower wavelengths. The spectral radiance maximum peak of the black body, while temperature increasing, rises and shifts towards less wavelengths, more and more close to visible light.

The spectral emissivity

The spectral hemispherical emissive power is defined as the rate at which radiation is emitted per unit area at all possible wavelengths and in all possible directions from a surface, per unit wavelength and per unit surface area. Although the directional distribution of surface emission varies depends on the surface itself, many surfaces approximate diffuse emitters. That is, the intensity of emitted radiation is independent of the direction in which the energy is incident or emitted. In this case, the total, hemispherical (spectral) emissive power $E_\lambda(\lambda)$ [W/m^2] is defined as:

$$E_\lambda = \pi I_{\lambda,e}(\lambda) \qquad (10)$$

where I_e is the total intensity of the emitted radiation, or the rate at which radiant energy is emitted at a specific wavelength, per unit area of the emitting surface normal to the direction, per unit solid angle about this direction, and per unit wavelength. Notice that E_λ is a flux based on the actual surface area, where $I_{\lambda e}$ is based on the projected area. In approximating a blackbody, the radiation is almost entirely absorbed by the cavity. Any radiation that exits the cavity is due to the surface temperature only.

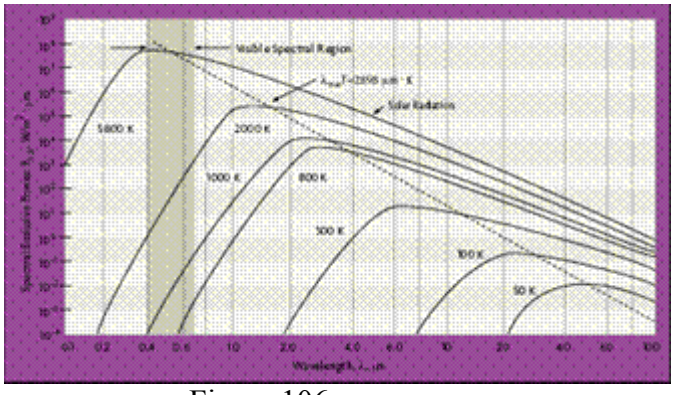

Figure 106

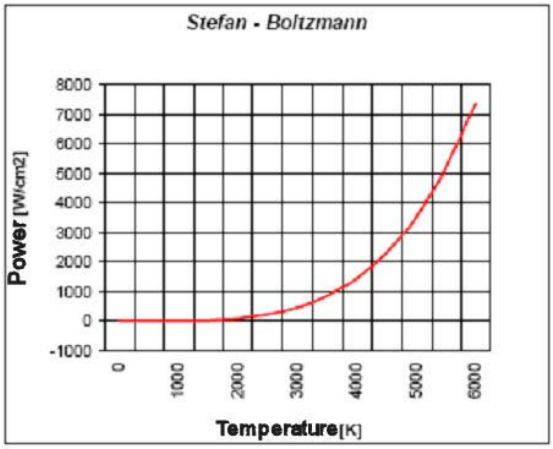

Figure 107

The Planck's law and Stephan-Boltzmann's law, for non-black body are:

$$I_{\lambda,T} = \frac{\varepsilon_{\lambda,T} C_1}{\lambda^5 \left[\exp\left(\frac{C_2}{\lambda T} \right) - 1 \right]} \tag{11}$$

$$W = \int_0^\infty I_{\lambda,T} d\lambda = \varepsilon_T \sigma T^4 \tag{12}$$

where εT is average emissivity, weighted with black body radiances on the whole spectrum at the temperature T.

Relation between temperature and thermal radiation

All matter constantly exchanges thermal energy in the form of electromagnetic radiation with its surroundings. If there is a temperature difference between the object and its surroundings, there will be a net energy transfer in the form of heat. The topic of this volume, radiation thermometry, or more generally, non-contact temperature measurement, involves taking advantage of this radiation dependence on temperature to measure the temperature of objects and masses without the need for direct contact.
The magnitude of radiation at any wavelength as well as the spectral distribution varies with the properties and temperature of the emitting surface. Radiation is also directional. A surface may prefer a particular direction to radiate energy. Both spectral and directional distribution must be considered in studying radiation. Non-contact temperature sensors work in the infrared portion of the spectrum.

Thermography

Thermography, or *thermal imaging*, is a type of infrared imaging. Thermographic cameras, also said *infrared camera*, detect radiation in the infrared range of the electromagnetic spectrum and produce images of that radiation. Since infrared radiation is emitted by all objects based on their temperature, according to the black body radiation law, thermography makes it possible to "see" one's environment with or without visible illumination. The amount of radiation emitted by an object increases with temperature, therefore thermography allows one to see variations in temperature, hence the name. With a thermographic camera warm objects stand out well against cooler backgrounds.

Thermography main advantages

The thermal imaging main advantages are the following.

c. it allows a non invasive measures;
d. it allows temperature measures on moving object;
e. it doesn't influence measures of the temperature;
f. it allows the measures of the temperature on object difficult to reach because placed in closed test chamber;
g. it allows to effect measures on conductor objects without the risk of short-circuits.

Error sources in thermal imaging

The properties of the material at various temperatures must also be considered. Changes in process material emissivity, radiation from other sources, and losses in radiation due to dirt, dust, smoke, or atmospheric absorption can introduce errors.
As often as not, measure errors depend on external factors. We consider some example of error sources.

- Sunlight or artificial light or another source of infrared radiation can affect the measure of infrared radiation coming from the target, if proper filters aren't used, i.e. filters just able to eliminate improper wavelengths for the measure.
- A typical example of interference is constituted by hot objects near the target. The infrared radiation emitted by the "disturbing" object can be reflected by the target surface, hence the instruments detects an higher radiation.
- In the presence of filters, for example protective glasses of the sensor, an appropriate transmitted spectrum should be take into account when carrying out measure.
- If the measure is carried out using a window, the emissivity coefficient has to be modified to compensate the loss of absorbed radiation; it's the same in the presence of smoke, hanging particles or water vapour.

The atmosphere has a typical transmitted spectrum shown in Figure 108. The termographic instruments work at specific wavelenghts bands in which the absorption made by atmosphere can be neglected.

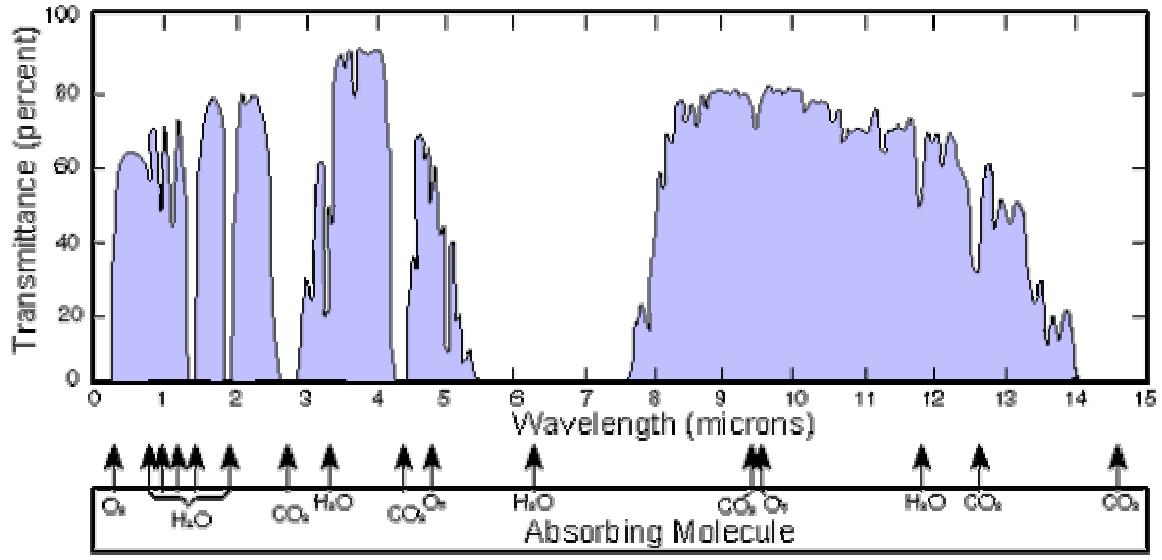

Figure 108 the typical atmosphere's transmitted spectrum

Appendix B: Numerical Model

Working fluid model

All of the numerical simulations were carried out using a viscous model both bi-dimensional (axisymmetric) and three dimensional geometries and steady/unsteady model. The working fluid is considered as a five species mixture (O2, N_2, NO, O, N).

Thermodynamic model

For a chemically reacting mixture of five perfect gases, the pressure of the mixture is given by Dalton's law of partial pressures:

$$p = \sum_i p_i \tag{13}$$

where p_i is the pressure of species i and p is the pressure of the mixture, where the summation is taken over all species of the mixture.

In addition, using the perfect gas equation of state, we obtain the partial pressure in terms of density and temperature of the mixture:

$$p_i = \rho_i R_i T = \rho \alpha_i R_i T \tag{14}$$

where ρ is the density of the mixture, T is the temperature of the mixture, α_i is the mass fraction of the species i and R_i states the ratio between the molecular weight of the species i and the universal gas constant R_0 = 8314 J/Kg K).

Combining equations (13)and (14), we have:

$$\rho = \frac{p}{R_0 T \sum_i \frac{\alpha_i}{M_i}} \tag{15}$$

The sensible enthalpy of the species *i* per unit mass of *i*, is given by:

$$h_i = \int_0^T c_{pi}(T)dT + \left(\Delta h_f\right)_i^0$$

where $(\Delta h)_i$ is the heat of formation of the species i.

The sensible enthalpy of the mixture per unit mass is given by:

$$h = \sum_i \alpha_i h_i$$

Table 8 shows the heat of formation for the chemical species considered in the mixture.

Species	$(\Delta h_f)^0$ [J /kmole]
O_2	0
O	$2.4918*10^8$
N_2	0
N	$4.7096*10^8$
NO	$9.029*10^7$

Table 8 Heats of formation for the chemical species considered in the mixture

To evaluate the heat of formation per mole of species *i*, the polynomial law was employed.
The specific heat at constant pressure of the mixture is given by:

$$c_p = \sum_i \alpha_i c_{pi} \tag{16}$$

To evaluate the specific heat at constant pressure of the species *i*, the polynomial law was employed.
Species viscosities, thermal conductivity and mass diffusivity are given by the kinetic theory of gases in terms of the Lennard-Jones parameters:

$$\mu_i = 2.6693 \cdot 10^{-6} \cdot \frac{\sqrt{M_i T}}{\sigma_i^2 \Omega_{\mu i}} \tag{17}$$

$$\lambda_i = \frac{15}{4}\frac{R}{M_i}\mu_i\left[\frac{4}{15}\frac{c_p M_i}{R} + \frac{1}{3}\right] \tag{18}$$

$$D_{i,j} = 0.0188 \frac{\left[T^3\left(\frac{1}{M_i} + \frac{1}{M_j}\right)\right]^{\frac{1}{2}}}{p\sigma_{ij}^2 \Omega_D} \tag{19}$$

where M_i is the molecular weight of species i, σ_i is the molecular diameter in angstrom, ε_i/k is a reference temperature, Ω is the collision integral (see Table 9).

For a chemically reacting gas, the mixture values of viscosity μ and thermal conductivity k must be found from the values of μ_i and k_i of each of the chemical species *i* by means of mixture rules. A common mixture rule for viscosity is Wilke's rule, which state that:

$$\mu = \sum_{i=1}^{n} \frac{X_i \mu_i}{\sum_{j=1}^{n} X_i \phi_{ij}}; \qquad \lambda = \sum_{i=1}^{n} \frac{X_i \lambda_i}{\sum_{j=1}^{n} X_i \phi_{ij}} \tag{20}$$

where

$$\phi_{ij} = \frac{\left[1+\left(\frac{\mu_i}{\mu_j}\right)^{1/2}\left(\frac{M_j}{M_i}\right)^{1/4}\right]^2}{\left[8\left(1+\frac{M_i}{M_j}\right)\right]^{1/2}} \tag{21}$$

and X_i is mass fraction of the species i.

The multicomponent diffusion coefficient D_i in the mixture is related to the binary diffusion coefficient for the diffusion of the species *i* into species *j* by means of the approximate expression:

$$D_i = \frac{1-X_i}{\sum_j \frac{X_j}{D_{i,j}}} \tag{22}$$

Species	σ_i [Å]	ε_i / k [K]
O	**2.75**	**80**
O_2	**3.458**	**107.4**
N	**3.298**	**71.4**
N_2	**3.681**	**91.5**
NO	**3.47**	**119**

Table 9 Lennard – Jones parameters

Fluid dynamic equations

The equations of the fluid dynamics considered are the continuity equation, the transport equations of the mass of the species *i*, of momentum and of energy.
The transport equation of the species *i* is:

$$\frac{\partial(\rho\alpha_i)}{\partial t} + \underline{\nabla}\cdot\left(\rho\underline{V}\alpha_i\right) + \underline{\nabla}\cdot J_i = \dot{\omega}_i \tag{23}$$

where:

- $J_i = -\rho D_i \underline{\nabla}\alpha_i$ is the diffusive flux of the species *i*, according to the Fick's law.
- $\dot{\omega}_i$ is the production of the species *i*.

Since:

$$\sum_i \alpha_i = 1$$

$$\sum_i J_i = \sum_i \dot{\omega}_i = 0 \tag{24}$$

From the equations (16) and 17) we obtain the continuity equation of the whole mixture:

$$\frac{\partial \rho}{\partial t} + \underline{\nabla} \cdot (\rho \underline{V}) = 0 \tag{25}$$

The transport equation of momentum is:

$$\frac{\partial (\rho \underline{V})}{\partial t} + \underline{\nabla} \cdot (\rho \underline{V}\underline{V}) + \underline{\nabla} p = \underline{\nabla} \cdot [\underline{\underline{\tau}}_d] \tag{26}$$

The transport equation of energy is:

$$\frac{\partial (\rho E)}{\partial t} + \underline{\nabla} \cdot [(\rho E + p)\underline{V}] = \underline{\nabla} \cdot \left(\underline{\underline{\tau}}_d \cdot \underline{V} - \underline{J}_q - \sum_i h_i \underline{J}_i \right) - \sum_i h_i \dot{\omega}_i \tag{27}$$

Chemically reacting gas
The general equation of the chemical kinetic:

$$\frac{d[X_i]}{dt} = (\nu''_i - \nu'_i) \cdot \left[K_f \prod_i [X_i]^{\nu'_i} - K_b \prod_i [X_i]^{\nu''_i} \right] \tag{28}$$

Let us consider k reactions involving the i chemical species. They can be written in the following general manner:

$$\sum_{i=1}^{I} \nu'_{ik} s_i \Leftrightarrow \sum_{i=1}^{I} \nu''_{ik} s_i \tag{29}$$

where i is the generic species and ν_{ik} are the stoichiometric coefficients of reagent and product species, respectively.

The production of the species *i* in the k^{th} reaction is given by:

$$\dot{\omega}_{ik} = \Gamma \cdot (\nu''_{ik}{}' - \nu'_{ik}) \cdot \left[K_{fk} \prod_j C_j^{\nu'_{jk}} - K_{bk} \prod_j C_j^{\nu''_{jk}{}'} \right] \tag{30}$$

where there is the molar concentration of the species, K_{fk} and K_{bk} are the forward and backward reaction rates respectively, for the k^{th} reaction, and Γ is the third body efficiency, calculated as:

$$\Gamma = \sum_i \gamma_{ik} C_i \tag{31}$$

The forward reaction rate constant of each elementary kinetic process is specified by the Arrhenius law as:

$$K_k = A_K T^{\beta_K} \exp\left(-\frac{E_k}{R_o T} \right) \tag{32}$$

The pre-exponential A_k, the temperature exponent β_k and the activation energy of the k^{th} process E_k are showed in the following table (Park 1989):

Reazione	A_k	E_k [J/Kg·mol]	β_k
$O_2 \rightarrow 2O$	$3.61 \cdot 10^{15}$	$4.938 \cdot 10^{8}$	-1.0
$N_2 \rightarrow 2N$	$1.92 \cdot 10^{14}$	$9.403 \cdot 10^{8}$	-0.5
$N_2+N \rightarrow 3N$	$4.15 \cdot 10^{19}$	$9.403 \cdot 10^{8}$	-1.5
$NO \rightarrow N+O$	$3.97 \cdot 10^{17}$	$6.285 \cdot 10^{8}$	-1.5
$NO+O \rightarrow O_2+N$	$3.18 \cdot 10^{06}$	$1.638 \cdot 10^{8}$	1.0
$N_2+O \rightarrow NO+N$	$6.75 \cdot 10^{10}$	$3.118 \cdot 10^{8}$	0.0

Table 10 Park's model coefficients

The backward reaction rate is computed from the forward reaction rate using the following relation:

$$K_{bk} = \frac{K_{fk}}{K_k^{eq}} \tag{33}$$

The equilibrium constant K_k^{eq} for the chemical reaction is given by:

$$K_k^{eq} = \left(\frac{p_{atm}}{R_0 T} \right)^{\sum_{i=1}^{I} (\nu''_{ik} - \nu'_{ik})} \exp\left(\frac{\Delta S_k^0}{R_0} - \frac{\Delta H_k^0}{R_0 T} \right) \tag{34}$$

where p_{atm} is the atmospheric pressure in atm and ΔS_k^0, ΔH_k^0 are the entropy and enthalpy variation due to chemical reaction, respectively.

The production term in eq (16), due to the considered chemical reactions inside the control volume, can be written as:

$$\dot{\omega}_i = M_i \sum_k \dot{\omega}_{ik} \tag{35}$$

The governing flow equations

Hence, we have *i*+4 physical variables:

2. Mass fractions of the *i* species considered in the mixture, or, the same way, mass fractions of *i-1* species of and density of the mixture, since *i* unknowns.
3. Speed.
4. Pressure.
5. Enthalpy.
6. Temperature.
7. Vibrational energy

To calculate unknown variables, we need *i+4* equations:

1. Transport equations of *i* chemical species, or, the same way, *i-1* among them and the continuity equation.
2. Transport equation of momentum.
3. Transport equation of energy.

4. Equations of state.
5. Vibrational energy balance
6. Transport equation of enthalpy.

The system is well-posed if we assign the right boundary conditions.

Boundary conditions for reacting chemically flow

The *far-field* conditions are assigned by equilibrium values mass fraction of the species at considered altitude. At the wall, the boundary condition on c_i involves, in general, a surface chemistry interaction with the gas at the wall. The wall may be made of a material that tends to catalyze chemical reactions right at the surface: such surfaces are called *catalytic walls*. This leads to the following definitions:

$$\left(\frac{\partial c_i}{\partial n}\right)_W = 0 \qquad \textit{non catalytic wall}$$

$$\rho D\left(\frac{\partial c_i}{\partial n}\right)_W = \rho K_w\left(c_i - c_{eq}\right) \qquad \textit{partially catalytic wall}$$

$$c_i = (c_i)_{equil} \qquad \textit{fully catalytic wall}$$

The partially catalytic boundary condition has been set by means of superficial re-combination coefficient K_w:

$$K_{ws} = \gamma\sqrt{RT_w/(2\pi M_s)} \qquad (36)$$

where R is the universal constant of gas, T_w is surface's temperature, M_s is atomic mass of the species s. The K_w values are corresponding to γ_w values in the range between $5\cdot10^{-2}$ and 10^{-3}, for both atomic oxygen and nitrogen. The fully catalytic boundary condition has been set with atomic species at equilibrium values. The ionization effects have been neglected because they aren't active by the considered energy. Moreover, at the same altitude, heat flux is not affect by the thermal non-equilibrium effects, because the vibrational and translational temperatures tend towards the equilibrium near the wall. For this reason, a model with an unique temperature value has been considered. At the edge of the boundary layer, thermal and chemical equilibrium is assumed, therefore, a single equilibrium temperature T_e is introduced to described translational and internal degrees of freedom. Vibrational level populations follow the Boltzmann distribution with temperature T_e. The gas temperature near the surface is assumed to be equal to the wall temperature T_w. The boundary condition on the surface is the local radiative equilibrium. This condition sets the balance between incident convective heat flux and radiated heat

flux. In this case, in the locally radiative equilibrium there is an energy transport due to diffusion of chemical species i:

$$\sigma\varepsilon T_w^4 = -\lambda\left(\frac{\partial T}{\partial n}\right) - \rho\sum_i D_i h_i \frac{\partial c_i}{\partial n} \tag{37}$$

where λ is air thermal conductivity, T_w is surface's temperature, ε and σ are emissivity coefficient and Stefan-Boltzmann's constant, respectively.

By means of relation (27), we calculate the body's temperature due to the heat conduction.

Numerical simulations: used materials' properties

Material	ρ [Kg/m^3]	C_p [J/Kg K]	k [w/m K]
UHTC	**6000**	**628**	**66**
Tungsten	**19300**	**130**	**174**
Allumina	**3900**	**880**	**30**
Graphite	**1730**	**600**	**90**

Table 11 Materials' properties

Appendix C: Characteristic's materials

Massive ZrB2-SiC

Properties	Massive ZrB_2 + SiC	
Density (kg/m^3):	5610	
Porosity (%)	< 1	
Permeability (cm^2/sec)		
Thermal Conductivity (W/m K):	103.8 @300 K [3] 83.07 @900 K [3] 76.15 @1500K[3] 69.23 @2100 K [3] 67.50 @2400 K [3]	
Specific Heat (kJ/kg-K):	T (K)	C_P (J/g/K)
	298 300 400 500 600 700 800 900 1000 1100 1200 1300 1400 1500 1600 1700 1800 1900 2000 2100 2200	0.459 0.462 0.554 0.603 0.633 0.656 0.673 0.687 0.699 0.711 0.721 0.731 0.741 0.750 0.759 0.768 0.776 0.785 0.794 0.802 0.811
Total Hemispherical Emissivity:[5]	T(K)	Emissivity
	1037 1169 1263 1334 1485 1681 1842	0.775 0.712 0.72 0.734 0.748 0.724 0.663
Mult.Use Temperature Limit (°C):	2015.889	
Single Use Temperature Limit (°C):	2587.556	
Eutectic Temperature Limit (°C):	2207.556	

Melt Temperature (°C):	**2747.556**
Vickers HardnessHV_{1-0} (Gpa)	**17.7(0.4 7**
Fracture Toughness KIC (MPa*$m^{1/2}$)	**4.07±0.03 @ RT** **2.53±0.23 @1500°C**
Young Modulus	**480±4 9**
Tensile Modulus (GPa):	**Idem**
Tensile Strength (MPa)	**491 @R.T.** **610 @800°C** **561 @1000°C** **226 @1200°C**
Compressive Strength (MPa):	**3.447E+03**
Compressive Modulus (Gpa)	
Flexural Strength (MPa):	**887+125 @R.T.** **255+24 @1500°C**
Flexural Modulus (Gpa)	**Idem**
Poisson's Ratio:	**0.13**
CTE (cm/cm K):	**6.67E-06 @ 800°C** **6.79E-06 @900°C** **6.95 E-06 @1000°C** **7.02 E-06 @1100°C** **7.01 E-06 @1200°C** **7.11 E-06 @1300°C**
Electrical resistivity (/jQcm)	**16.0**

Table 12 Massive ZrB_2-SiC properties

Super alloy PM1000

Temp [C]	Sig yld [MPa]	Sig ult [MPa]	E-modulus [GPa]	nu [-]	Exp. Coef. [10^-6/K]
0	545	832	186	0.30	12.8
20	535	825	185	0.30	12.9
50	521	814	183	0.30	13.0
100	497	795	180	0.30	13.2
200	455	753	175	0.30	13.7
300	408	705	169	0.30	14.1
400	365	643	164	0.30	14.5
500	320	557	158	0.30	14.9
600	273	421	153	0.30	15.3
700	234	311	145	0.30	15.8
800	194	230	137	0.30	16.2
900	143	161	128	0.30	16.6
1000	122	131	119	0.30	17.0
1100	82	90	109	0.30	17.5
1200	69	72	99	0.30	17.9
1300	59	62	88	0.30	18.3
1350	54	57	83	0.30	18.5

Table 13 Super alloy PM1000

Temp [C]	Density [10^3*kg/m^3]	Heat cap. [J/kg/K]	Therm. cond. [W/m/K]	Emissivity [-]
0	8.24	432	11.5	0.60
20	8.24	440	12.0	0.61
50	8.24	451	12.8	0.61
100	8.24	471	14.0	0.63
200	8.24	509	16.6	0.65
300	8.24	547	19.1	0.68
400	8.24	585	21.7	0.70
500	8.24	623	24.2	0.73
600	8.24	661	26.7	0.76
700	8.24	699	29.3	0.79
800	8.24	737	31.8	0.82
900	8.24	776	34.4	0.84
1000	8.24	814	36.9	0.85
1100	8.24	852	39.5	0.87
1200	8.24	890	42.0	0.88
1300	8.24	928	44.5	0.90
1350	8.24	947	45.8	0.90

Table 14 Super alloy PM1000

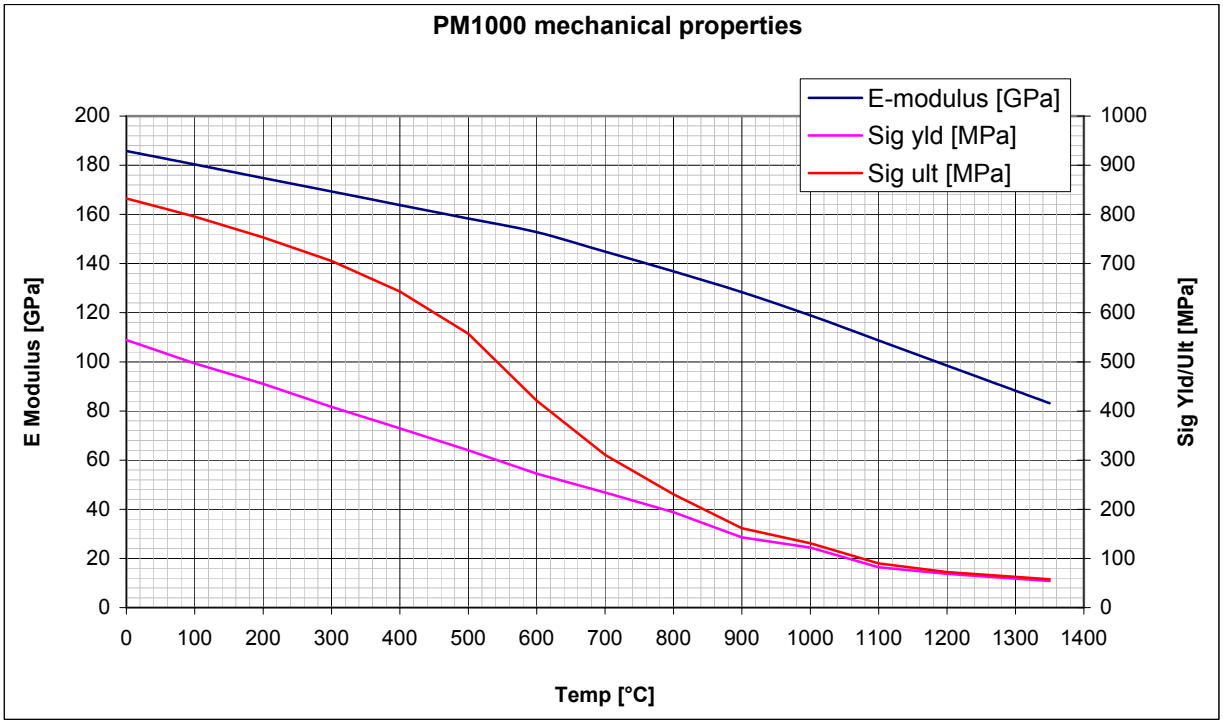

Figure 109 Materials' properties

INCONEL alloy 617

ρ [Kg/m^3]	Melting Range [°C]	Specific Heat at 26°C [J/kg °C]	Electrical Resistivity at 26°C [μΩ m]
8.36	1332-1380	419	1.22

table 15 Physical Constants

Temperature [°C]	Electrical Resistivity [μΩ m]	Thermal Conductivity [W/m °C]	Coefficient of Expansion [μm/m °C]	Specific Heat [J/kg °C]
20	1.222	13.4	-	419
100	1.245	14.7	11.6	440
200	1.258	16.3	12.6	465
300	1.268	17.7	13.1	490
400	1.278	19.3	13.6	515
500	1.290	20.9	13.9	536
600	1.308	22.5	14.0	561
700	1.332	23.9	14.8	586
800	1.342	25.5	15.4	611
900	1.338	27.1	15.8	636
1000	1.378	28.7	16.3	662

table 16 Electrical and Thermal Properties

Temperature [°C]	Tensile Modulus [GPa]	Shear Modulus [GPa]	Poisson's Ratio[b]
25	211	81	0.30
100	206	80	0.30
200	201	77	0.30
300	194	75	0.30
400	188	72	0.30
500	181	70	0.30
600	173	66	0.30
700	166	64	0.30
800	157	61	0.30
900	149	57	0.30
1000	139	53	0.31
1100	129	49	0.32

table 17 Modulus of Elasticity

Exposure Temperature [°C]	Exposure Time, h	Yield Strength (0.2% Offset) [MPa]	Tensile Strength [MPa]	Elongation, %	Impact Strength [J]
No exposure		319	769	68	232
595	100	321	769	69	289
	1 000	357	803	67	302
	4 000	384	810	67	245
	8 000	410	838	61	133
	12 000	466	910	34	94
650	100	357	789	69	259
	1 000	459	920	37	47
	3 640	526	979	33	47
	8 000	527	993	28	54

	12 000	534	993	32	52
705	100	405	872	38	77
	1 000	486	952	33	65
	4 000	487	952	36	65
760	100	402	872	35	76
	1 000	388	879	37	85
	4 000	401	886	38	84
	8 000	403	896	40	87
	12 000	389	893	38	91

table 18 Mechanical Properties After Exposure to Elevated Temperatures

Bibliography

1. D. Paterna, R. Monti, R.Savino, A. Esposito, *Experimental and Numerical Investigation of Martian Atmosphere Entry*, Journal of Spacecraft and Rockets, Vol. 38, N.6, pp. 1-10, 2001.

2. R. Monti, A. Esposito, D. Paterna, *Low Catalycity Coating for Planetary Entry Thermal Protection Systems,* Proceedings of the Workshop "Materiali per lo spazio: sintesi, metodologie, tecnologie", Bonassola, 7-8 Giugno 2001.

3. D. Paterna, R. Monti, A. Esposito, R. Savino, R. Renis, *Numerical and Experimental Analysis of Surface Catalytic Effects for Martian Atmosphere Entry*, Proceedings of the IV European Symposium on Aerothermodynamics for Space Vehicles, ESA SP-487, 15-18 October 2001.

4. R. Monti, G. Pezzella, R. Savino, D. Paterna, A. Esposito, *Aerothermodynamic Study of an Advanced Thermal Protection System*, Proceedings of the 4th European Workshop on Hot Structures and Thermal Protection Systems for Space Vehicles, Palermo, 26-29 Novembre 2002, ESA SP-251, Aprile 2003.

5. R. Savino, M. De Stefano Fumo, D. Paterna, M. Serpico, *Aerothermodynamic Study of UHTC-based Thermal Protection Systems*, Aerospace Science and Technology, Volume 9, Issue 2, March 2005, Pages 151-160.

6. F. De Filippis, R. Savino, A. Martucci, *Numerical-Experimental correlation of stagnation point heat flux in high enthalpy hypersonic wind tunnel*, 13th AIAA/CIRA International Space Plane and Hypersonic Systems and Technologies Conference, Capua, 16-20 Maggio 2005

7. R.B. Pope, *Stagnation-Point Convective Heat Transfer in Frozen Boundary Layers*. AIAA Journal, Vol. 6, No. 4, April 1968.

8. J.C. Greaves and J.W. Linnett. *Recombination of Atoms at Surfaces. Part 5. Oxigen Atoms at Oxide Surfaces*. Trans. Faraday Soc., 1959, 55, 1346.

9. P.G. Dickens and M. B. Sutcliffe. *Recombination of Oxigen Atoms on Oxide Surfaces. Part 1. Activation Energies of Recombination*. Trans. Faraday Soc., 1964, 60, 1272.

10. W.L. Wolfe, G.J. Zissis, *The Infrared Handbook*. Environmental Research Institute of Michigan,1978.

11. F. De Filippis, M. Serpico, *Air High-Enthalpy Stagnation Point Heat Flux Calculation*. J.Thermophysics, vol.12, No.4: Technical Notes, pp. 608-610

12. M. Serpico, R. Monti, and R.Savino, *Heat Flux on Partially Catalytic Surfaces in Hypersonic Flows*. Journal of Spacecraft and Rockets, Vol. 35, N.1, 1998, pp. 9-15.

13. J.A. Fay, and F.R. Riddel, Theory of Stagnation Point Heat Transfer in Dissociated Air, Journal of the Aeronautical Sciences, Vol. 25, No. 2, 1992, pp.73-85.

14. S. Pidan, M. Auweter-Kurtz, G. Herdrich, M. Fertig, Determination of Recombination Coefficients and Spectral Emisivity of Thermal Protection Materials, 37th AIAA Thermophysics Conference, AIAA-2004-2274.

15. R.E. Jahn, Temperature Distribution and Thermal Efficiency of Low Power Arc-heated Plasma Jets, BRIT. J. APPL. PHYS., 1963, VOL. 14.

16. J.J. Bertin, Hypersonic Aerothermodynamics, AIAA Education Series, J. S. Przemieniecki Series Editor-in-chief, 1994, pp. 373-405.

17. J.D. Anderson, Hypersonic and High Temperature Gas Dynamics, AIAA, Reston, Virginia, 2000.

18. J.D. Anderson, Computational Fluid Dynamics: The Basics with Applications, McGraw-Hill, New York, 1995

19. C. Hirsch, Numerical Computation of Internal and External Flows, vols. 1 and 2, J. Wiley and Sons, Chichester 1988.

20. B.S. Baldwin and H. Lomax, Thin Layer Approximation and Algebraic Model for Separated Turbulent Flows, AIAA paper No. 78-257, Jan. 1978.

21. J.H. Ferziger and M. Peric, Computational Methods for Fluid Dynamics, 3rd Ed., Springer.

22. R. Monti, G. Zuppardi, Lezioni di Aerodinamica Ipersonica, Liguori, 2002.

23. IMPAC INFRARED GmbH, "Infrared Temperature Measurement".

24. ThermCAM™ Researcher 2001 Operating Manual.

25. Fluent 6.2 User's Guide", Fluent Inc., Lebanon, NH, 2004.

26. J.F. Shackelford – "Material Science for Engineers" - McGraw-Hill - 1992.

27. C. Park, *Review of Chemical Kinetics Problems for future NASA Mission Part1: Earth Entries*, Journal of Thermophysics and Heat Transfer, Vol.7, No.3, 1993, pp 385.398.

28. P. Bradshaw, T. Cebeci, J. Whitelaw, *Engineering Calculational Methods for Turbulent Flows*, Academic Press, New York, 1981.

29. M. J. Lewis, *Sharp Leading Edge Hypersonic Vehicles in the Air and Beyond, Sae Transactions*, 1999, vol. 108, No. 1, pp. 841-851

30. D. Thomas, Design and Analysis of UHTC Leading Edge Attachment, NASA CR-2002

31. E. Zoby, Empirical Stagnation Point Heat Transfer Relation in Several Gas Mixture at High Enthalpy Levels, NASA TN D-4799.

32. F.K. Lu and D.E. Marren, Principles of Hypersonic Test Facility Development, Advanced Hypersonic Test Facilities, edited by F.K. Lu and D.E. Marren, AIAA, 2002, Vol.198, pp. 17-27.

33. D.M. Smith, E.J. Felderman, F.L. Shope, and J.A. Balboni, Arc-Heated Facilities, Advanced Hypersonic Test Facilities, edited by F.K. Lu and D.E. Marren, AIAA, 2002, Vol.198, pp. 279-314.

34. A. Gulhan and B. Esser, Arc-Heated Facilities as a Tool to Study Aerothermodynamic Problems of Reenty Vehicles, Advanced Hypersonic Test Facilities, edited by F.K. Lu and D.E. Marren, AIAA, 2002, Vol.198, pp. 375-403.

35. G. Russo, F. DeFilippis, S. Borrelli, M. Marini, and S. Caristia, The SCIROCCO 70-MW Plasma Wind Tunnel: A New Hypersonic Capability, Advanced Hypersonic Test Facilities, edited by F.K. Lu and D.E. Marren, AIAA, 2002, Vol.198, pp. 315-351.

36. R. Savino, D. Paterna, "Blunted cone-flare in hypersonic flow", Computers & Fluids, Vol. 34, 2005, pp 859-875.

37. R.C. Millikan and D.R. White, "Systematics of Vibrational Relaxation", The Journal of Chemical Physics, Vol. 39, No. 12, 1963, pp. 3209-3213.

38. J.O. Hirscfelder, C.F. Curtiss and R.B. Bird, "Molecular Theory of Gases and Liquids", Wiley, New York, 1954, pp 75-106.

39. P.L. Roe, "Characteristic Based Schemes for the Euler Equations", Annual Review of Fluid Mechanics, Vol.18, 1986, pp 337-365.

40. L.Walpot, H. Ottens: "FESART/EXPERT Aerodynamic and Aerothermodynamic analysis of the REV and KHEOPS configuration", ESA ESTEC Technical Report TOS-MPA/2718/LW, 16th September 2002.

41. M.E. Tauber: ”A review of High-Speed Convective, Heat Transfer Computation Methods”,NASA Technical Paper 2914, 1989.

42. Internal report: UHTC plasma torch test.

43. Rasky D.J., Advanced Ceramic Matrix Composites for TPS, Current Technology for Thermal Protection System, NASA Conference Publication CP-3157, 1992.

44. Capitelli M., Colonna G., Gorse C., D’Angola A., “Transport Properties of High Temperature Air in Local Thermodynamic Equilibrium”, The European Physical Journal, D11 279-289 (2000).

45. George C., Candler G., Pfender E., “An Implicit Algorithm to Simulate Reaction Chemistry in a Plasma”, J. Phys. D: Appl. Phys. 31 (1998) 2269-2280.

46. Park C., “Nonequilibrium Hypersonic Aerothermodynamics”, John Wiley & Sons, 1990.

47. Sakai T., Sawada K., “Calculation of Nonequilibrium Radiation from a Blunt-Body Shock Layer”, Journal of Thermophysics and Heat Transfer, Vol. 15, No 1, pp 99-105, January-March 2001.

48. D.C. Wilcox, Turbulence Modeling for CFD, DCW Industries, Inc., La Canada, California, 1998.

49. J.C. Greaves and J.W. Linnett. “Recombination of Atoms at Surfaces. Part 5. Oxigen Atoms at Oxide Surfaces”. Trans. Faraday Soc., 1959, 55, 1346.

50. P.G. Dickens and M. B. Sutcliffe. “Recombination of Oxigen Atoms on Oxide Surfaces. Part 1. Activation Energies of Recombination”. Trans. Faraday Soc., 1964, 60, 1272.

51. G. A. Melin and R.J.Madix. “Energy Accomodation During Oxygen Atom REcombination on Metal Surfaces”. Trans. Faraday Soc., 1971, 67,198.

52. B. Halpern and D.E.Rossner. “Chemical Energy Accomodation at Catalyst Surfaces”. Trans. Faraday Soc., 1977, 73, 1883.

53. R.B. Pope. “Stagnation-Point Convective Heat Transfer in Frozen Boundary Layers”. AIAA Journal, Vol. 6, No. 4, April 1968.

54. A.F. Kolesnikov, I.S. Pershin, S.A. Vasil’evskii and M. I. Yakuskin.”Study of Quartz Surface Catalicity in Dissociated Carbon Dioxide Subsonic Flows”. Journal of Spacecraft and Rockets, Vol. 37, No. 5, September-October 2000.

55. U.S. Standard Atmosphere, 1976, U.S. Government Printing Office, Washington, D.C., 1976.

56. David A. Stewart, Surface Catalysis and Characterization of Propose Candidate TPS for Access-to-Space Vehicles, NASA TM-112206, July 1997.

57. Angelo Bongiorno, Clemens J. Först, Rajiv K. Kalia, Ju Li, Jochen Marschall, Aiichiro Nakano, Mark M. Opeka, Inna G.Talmy, Priya Vashishta, and Sidney Yip, *A Perspective on Modeling Materials in Extreme Environments: Oxidation of Ultrahigh-Temperature Ceramics*, MRS BULLETIN, VOLUME 31, MAY 2006.

58. Jochen Marschall, Adam Chamberlain, Daniel Crunkleton and Bridget Rogers, *Catalytic Atom Recombination on ZrB2/SiC and HfB2/SiC Ultrahigh-Temperature Ceramic Composites*, Journal of Spacecraft and Rockets Vol. 41, No. 4, July-August 2004.

59. L. Scatteia, G. Cosentino, S. Cantoni, M. Balat-Pichelin, E. Beche, J.L. Sans, *An Investigation upon the Catalytic and Radiative Behaviours of ZB_2-SiC Ultra High Temperature Ceramic Composites,* Proceedings 5th European Workshop on Thermal Protection Systems and Hot Structures Noordwijk, The Netherlands, 17 - 19 May 2006 (ESA SP-631, August 2006).

60. Bellosi, F. Monteverde, *Ultra High Temperature Ceramics: Microstructure Control and Properties Improvement related to Material Design and Processing Procedures*, CNR-ISTEC, Institute of Science and Technology for Ceramics, Via Granarolo 64, 48018 Faenza, Italy.

61. Marschall J., Chamberlain A., Crunkleton D., Rogers B., *Catalytic Atom Recombination on ZrB_2/SiC and HfB_2/SiC Ultra-High Temperature Ceramic Composites*, Journal of Spacecrafts and Rocket, Vol.41, No. 4, 2004, pp. 576-581.

62. L. Scatteia, R. Borrelli, G. Cosentino, F. De Filippis, G. Marino, *Advanced ceramic materials for sharp hot structures*, Proceedings of AIAA 13th International Space Planes and Hypersonics Systems and Technologies Conference, CIRA, Capua, ITALY, 16-20 may 2005.

63. Balat-Pichelin M., Badie J.M., Berjoan R., Boubert P., *Recombination Coefficient of Atomic Oxygen on Ceramic Materials Under Earth Re-Entry Conditions by Optical Emission Spectroscopy*, Chemical Physics, Vol. 291, No. 2, 2003, pp. 181-194.

64. Balat M. J. H., Czerniak M., Badie J. M., *Ceramic Catalysis Evaluation at High Temperature Using Thermal and Chemical Approaches*, Journal of Spacecrafts and Rockets, Vol.36, No. 2, 1999, pp. 273-279.

List of Figures

List of Tables